Abstract

Title of Dissertation	Microwave Surface Impedance Investigation of the Superconducting Proximity Effect in Superconductor/Normal-Metal Bilayer Structures

Michael S. Pambianchi, Doctor of Philosophy, 1995

Dissertation Directed by	Professor Steven M. Anlage
	Department of Physics

This thesis seeks to develop a clearer understanding of the microwave-frequency electrodynamics of thin normal metal films which are superconducting by virtue of intimate contact with a superconducting film. It is found in superconductor/normal-metal (S/N) bilayer thin films of Nb/Cu and Nb/Al that the effective penetration depth and the surface resistance decrease precipitously as the temperature is lowered toward zero, unlike the exponentially slow variation of these quantities with temperature in a bare superconducting film. This behavior is associated with the temperature dependence of the characteristic penetration length scale of the superconducting order parameter in the normal metal film, which diverges as $T \to 0$. However, theory predicts that the normal metal films under study in this thesis, having thicknesses in the range 100 - 800Å, are much thinner than this decay length and hence should not show strong temperature dependence as this length scale diverges. We conclude that this theory is not adequate for describing the spatial dependence of the induced order parameter very near the S/N interface, and develop an improved model of the electrodynamics of proximity-coupled systems with very thin normal metal layers which reproduces the observed data. We demonstrate that a much shorter effective decay length for the order parameter in the

normal layer can correctly describe the extent of proximity coupling in these structures.

The advantages of the parallel-plate resonator technique in exploring these effects are presented. The distinctive ability of the technique to simultaneously gather data on the properties of the induced superconducting condensate (penetration depth data) and the properties of the spectrum of excitations above it (surface resistance data) in the proximity-coupled normal metal set the technique apart from previous methods, and allow it to study the very thin normal metal layers on which data are presented here. In addition to the much shorter effective decay length, we give strong evidence for the existence of case II coherence effects between excitations in the normal metal, indicating that the induced superconducting state exhibits the same quasiparticle correlations as a true superconducting state.

MICROWAVE SURFACE IMPEDANCE INVESTIGATION OF

THE SUPERCONDUCTING PROXIMITY EFFECT IN

SUPERCONDUCTOR/NORMAL-METAL

BILAYER STRUCTURES

by

Michael Scott Pambianchi

Dissertation submitted to the Faculty of the Graduate School
of The University of Maryland in partial fulfillment
of the requirements for the degree of
Doctor of Philosophy
1995

Advisory Committee:

Assistant Professor Steven Anlage, Chairman/Advisor
Professor Richard L. Greene
Professor Jeffrey Lynn
Professor Christopher Davis
Dr. Stuart Wolf, Naval Research Laboratory

Dedication

To my father

and

to my wife

Acknowledgments

Acknowledging those who have aided and supported me through my graduate school years is a pleasure. I've received help from professors, postdocs, fellow grad students and family members, not to mention the folks who prepare tea in the Physics lobby every day at 3:30. Getting a Ph.D. is full of perplexing problems, unresolved contradictions, long hours, and computer malfunctions; the unflagging support from the people mentioned below enabled me to get through to the good stuff.

I want to thank my advisor Steven Anlage for his immense contribution to my graduate education and his extremely robust, exuberant attitude toward scientific research. He's the one who has instilled in me the level of confidence and the drive needed to perform good work, take the best data possible, put the results into an exciting context, and communicate it effectively. His frequent presence in the lab and desire to work alongside us there whenever possible always gave me the feeling of being part of a team.

My fellow Microwave Group members, Jim Booth, Jian Mao, and Dong Ho Wu, provided great support, both technically and nontechnically. Together, we grappled with issues from microwave connectors and GPIB bus commands to graduation requirements and the search for a job. They were always a pleasure to work with. I'd also like to thank the outstanding undergraduate students who worked in our lab, Tony De Marco, Arijit Das, and Ali Gökirmak, for cheerfully enduring my presence. They're smart guys and will all enjoy great success in their future endeavors.

My fellow grad students Chris Doughty, Santanu Bhattacharya, Alp Findikoglu, Sining Mao, Chuhee Kwon, Ichiro Takeuchi, and Vitaly Talyansky, of the thin film group headed by T. Venkatesan, were also close companions throughout my time at Maryland. Their knowledge of thin films and their willingness to provide test samples was a tremendous resource for me.

I also want to thank the faculty members of the Center for Superconductivity Research, Profs. Rick Greene, Chris Lobb, Venky Venkatesan, Fred Wellstood, and Jeff Lynn, for providing constructive critical remarks on talks I gave at the weekly Center meetings. Their comments contributed greatly to the development of my style when giving presentations and will certainly play a role in my ability to secure job offers. I want to thank Chris Lobb especially for several enlightening discussions we had.

I owe a great deal of my accomplishment to the untiring support of my father, Wayne Pambianchi, who convinced me six years ago that getting a Ph.D. was a good idea and who provided immeasurable support during the past six years, both materially and ideologically, to help me complete the degree. He was the one who made sure I always realized the value such an accomplishment would carry later in life.

Finally, I want to thank my wonderful wife Christy for bearing with me while I completed this important part of my career, and for her willingness to make Maryland fit into her own ambitious career for a few years while I was here. Her unmatched enthusiasm and extremely energetic personality have been by far my greatest source of energy.

Mike Pambianchi
College Park, Maryland
19 July 1995

Table of Contents

List of Tables

List of Figures

x

xi

xiii

Chapter 1
Proximity Effect History and Background

1.0 Introduction

When it was discovered in the early 1930's that a normal metal in contact with a superconductor exhibited some hints of superconducting behavior, all scientists could do was wonder and gather data. No suitable theory of the phenomenon of superconductivity had even been advanced, so the apparent induction of this phenomenon into a nonsuperconducting metal by mere contact was perhaps not very surprising. Yet today, when the Bardeen-Cooper-Schrieffer (BCS) theory [1] of superconductivity and its various refinements have enjoyed marvelous predictive success across a large number of experiments on conventional, low-T_c superconductors, the exact manner in which superconductivity can be induced by a metallic contact into a nonsuperconducting metal still eludes complete theoretical treatment.

Since the early 1930's, many more experiments have been performed on superconducting and normal metal wires and layered superconductor/normal-metal thin film heterostructures. A few key traits of proximity-superconducting systems have emerged:

(a) Current can flow through a normal metal without resistance if the normal metal is in contact with a superconducting metal.

(b) Contact with a normal metal affects the transition temperature of a superconductor; the transition temperature decreases with increasing normal metal thickness, down to a constant value which in turn depends only on the thickness of the superconducting metal. The transition temperature goes to zero as the superconducting metal thickness goes to zero.

(c) Magnetic flux is excluded, at least partially, from the interior of a normal metal

1

in proximity contact with a superconductor.

(d) Tunneling spectra of some proximity-coupled normal metals indicate a gap in the density of states, suggesting that a true superconducting state exists in an otherwise normal metal.

These observations point to an effect rich in underlying physics, and represent what is still an incompletely solved many-body quantum-mechanical problem. One can, however, hope to understand the behavior of proximity systems from an experimentalist's point of view, which can then assist in the formulation of a microscopic theory. The spatially nonuniform superconducting properties of these systems can lead to behavior unlike that of homogeneous superconductors, and may even find practical application in real devices some day. This thesis offers a new body of valuable experimental evidence advancing the understanding of the superconducting proximity effect.

1.1 Experimental History

It is important to place the work of this thesis, which addresses properties of very thin proximity-superconducting normal metal layers, in proper context. To this end, a rather complete overview of experiments on superconducting proximity-effect systems, most of which were conducted after 1960, follows.

1.1.1 Transport Properties and Suppression of T_c

The first proximity-effect experiments sought to explore and understand the suppression of the transition temperature T_c which occurred in superconductors in contact with nonsuperconducting metals; the earliest such experiments were performed in the early 1930's. The first report [2], in which interface resistances between metals was examined, demonstrated that Pb-Pb, Sn-Sn, and Pb-Sn contact regions behaved

essentially like superconducting regions, with no resistance developing across a contact in the superconducting state. The first quantitative study of true superconductor/normal-metal (S/N) layered structures was soon performed at the University of Toronto in 1934 [3], where tin was deposited onto Cu and constantan wires. A monotonic decrease in the transition temperature T_c of tin was noted with decreasing tin thickness, until T_c was suppressed below 1.9K (the lower limit of the apparatus) at tin thickness ~ 2000Å. Decreased critical current density was also reported. Similar experiments on S/N alloys (not layered structures) had also indicated these behaviors [4] upon examining the resistive transition. It was not until 1958, however, that true interest in the proximity effect appeared in the literature. This was probably related to the recent success of the Bardeen-Cooper-Schrieffer (BCS) microscopic theory of superconductivity [1] and the subsequent work of Gor'kov [5] relating it to the Ginzburg-Landau phenomenological theory.

In 1958, Hans Meissner [6] showed that a thin layer of normal metal between two superconducting metals does not necessarily prevent supercurrent from flowing through the contact, as demonstrated with crossed wires of Sn, Cu-plated Sn, and Sn/In. Later, he showed that superconductivity in the normal metal contact disappears beyond a certain normal metal thickness [7], giving some notion of the "range of order" of the superconducting electrons in the normal metal barrier. It was found, in particular, that clean noble metals (Au, Ag, Cu) had critical barrier thicknesses of 3000 - 4000Å when sandwiched between Sn electrodes, while for ferromagnetic materials (Cr, Fe, Co, Ni) this length was more like 100 - 400Å. In 1960, Meissner extended this work [8] to explore the dependence of T_c on the thickness of the superconducting metal, and found for fixed normal metal thickness that there was a critical Sn thickness below which superconductivity did not occur. These more detailed, quantitative results firmly established the fact that the normal metal really becomes superconducting in such systems, rather than just an improved normal conductor.

3

Further work by Smith *et al.* in 1961[9] included measurements of the critical current J_c and critical field H_c on Pb-Ag bilayer films in addition to studies of the resistive transition in zero field. These showed a decrease of J_c with increasing Ag thickness. Later that same year, measurements of diamagnetic screening [10] were performed on the Sn-Au system by a torsion balance technique. The authors recorded a decrease of T_c with decreasing Sn thickness, eventually passing through $T_c = 1.35K$ (their experimental limit) at Sn thickness 5700Å. Similar T_c dependences on both normal metal and superconductor thicknesses were reported for Cu-Pb [11,12], Sn-Ag [13], and Pt-Pb [12]. The latter authors attempted to deduce the BCS interaction potential V of Cu and Pt, both of which were nonsuperconducting in isolation down to millikelvin temperatures, by carefully studying the thickness dependence of T_c in Pb-Cu and Pt-Pb contacts. They obtained $T_c(Cu) \leq .006K$ and $T_c(Pt) \leq .002K$. Finally, resistive transitions on Pb-In [14] also showed a decrease of T_c with increasing In thickness, in accordance with Jacobs' theory [15].

1.1.2 Tunneling

Depression of the critical temperature was perhaps the simplest consequence of a normal metal in contact with a superconductor, and was explained by several authors in terms of pair-breaking effects similar to but not exactly the same as those associated with magnetic impurities [16-18]. However, workers soon realized that electron tunneling through an insulating barrier was a better way to probe the electronic properties of superconductor/normal-metal (S/N) proximity systems and obtain detailed information about the degree of long range order developed in the normal side of an S/N junction. Metals which formed an oxide easily (Al, Pb, Sn) were used most often as the superconducting side of the junction. It was shown that in a structure such as S/I/N/S (I is the insulating oxide tunnel barrier), the normalized conductance $(dI/dV)_S/(dI/dV)_N$ yielded a direct measure of the density of excitations in N at the boundary with the

insulator [19]. In particular, a gap in the electronic excitation spectrum of the N metal could be clearly discerned.

Early measurements by Smith *et al.* [9] on the Ag-Pb system found a "gap" of 0.16 meV in the Ag layer of a bilayer sample consisting of 5700Å Ag on 1500Å Pb. Much more detailed work on the Cu-Pb system [20] also observed a large increase in the density of states identifiable as a "gap" in Cu, with the gap decreasing in magnitude as the Cu thickness was increased. They also found a strong localization of states just above the gap energy in Cu, but no evidence of the bound states inside the gap predicted by de Gennes and St. James [21]. McMillan and Rowell [22] and Tomasch [23] did find periodic behavior of d^2V/dI^2 versus voltage in Ag-PbO-Pb and Al-AlO$_x$-In junctions, respectively, with the periodicity depending only on the normal metal thickness. This was interpreted as a set of bound states in N to which entering electrons lost energy.

Then in 1969, Clarke [24] demonstrated in a very careful Pb-Cu SNS tunneling measurement that there was a clear gap in the Cu excitation spectrum, enabling him to estimate $T_c(Cu) \approx 10^{-5}$K. In many ways this experiment brought out the similarities between SIS (Josephson) junctions and SNS junctions (both show interference effects visible as a Fraunhofer pattern in the critical current vs. magnetic field) while clarifying the differences (SNS has linear sections of the Fraunhofer central maximum and a 5000Å normal metal barrier instead of a 20Å-thick insulating barrier). Subsequent work by Greenspoon on Pb-PbO-Cu-Pb junctions [25], Romagnan on Pb-PbO-Sn-Pb and Pb-Sn-Pb junctions [26-27] and Wolf et al. [28] on Nb-Al enabled the phonon structure and the Eliashberg function $\alpha^2 F(\omega)$ to be studied in S/N bilayers. An excellent review of tunneling experiments in S/N bilayers can be found in Wolf's book [29].

1.1.3 Magnetic Screening and Magnetic Breakdown

The ability to screen out an applied DC magnetic field is a key trait of a superconductor, and measurements of the penetration depth λ are often used to

characterize superconducting samples. A normal metal with proximity-induced superconductivity naturally displays flux expulsion also, and this was used to study the spatial dependence of the induced order parameter $\Delta(z)$. In early measurements, such as those performed at Orsay by Burger *et al.* [30], a normal metal layer was deposited on the exterior of a hollow cylinder of superconducting metal and the cylinder was inserted into the inductor coil of a resonant circuit, in the manner of Schawlow and Devlin [31]. The resonant frequency $f(T)$ of the circuit depends sensitively on the flux excluded by the sample, yielding information about magnetic penetration into the bilayer (see Fig. 1.1).

This early work [30] in the mid 1960's was performed on InBi/Zn bilayer samples, with Zn as the normal metal $(T_c(Zn) = 0.9K)$. Both components were in the dirty limit, with thicknesses 1000Å - 5000Å for Zn and 3500Å - 10000Å for InBi. Rapid flux penetration occurred for H > 90 Oe at 2.1K, and this "breakdown field" H_b increased as T decreased. By varying the normal metal thickness d_N the dependence $H_b \sim e^{-Kd_N}$ was ascertained. The length scale K^{-1} was interpreted as the effective penetration distance for superconducting electrons into the normal metal.

A theory for the penetration of flux into a proximity-coupled normal metal layer was quickly developed by P. G. de Gennes and others at Orsay [32] to explain the results of the Schawlow-Devlin experiments. For weak magnetic fields, assuming exponential decay of the order parameter in the normal metal far from the S/N interface, de Gennes arrived at the well-known expression

$$\rho = K^{-1}\left[\ln\left(\frac{K^{-1}}{\lambda(0)}\right) - 0.116\right] \tag{1.1}$$

where ρ is the position in N measured from the S/N interface where the magnetic field gets abruptly screened out, and $\lambda(0)$ is the induced local penetration depth in the normal metal at the interface. A typical screening profile is shown in Fig. 1.1. It was soon verified using the same InBi/Zn bilayers that Zn was indeed capable of screening a magnetic field at temperatures well above $T_{cN} = 0.9$ K, and that relation (1.1) was correct

6

within 20% [33]. In the dirty limit the temperature dependence of K^{-1} was predicted to be $K^{-1} \sim T^{-1/2}$, a simple result emerging from a diffusion process and rooted in Ginzburg-Landau theory, so that according to Eq. (1.1), one should observe $\rho \sim T^{-1/2}$ well above T_{cN}. The first true test of this prediction was done in 1969 by Deutscher *et al.* [34] using the same Schawlow-Devlin technique, on Pb/Cd and Pb/Zn samples with

Normal Metal
$\sim 10 \ \mu$m thick

Superconductor
$\sim 30 \ \mu$m thick

H

N   **S**

ρ

H

Field Penetration Profile

Schawlow-Devlin Coil
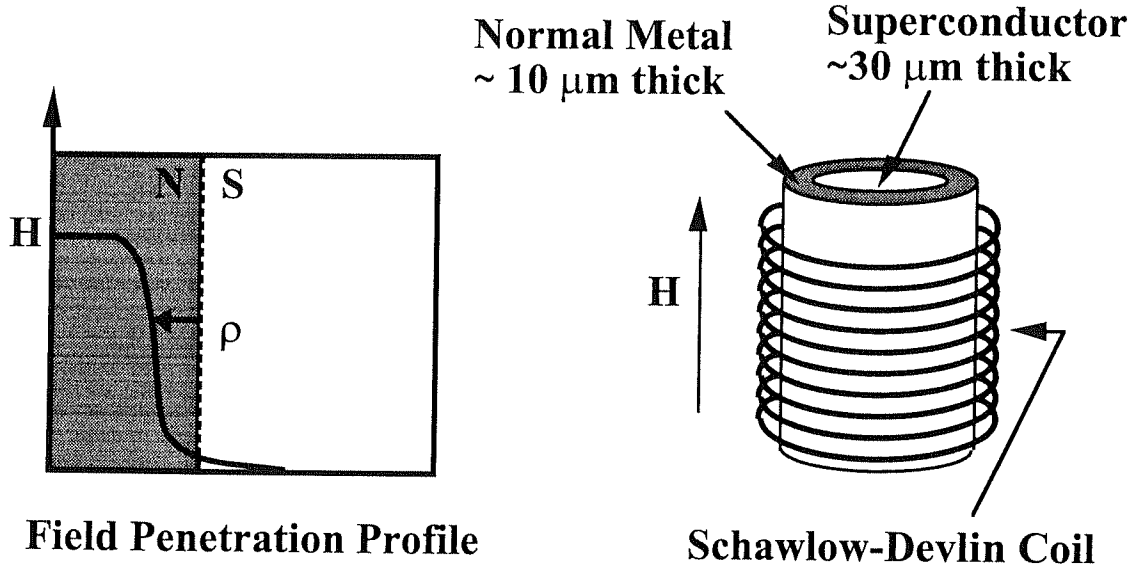
Figure 1.1. The Orsay picture of magnetic field penetration into thick proximity-coupled normal metals, and the Schawlow-Devlin coil technique used to measure the thickness of the Meissner region, ρ, in drawn normal/superconducting wires.

normal layer thicknesses $d_N = 2000\text{\AA}$ to $20000\text{\AA}$. The relation (1.1) was found to be correct in suitably prepared samples for T well above T_{cN}. For these relatively thin N layers, the approximations used in deriving Eq. (1.1) often became invalid as $T \rightarrow T_{cN}$ and data tended to deviate from model predictions, however. Subsequent work on Ag/Pb and Cu/Pb by Vallette [35] using the same technique yielded similar results. They incidentally also led to the conclusion that both Ag and Cu probably had superconducting transition temperatures somewhere below 10^{-4}K.

The group at Orsay effectively dominated the study of magnetic penetration in

proximity-coupled normal metals throughout the 1960's and early 1970's, using superconductors such as Pb and Sn to back normal metals. It was not until 1978 that Oda and Nagano [36] joined this effort, this time in Cu backed by Nb and NbTi. Niobium had of course been a desirable elemental superconductor to use in such experiments all along due to its high transition temperature $(T_c = 9.3K)$, but it was not until commercially available Nb wires had been perfected for use in superconducting magnets (mid 1970's) that it was used to back normal metals in proximity-effect experiments. The samples studied by Oda and Nagano were 250 μm-diameter Nb and 70 μm-diameter NbTi wires, coated with 350 μm and 100 μm Cu, respectively. Their results, obtained using basically the same resonant coil technique, extended down to 25 mK and showed a temperature dependence $\rho \sim 1/(T + T_0)^{-1/2}$, where $T_0 = 73$ mK and 57 mK, and $\rho(25mK) = 12$ μm and 7 μm, for Nb/Cu and NbTi/Cu, respectively. Though ρ showed no sign of saturating as T -> 0, the observed temperature dependence did not agree with the dirty-limit Orsay theory for T < 1.5 K. This was not unexpected, however; studying proximity effects in such thick (10 - 100 μm) normal metal layers only made sense if millikelvin temperatures could be reached, a region of temperature that had not been accessible to the Orsay Group and also was not covered by their theories.

The behavior of Cu in proximity contact with NbTi was subsequently studied by Mota *et al.* [37] using samples very similar to those of Oda and Nagano, and going down to 5 mK. The authors found that ρ saturated at a value equal to the Cu thickness, implying that in thicker Cu layers the diamagnetic properties of the Cu layer would have continued to strengthen further as T -> 0. For T > 200 mK, they observed $\rho \sim T^{-1.4}$, interpreted by them as consistent with their assessment that their samples were in the clean limit. Mota *et al.* also made extensive studies of the breakdown field H_b in Cu, the value of the magnetic field where sudden penetration of field occurred. They found the relation $H_b \sim \exp(-\alpha T d_N)$, indicating that the Orsay result $H_b \sim \exp(-K d_N)$ would hold if $K \sim T$. This implied clearly that a clean limit expression $K^{-1} \sim 1/T$ was applicable to their

samples. Their measurements of the breakdown field were the first to be performed on a metal with essentially zero transition temperature, and the values of $H_b \approx 1$ Oe in Cu were found to be much smaller than those of Zn ($H_b \approx 100$ Oe).

Further work by Oda *et al.* [38] on similar Cu-coated Nb wires exhibited $\rho \sim T^{-1/2}$ nearly perfectly down to 4.5 mK, utterly defying the restriction that the Ginzburg-Landau theory should apply only near T_c, with ρ becoming comparable to the Cu thickness below 20 mK as in the work of Mota *et al.* [37] The dependence of ρ on magnetic field was studied in great detail and the authors showed that when $\rho < d_N$, the relation $\rho \sim \ln H$ held at fields in the range $H = 0.01 - 1.0$ Oe, whereas when $\rho \sim d_N$ (the case below 20 mK) ρ was independent of H up to a breakdown field H_b, after which a rapid decrease of ρ occurred. H_b increased with decreasing temperature as well, and the rapid shrinking of the Meissner region was observed to be fully reversible upon removal of the field, which had not been the case for InBi/Zn. Similar to Cu, these breakdown fields in Ag were of the order of $0.1 - 1$ Oe. It was concluded that these results were all in accordance with Orsay theories of magnetic breakdown in S/N bilayers, with little exception. Similar experiments on Au-coated Nb were later reported [39], with $\rho \sim T^{-1/2}$ as before, but the results were generally weaker than with Cu, and were attributed to poorer S/N interface quality. Later, Mota *et al.* [40] showed that both clean and dirty limit samples, characterized independently, showed the correct corresponding temperature dependences $K^{-1} \sim T^{-1}$ and $K^{-1} \sim T^{-1/2}$ down to very low T, further verifying the Orsay picture despite the fact that the theories of the Orsay Group were developed in the Ginzburg-Landau framework with a small induced order parameter ($T \sim T_c$) in mind.

The most recent DC magnetization work using the inductance coil technique to detect flux exclusion in thick proximity-coupled samples has come from Mota's group in Switzerland [41-42]. They report on Nb/Cu and Nb/Ag drawn wires, as well as providing an excellent summary of screening experiments in proximity samples to date. The Nb/Ag samples were drawn in a similar fashion to the previously studied Nb/Cu

samples, but the Ag was extremely clean (ℓ_{Ag} = 20 μm). They observed an even stronger temperature dependence $\rho \sim T^{-2}$, saturating at $\rho = d_N$ = 5.3 μm for T < 1K. From studies of the breakdown field in Nb/Ag (again on the order of 1 - 10 Oe) they show $K_{Ag}^{-1} \sim 1/T$ as expected for such a clean normal metal. In this work, perhaps the most important conclusion drawn regards the spatial dependence of the superconducting order parameter $\Delta_N(x)$. Far from the interface in the dirty limit at high temperatures, the Orsay result [43] was essentially $\Delta_N(x) = \Delta_N(0) \, e^{-K|x|}$. On the other hand, Falk [44] showed early on that at low temperatures this dependence should become $\Delta_N(x) \sim 1/|x|$, not exponential, far from the interface. Mota *et al.* [41] have deduced, by studying the behavior of local critical fields $H_c(x)$ in the normal layer, the spatial dependence of $\Delta_N(x)$ *near* the interface, i.e. $|x| \ll K^{-1}$. This region is not often treated theoretically, though it is frequently encountered in experiment. Their results show that in that region a more appropriate form of the order parameter is $\Delta_N(x) = \Delta_0 \, x_0/(|x|+x_0) \, e^{-K|x|}$, with $x_0 \ll d_N$. They quote for example x_0 = 0.7 μm in Ag at 7 mK in a sample with d_N = 14.5 μm. This has the profound implication that Δ_N is never constant across a thin N layer at any temperature, in agreement with many thin film experiments including those presented in this thesis.

More recently, Claassen *et al.* [45] have used the low frequency mutual inductance technique of Hebard and Fiory [46] to examine the screening of applied magnetic field in NbN/Al and Nb/Cu bilayer films. Their geometry is shown in Fig. 1.2. In contrast to previous proximity effect work where the superconducting layer was relatively thick, this technique works best when the S layer is thinner than its own penetration depth. Hence samples consisting of 550Å Nb/12000Å Cu an 500Å NbN/1100Å Al were studied. The results on both samples showed that the effective penetration depth of the whole bilayer continued to decrease as T decreased, and that the rate of decrease even became more rapid as T -> 2K in the Nb/Cu sample. When a NbN/Al sample with an AlO$_x$ layer at the S/N interface was measured, it exhibited the

same behavior as bare Nb. The authors concluded that they had measured considerable screening of the field in relatively thin normal metal layers, and that their temperature dependence was in agreement with the dirty limit expression $K^{-1} \sim T^{-1/2}$. Very recent results from this group [47] on NbN/Al down to 0.8 K have found a much stronger temperature dependence $K^{-1} \sim T^{-2}$ for $T > T_{c,Al} = 1.14$ K, reminiscent of the work of Mota *et al.* [41] on Nb/Ag.

Drive coil

Pickup coil
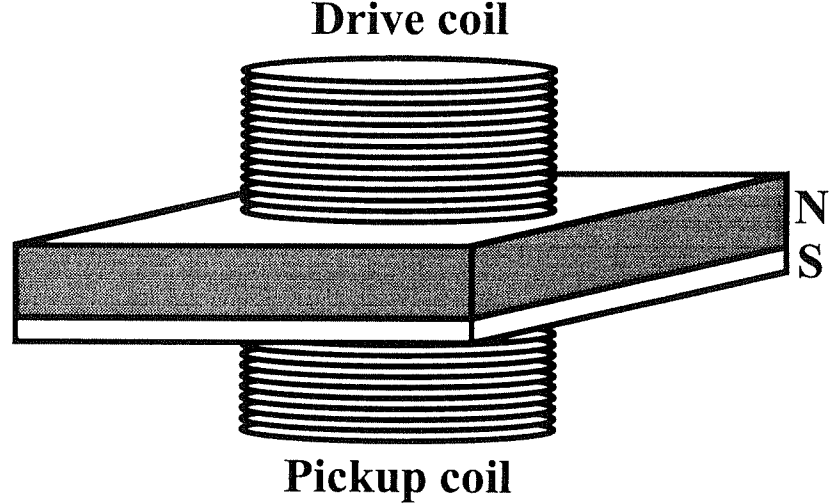
Fig. 1.2. The mutual inductance technique of Hebard and Fiory used by Claassen *et al.* to measure the kinetic inductance of proximity-coupled bilayer films with thick N layers and thin S layers.

1.1.4 Josephson Critical Current Modulation

Perhaps the most elegant experiments on magnetic penetration into proximity-superconducting normal metals were performed by Simon and Chaikin [48]. These experiments were completely separate from the magnetization experiments of the previous section in that they utilized a quantum-mechanical effect with great magnetic field sensitivity, the Josephson effect, to measure the field penetration in a normal metal. The largest drawback of their technique was certainly the difficulty of fabrication of adequate samples in the correct geometry, but the advantage of being sensitive to the

11

absolute value of the flux threading their junction justified painstaking fabrication. Their method also concentrated on the magnetic screening ability of relatively thin (< 1 μm) normal films, so they were working in the near-interface region.

Their experiment is described by Fig. 1.3. A tin electrode of thickness 3000Å was deposited, and its surface allowed to oxidize. Then silver and lead were deposited on top, in an SINS' structure. The oxide layer was very thin, so that a Josephson
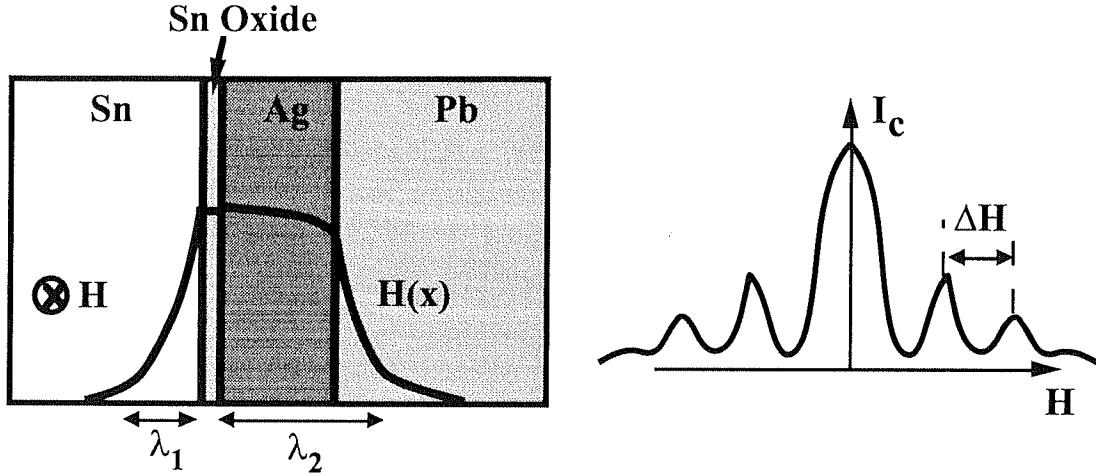
Fig. 1.3. Josephson critical current modulation experiment of Simon and Chaikin.

current developed across it. When a DC magnetic field was applied parallel to the layers, the critical current displayed the well-known Fraunhofer diffraction pattern $I_{max} = I_0$ $\sin(\pi\Phi/\Phi_0)/(\pi\Phi/\Phi_0)$ as a function of field. The diffraction peaks were spaced by the interval $\Delta H = \Phi_0/[W(\lambda_1 + \lambda_2 + d)]$, where W is the width of the junction, λ_1 and λ_2 are the effective penetration depths of the tin and silver/lead electrodes, d is the oxide barrier thickness, and Φ_0 is the flux quantum. Because λ_2 contains the screening effects of both the proximity-coupled silver layer and the Pb layer behind it, this spacing ΔH could be used to study the proximity effect in silver, particularly its temperature dependence. Simon and Chaikin used 4000Å Pb to back their silver layers, which had thicknesses in

12

the range 400Å - 10000Å. They found at low temperatures that the effective penetration depth in the Ag/Pb electrode increased linearly with silver thickness up to $d_N = 2000$Å, remained relatively constant up to $d_N = 4000$Å, and then increased again. This plateau region at 2000Å $\leq d_N \leq 4000$Å showed an effective penetration depth of ~ 1500Å, suggesting that this may have been the characteristic penetration depth of their silver film. For several Ag thicknesses from 2500Å to 10000Å, the zero-temperature extrapolated penetration depth also was found to be in the range 1200Å - 1600Å. The dependence of λ_{eff} was noticeably linear in T below 3K.

These authors were the first to explicitly calculate magnetic field profiles in S/N bilayers using the concept of a spatially varying penetration depth $\lambda_N(z)$ in the normal metal. They used the form

$$\lambda_N(z) = \lambda_0 \frac{\cosh Kd_N}{\cosh K(d_N - z)} \qquad (1.2)$$

which is the approximate dependence developed by the Orsay group with boundary condition $d\Delta/dz = 0$ at the free surface. This dependence, along with a generalized version of the second London equation, led to the differential equation describing the magnetic field in the normal layer:

$$\frac{d^2H}{dz^2} + 2K \tanh[K(d_N - z)] \frac{dH}{dz} - \frac{1}{\lambda_0} \frac{\cosh^2[K(d_N - z)]}{\cosh^2 Kd_N} H = 0 \qquad (1.3)$$

This equation could not be solved analytically, so numerical methods were used to calculate field profiles in the S/N electrode for comparison with experiment. Simon and Chaikin were thus able, using the dirty limit temperature dependence of $K^{-1}(T)$, to deduce the size of the order parameter decay length induced into the silver layer, which

13

they found to be 6150Å at 1.2 K. They emphasized also that this temperature dependence could always be expected to become valid as T -> 0 since at some point the diverging decay length would always exceed the mean free path (dirty limit), but that at higher temperature the samples might act cleaner. Their work in general was the first to attempt to improve the understanding of magnetic screening beyond that of the simple Orsay expression (1.1).

In a subsequent publication [49] Simon and Chaikin extended their work to other bilayer systems, using Al/Pb, Ag/Sn, Sn/Pb and trilayer Ag/Sn/Pb for the second electrode of the Josephson junction, and going down to 0.1 K. This work attempted to establish whether screening properties in proximity-superconducting normal metals depended more on properties of the normal metal (comparing Ag/Pb, Al, Pb and Sn/Pb) or more on characteristics of the backing superconductor (comparing Ag/Pb, Ag/Sn, and Ag/Sn/Pb). They also investigated the effect of normal metal thickness on the induced penetration depth in the normal metal.

With data going down to 0.1 K, they firmly established that the penetration depth in silver backed by Pb goes to 1500Å at very low temperature, independent of silver thickness. This is considerably larger than the London value 250Å for silver. Their silver films were found to have long mean free paths, ruling out the possibility of the dirty limit. Similarly, Al on Pb was found to have a thickness-independent proximity-induced penetration depth of 900Å, larger than the bulk value of 500Å for Al, though the gap induced in Al by proximity to Pb (0.23 meV) was found to be larger than that of bulk Al (0.17 meV).

Upon switching the backing superconductor from Pb to Sn, the penetration depth of Ag was observed to increase to ~3500Å. When Ag was backed by Sn/Pb, this value was 2000Å. In the latter case, the Pb induces a gap in Sn which then dictates the screening ability of Ag. Since the gap in Sn/Pb is between that of Sn and Pb alone, this tested the dependence of λ_{Ag} on the size of the gap in the backing superconductor. λ_{Ag}

14

was found to scale inversely with the magnitude of the gap in S. In all cases, however, neither the dirty nor the clean limit expressions really matched the observed temperature dependences. Another interesting result of their work was the discovery that in metals which have a superconducting transition at lower temperatures (Al, Sn), the induced penetration depth was much larger than the bulk value for these materials below their critical temperatures, despite having larger induced gaps from proximity to Pb. Overall, Simon and Chaikin's work revealed several dependences and behaviors not reported in any other work, making their contribution to the field singularly useful.

1.1.5 High Frequency Measurements

Only a few groups have probed the electromagnetic response of a proximity-coupled normal metal at microwave frequencies, perhaps because coherent microwave sources were not commonplace in the early 1960's when much of the early resistivity and tunneling work was done. Still, microwave measurements performed in the 1960's and '70's did show screening behavior similar to that found at DC in magnetic screening experiments. Additional information pertaining to excitations above the condensate leading to RF losses was also analyzed, but RF measurements have not achieved their full potential in studying proximity systems. One purpose of this thesis is to expand the work at high frequency on S/N structures and give further attention to the benefits of microwave experiments in investigating these structures.

The first early measurement [50] was performed in a cavity at 9 GHz using an endwall replacement technique. The endwall was tin plated with varying thicknesses of gold. The authors measured the power absorbed by a calorimetric technique, so they did not obtain penetration depth data, which is related to shifts in the resonant frequency of the cavity. They simply found that for Au thicker than 500Å, the RF loss did not extrapolate to zero as T -> 0 as they did for pure Sn. Penetration depth measurements were also reported in this work using the Schawlow-Devlin technique and were more

informative, though at low frequency.

A much better early microwave result was obtained by Fischer and Klein [51] on Cu/Pb using the same type of cavity endwall replacement at 9.5 GHz. The authors found that the surface resistance started to decrease rapidly as T -> 0, and that this dependence on temperature was more pronounced in thicker films (~ 5000Å) of Cu than in thinner ones (~ 500Å). The authors relied on reflected microwave power only; they did not provide penetration depth data. They also recorded an initial decrease in the surface resistance upon application of a parallel magnetic field, followed by an increase at higher fields. The minimum in R_s occurred at fields of 20 - 200 Oe at 1.5 K, increasing with decreasing Cu thickness. They developed a semi-quantitative explanation for both the rapid drop with temperature and with field, based on simplified versions of the Orsay theory and the work of Garfunkel [52]. Their results are quite revealing, though the actual purpose of their work, that of estimating the transition temperature of Cu, was not achieved with much precision.

Work on Sn-In alloys using endwall replacement was reported by S. C. Harris [53] at 3 GHz. In samples where phase segregation occurred, proximity effects in the locally normal regions produced rounding of features in the temperature dependence of the surface resistance. Quantitative conclusions were not drawn, though the work did indicate that proximity coupling could substantially affect the behavior of normal/superconducting alloys.

The most recent and most sophisticated effort to study proximity systems at microwave frequency was that of Hook [54]. An early form of the parallel-plate resonator technique used in this thesis [55] was employed to measure the complex surface impedance of Pb/Sn bilayer films over the temperature range 2 - 7 K. The samples consisted of Pb plates (1 mm thick) plated with tin of thickness 6000Å. The tin could be made dirty or clean by adding small concentrations of indium.

The authors found that both the effective penetration depth and the surface

16

resistance dropped rapidly below the T_c of Pb, entered a plateau region over the range 4 - 6 K, then rapidly dropped again while still above the transition temperature of tin (3.72 K). The temperature at which the decrease occurred became higher as the tin thickness was decreased, and eventually the plateau region disappeared altogether for a thin enough tin layer. The authors explained their data using the theory of Hook and Waldram [56], from which they extracted the value of the energy gap Δ_N in the tin at the free surface, on which the surface resistance only depends according to their model. They reported a dependence on normal metal thickness d_N of this free surface gap given by $\Delta_N \sim (d_0 + d_N)^{-1}$.

They also deduced, by fitting their data to their model, that the gap induced in tin is between that of Pb and that of tin in isolation well below T_{cN}. The fitting procedure is described separately [57]. Essentially, Hook assumed that there is a spatially dependent gap over which local quasiparticles are thermally excited. The fitting procedure then calculated the losses numerically using the Hook and Waldram theory for $\Delta_N(z)$ and the boundary conditions of Zaitsev [58], and assumes Mattis-Bardeen theory [59] to calculate the local value of the real part of the conductivity, σ_1. Hook and Battilana were able to fit most of their data well this way, but they conclude that their results do not rule out the Ginzburg-Landau-based theories of the Orsay group and Werthamer either.

While the raw resonator data of Hook on Sn/Pb is compelling, their experiment was not as precise as it needed to be in order to make quantitative statements about the size of the order parameter decay length K^{-1} or the induced normal metal penetration depth λ_N. In addition, they quote surface resistances in excess of 5 mΩ at 2K for Sn/Pb at 9 GHz, which is very high. The spacing between the resonator plates in their experiment is estimated to have been on the order of 2 mm, and in all likelihood Hook and Battilana had some difficulty in determining the extent to which extrinsic losses due to coupling from fringing fields affected the quality factor of their resonator. Presumably such extrinsic losses were very large with such a thick dielectric spacer between the

17

plates. Indeed, they plot data into the normal state of Pb, which is only possible with very wide spacing between two superconducting plates Therefore, it is entirely possible that quantitative treatment of their microwave loss data yielded imprecise results. However, their experiment does represent the only work done previously that was really similar to the goals of this thesis.

1.1.6 Other Experiments: Ultrasound, NMR, Thermal Conductivity

A few other types of experiments have been performed on proximity systems as well, though fewer in number. Nevertheless, these were very careful, high-quality experiments and each contributed uniquely to the overall understanding of the proximity effect.

The proximity effect in Pb-backed silver was investigated in 1973 by Deutscher *et al* [60] using measurements of the thermal conductivity down to 0.5 K. The goal, following interest by Clarke [24] and others, was to measure the electron-electron interaction parameter NV and estimate the superconducting transition temperature, if any, of silver. The ratio of thermal conductivities in the superconducting and normal states, $(K_S/K_N)^{Ag}$, yielded information about the size of the induced gap in the excitation spectrum of Pb-backed silver, since the thermal conductivity is much smaller when there is a gap in the density of electron states than when there are electron states available at energies arbitrarily close to E_F. The normal state data in Ag was achieved in their work by driving the Ag normal with an applied magnetic field of the order of 300 Oe. In this way, they deduced that there is in fact a gap in the density of states of proximity-coupled silver, and that the interaction constant NV is positive and very small (NV ~ 0.05), so that T_c (Ag) $< 10^{-5}$ K. They also point out that tunneling measurements are sensitive mainly to excitations moving in a direction perpendicular to the junction interface and thus are strongly thickness dependent and not always sensitive to the value of Δ_N. Thermal conductivity measurements do not have this limitation.

18

In the same year, Krätzig and Schreiber [61] investigated proximity effects in Al/Pb, Cu/Pb and Ag/Pb bilayers. They also aimed to estimate the electron-electron interaction in normal metals, again by means of measurements of the normal metal penetration depth λ_N and order parameter decay length K^{-1}. Their method involved measuring the ultrasonic attenuation of surface acoustic waves propagated through a thin proximity-coupled bilayer film as a function of magnetic field, the only such experiment on S/N bilayers ever published. In all cases the Pb films were 2500Å thick, and the normal metal thicknesses fell in the range 1000 - 5000Å. As they varied the parallel magnetic field they recorded changes in the ultrasonic attenuation coefficient. At the breakdown field H_b, there was a drastic jump in attenuation. The thickness dependence of this breakdown field, and the temperature at which this transition switched from first to second order were used to determine the normal metal penetration depth λ_N and the order parameter decay length K^{-1}. In contrast to many early proximity effect papers, Krätzig and Schreiber characterized their samples extensively. They found the following quantities in the three normal metals they characterized: K^{-1}_{Al} (1.9K) = 3400 Å, $\lambda_{Al}(0)$ = 460 $T^{1/2}$ ($K^{1/2}$ Å); K^{-1}_{Cu} (1K) = 2020 Å, $\lambda_{Cu}(0)$ = 1040 $T^{1/2}$($K^{1/2}$ Å); K^{-1}_{Ag} (1K) = 3810 Å, $\lambda_{Ag}(0)$ = 1120 $T^{1/2}$($K^{1/2}$ Å). Their results completely support the Orsay picture, though they acknowledge that $\lambda_N(T) \sim T^{1/2}$ must eventually break down at lower temperatures. Most notable are again the large values of λ_N for Cu and Ag, over three times larger than the London values for these metals.

Finally, proximity effects in normal metals can also be studied by nuclear magnetic resonance (NMR). The rate of nuclear relaxation is determined by the density of, and correlations between, thermally excited quasiparticles. The presence of an energy gap is readily detectable as are quasiparticle correlations near T_c (Hebel-Slichter peak). Zheng et al. [62] have published data on the nuclear spin-lattice relaxation rate $1/T_1$ for ^{63}Cu nuclei in Nb/Cu multilayers, in which a small peak in $1/T_1$ was observed just below T_c. At low temperatures, where exponential decrease with T is expected, they found

$1/T_1 \sim T$. They attributed this to a distribution of gaps for different **k**-vectors in the proximity-coupled Cu, with electrons propagated perpendicular to the interface having a gapped spectrum and electrons parallel to the interface behaving gaplessly. The observation of a peak in $1/T_1$ below T_c for ^{63}Cu nuclei does, however, indicate that nuclear relaxation in the presence of the proximity-induced state in Cu (layer thickness 400Å) exhibits the same quasiparticle correlations appropriate to case II coherence factors as a true superconducting state would.

1.1.7 Importance of the Present Work

The data gathered on proximity samples, mostly since 1960, has still not lead to a comprehensive understanding of the full range of proximity effect behavior. This is partly because of the difficulty of reproducing high quality samples with precisely known characteristics, and partly because of the serious lack of a suitable theoretical treatment of some key aspects of the problem, such as the near-interface region. By far most of the work has concentrated on the simplest approximations, i.e., linearization of the Gor'kov integral equation for small order parameter, the dirty-limit diffusion process, and behavior far from the S/N interface. In experiments designed to test proximity-induced superconducting properties of the normal metal far from the interface, theory has been essentially correct. But the more interesting region near the S/N interface is difficult to study both experimentally and theoretically, since linearization is not possible where large order parameters exist.

The work presented in this thesis addresses this relative lack of experimental data in the region of the normal metal near the S/N interface in proximity effect bilayer samples. In fact, since R F losses are considerable in the microwave range, resonant microwave experiments **require** thin normal layers, which are essentially entirely near-interface.

1.2 Theory

Here some of the theory is introduced which has been constructed to explain the nature of the superconducting state that arises in a normal metal due to contact with a superconductor. It is not the purpose of this thesis to provide a fully satisfactory account of these models, but the main ideas provide a relevant background for the work presented here.

1.2.1 The Bogoliubov - de Gennes Equations

To discuss superconductivity which varies in space, Bogoliubov [63] and later de Gennes [64] decided to try to construct a state of lower free energy in a metal by the method of canonical transformation which was used earlier in the self-consistent field description of the BCS ground state and the excitations above it [65-67]. What they did was to construct creation and annihilation operators for position eigenstates rather than for the Bloch states of a pure metal (eigenstates of momentum) or the eigenstates of a metal with nonmagnetic impurities (which are not eigenstates of momentum or of position). These operators were defined as:

$$\psi_\sigma^\dagger(\mathbf{r}) = \sum_{\mathbf{k}} e^{-i\mathbf{k}\cdot\mathbf{r}} \, c^\dagger_{\mathbf{k}\sigma}$$

$$\psi_\sigma(\mathbf{r}) = \sum_{\mathbf{k}} e^{i\mathbf{k}\cdot\mathbf{r}} \, c_{\mathbf{k}\sigma}$$

(1.4)

where $c^\dagger_{\mathbf{k}\sigma}$ and $c_{\mathbf{k}\sigma}$ are fermion creation and annihilation operators for the eigenstates $w_n(\mathbf{r})$ of the normal metal and the sum runs over all $\mathbf{k}$ in the first Brillouin zone. The $w_n(\mathbf{r})$ satisfy:

$$\xi_n w_n = \left(-\frac{\hbar^2}{2m}\nabla^2 + U_0(\mathbf{r}) - E_F\right) w_n$$

(1.5)

21

They then defined a generalization of the original Bogoliubov transformation [65]:

$$\psi_\uparrow(\mathbf{r}) = \sum_n \left[\gamma_{n\uparrow} u_n(\mathbf{r}) - \gamma^\dagger_{n\downarrow} v_n{}^*(\mathbf{r}) \right] \tag{1.6}$$

$$\psi_\downarrow(\mathbf{r}) = \sum_n \left[\gamma_{n\downarrow} u_n(\mathbf{r}) + \gamma^\dagger_{n\uparrow} v_n{}^*(\mathbf{r}) \right] \tag{1.7}$$

in which $u_n(\mathbf{r})$ and $v_n(\mathbf{r})$ (functions of position) are chosen in such a way as to diagonalize the Hamiltonian with electron-electron interactions included:

$$\mathcal{H}_{eff} = \int d\mathbf{r} \left\{ \sum_\sigma \psi_\sigma{}^\dagger(\mathbf{r}) \, \mathcal{H}_0 \, \psi_\sigma(\mathbf{r}) + \Delta(\mathbf{r}) \psi_\uparrow{}^\dagger(\mathbf{r}) \psi_\downarrow{}^\dagger(\mathbf{r}) + \Delta^*(\mathbf{r}) \psi_\uparrow(\mathbf{r}) \psi_\downarrow(\mathbf{r}) \right\} \tag{1.8}$$

and in which the $\gamma_{n\sigma}$'s are new fermion operators creating and destroying the excitations above the superconducting ground state. These excitations turn out to have a finite projection onto both hole and electron states of the normal metal.

The following quantities have been used in (1.8):

$$\Delta(\mathbf{r}) = V(\mathbf{r}) \langle \psi_\uparrow(\mathbf{r}) \psi_\downarrow(\mathbf{r}) \rangle = V(\mathbf{r}) \sum_n v_n{}^*(\mathbf{r}) \, u_n(\mathbf{r}) \, (1 - 2f_n) \tag{1.9}$$

$$\mathcal{H}_0 = \frac{1}{2m} \left(-i\hbar\nabla^2 - \frac{e\mathbf{A}}{c} \right)^2 + U_0(\mathbf{r}) - E_F \tag{1.10}$$

$U_0(\mathbf{r})$ contains the averaged Coulomb interaction between electrons, potentials due to lattice ions, and any overall electrostatic potential, and $V(\mathbf{r})$ is the electron-electron attractive interaction responsible for superconductivity.

Bogoliubov and de Gennes showed that u and v must therefore satisfy the coupled equations:

22

$$\mathcal{H}_0 u(\mathbf{r}) + \Delta(\mathbf{r})v(\mathbf{r}) = Eu(\mathbf{r})$$

$$\qquad\qquad (1.11)$$

$$-\mathcal{H}_0^\dagger v(\mathbf{r}) + \Delta^*(\mathbf{r})u(\mathbf{r}) = Ev(\mathbf{r})$$

These equations are known as the Bogoliubov - de Gennes equations; the quantity $\Delta(\mathbf{r})$ is called the **pair potential**. We see that if $\Delta = 0$, the equations decouple and $u(\mathbf{r})$ and $v(\mathbf{r})$ are just the normal state electron and hole eigenfunctions with energies $\pm E$ relative to E_F. In general, however, the presence of $\Delta(\mathbf{r})$ causes the mixing of electron and hole amplitudes that leads to the superconducting state.

1.2.2 Andreév Reflection

An important consequence of the Bogoliubov - de Gennes equations is the phenomenon of Andreév reflection, which follows naturally from (1.11) when the interaction potential V is not constant in space. This effect, first described by Andreév in 1963 [68], involves the reflections which occur when electrons in the normal metal side of an S/N interface are incident on the boundary. If the incident electron has energy $E > \Delta_S$, where Δ_S is the energy gap on the superconducting side of the interface, then there are states available for the electron to go to when it crosses the boundary. If $E < \Delta_S$, however, then there exist no propagating states in S for the electron to occupy. Instead, a second electron from the normal metal may participate in a Cooper pair with the first and the two can enter the superconducting condensate on the S side, sending a hole backward from the S/N interface along the time-reversed trajectory of the incident electron to conserve momentum. If this occurs, it results in a current twice as large as if the lone electron were to traverse the interface, creating a drop in apparent resistance of a factor of two. It can be shown [68] that essentially the interference of the reflected hole with the incident electron underlies the mechanism for pairing and the evolution of phase coherence in the normal metal.

23

1.2.3 Induced Order Parameter and the Single Frequency Approximation

An early, preliminary theory of superconductivity in the vicinity of metallic contacts on superconductors was put forth by Cooper [17]. He argued that superconducting correlations could extend deep into a volume where the interaction between electrons was actually zero. In such a system, the electron-electron interaction is a function not only of the momenta and relative coordinate between the electrons, but also of the absolute position. The matrix element $V_{k',k}$ for scattering from a two-electron state k into one labeled by k' can thus still be nonzero, and when it is integrated over all k' and averaged over k in the region of interaction, it yields the parameter $[N(0)V]_{av}$, which determines the transition temperature and the energy gap. This average $[N(0)V]_{av}$ will be smaller if the electron-electron interaction acts over only part of the normalization volume, as is the case near an S/N interface. This essentially is the cause of T_c depression, and also predicts that a thin enough normal metal in contact with a superconducting metal can itself become a superconductor, as had already been observed. The simple result Cooper obtained is $[N(0)V]_{av} = N(0)V_{BCS} \, t_1/(t_1 + t_2)$, where t_1 and t_2 are the superconductor and normal metal thicknesses, respectively, and V_{BCS} is the electron-electron interaction potential of the superconducting metal alone. The transition temperature depends exponentially on this factor, though, so according to Cooper even very thin N layers could cause substantial T_c suppression.

De Gennes and Guyon [69] later cast the problem into the Green's function formalism of Gor'kov [5], using a position-dependent electron-electron interaction and thus a spatially varying pair potential. Following Gor'kov, they wrote down the equation for the pair potential $\Delta(r)$ everywhere in an S/N bilayer:

$$\Delta(r) = \int K(r,r') \, \Delta(r') \, d^3r'$$

(1.12)

24

where the kernel $K(\mathbf{r},\mathbf{r}')$ is given by

$$K(\mathbf{r},\mathbf{r}') = \sum_{n,m} V\, w_n(\mathbf{r})\, w_m(\mathbf{r})\, w_n(\mathbf{r}')\, w_m(\mathbf{r}')\, \frac{1 - f(\xi_n) - f(\xi_m)}{\xi_n + \xi_m} \qquad (1.13)$$

and where, as in Eq. (1.5), $w_n(\mathbf{r})$ are normal state one-electron wavefunctions in the two metals, ξ_n are their energies measured from the Fermi level, and f is the Fermi function. This integral equation (1.12) is correct exactly at the critical temperature of the S/N bilayer. The authors showed that in the limit of very small $\Delta(\mathbf{r})$, only the terms of $K(\mathbf{r},\mathbf{r}')$ linear in Δ need be considered, yielding an exponentially decaying solution to Eq. (1.12) far from the interface in the normal metal and near T_c. This is known as the **single frequency approximation**. The decay length of $\Delta(\mathbf{r})$ in N was proportional to $\ell^{1/2}$, where ℓ is the mean free path. They also showed that as NV -> 0 in the normal metal (T_{cN} -> 0), the decay length K^{-1} is given by the diffusion-limited expression $K^{-1} = (\hbar D/2\pi k_B T)^{1/2}$, where $D = v_F \ell/3$ and v_F is the Fermi velocity in the N metal. Though the authors chose not to address the boundary conditions at the S/N interface, useful conclusions explaining the data of Hilsch [11] were drawn. Their work emphasized that proximity experiments could be used to measure the value of NV for metals which have transition temperatures too low to verify experimentally, and that such a technique might not even be very sensitive to the quality of the S/N interface.

Werthamer [70] carried the work of de Gennes and Guyon further, obtaining a complete solution for $\Delta(\mathbf{r})$ and T_c in an S/N bilayer in the single frequency approximation. He used the simplifying assumption that both metals of the bilayer are exactly the same (same Fermi velocity, density of states at the Fermi level, residual resistivity, Debye temperature) except for the electron-electron interaction parameter V. He then expressed the Gor'kov equation (1.12) as a differential equation identical in form to the Schrödinger equation, from which he could use standard solutions to solve for

25

$\Delta(\mathbf{r})$ and T_c in the bilayer case.

The boundary condition $d\Delta/dz = 0$ at a metal-insulator or metal-vacuum interface was clearly understood as necessary to ensure that the probability current in the z-direction went to zero at the vacuum interface. At the S/N interface, it was noted that Δ is discontinuous there, since it is proportional to $V(\mathbf{r})$, which changes abruptly. On the other hand, $\Delta/V = \langle \psi_\uparrow(\mathbf{r})\psi_\downarrow(\mathbf{r}) \rangle$ should be continuous, since it is interpreted as a wave function of a correlated pair. So the appropriate boundary condition was chosen to be that $(1/\Delta)\, d\Delta/dz$ is continuous at the S/N interface. Werthamer thus arrived at the solution:

$$\Delta(z) \sim \begin{cases} V_S \dfrac{\cos K_S(z-d_S)}{\cos K_S d_S}, & 0 \le z \le d_S \\[2em] V_N \dfrac{\cosh K_N(z+d_N)}{\cosh K_N d_N}, & -d_N \le z \le 0 \end{cases} \tag{1.14}$$

and $K_S \tan(K_S d_S) = K_N \tanh(K_N d_N)$. The latter relation he used to predict T_c of S/N bilayers; it was found to reproduce the data of Hilsch [11] quite well. For calculating the transition temperature this entire method should work very well, although it really applies only near T_{cS}, the transition temperature of the S metal, and thus should not be expected to predict behavior properly at very low temperatures.

The temperature dependence of the decay length $K^{-1}(T)$ in the N layer can be derived in two limits: clean and dirty. If N is in the clean limit ($\ell_N \gg K^{-1}$), the decay length is given by $K^{-1}(T) = \hbar v_F/(2\pi k_B T)$ in an infinite sample. If N is in the dirty limit ($\ell_N \ll K^{-1}$), the development of a nonzero order parameter in N is controlled by a diffusion process [69], and is given by $K^{-1}(T) = (\hbar D/2\pi k_B T)^{1/2}$, where $D = v_F \ell_N / 3$ is the diffusion constant, v_F the Fermi velocity and ℓ_N the electron mean free path of the N metal. These results apply to N metals with $V \le 0$, i.e., those which do not superconduct at any temperature in isolation. If N is a superconductor with $0 < T_{cN} <$

T_{cS}, these results must be modified so that the divergence of K^{-1} takes place at T_{cN}, a phenomenon equivalent to the critical opalescence behavior found at second order phase transitions. Then $K^{-1}(T)$ is given by the solution to [71]

$$\ln \frac{T}{T_{cN}} = \psi\left(\frac{1}{2}\right) - \psi\left(\frac{1}{2} - \frac{\hbar DK^2}{4\pi k_B T}\right) \tag{1.15}$$

where ψ is the digamma function. In the dirty limit, this behaves approximately as $(T - T_{cN})^{-1/2}$. A similar expression behaving approximately as $(T - T_{cN})^{-1}$ is appropriate for the clean limit.

Later, de Gennes produced a landmark work in which he expanded on the work of Werthamer [43]. Here he emphasized that in an inhomogeneous system such as an S/N bilayer, optimum electron pairing is no longer obtained by pairing one electron in state **k** with another in the time-reversed state **-k**, as is the case in a homogeneous superconductor. This fact led to the realization that the gap in the density of states, which can be treated as an order parameter in a homogeneous superconductor, is not an appropriate order parameter for S/N systems. Instead, the pair potential $\Delta(\mathbf{r}) = V(\mathbf{r})\langle\psi_\uparrow(\mathbf{r})\psi_\downarrow(\mathbf{r})\rangle$ is appropriate. De Gennes then showed that if this quantity depends on one spatial coordinate only (usually the case), then the gap in the spectrum of excitations in an S/N bilayer is equal to the minimum of $\Delta(\mathbf{r})$ in the sample. However, he also stated that if V=0 in the normal metal layer, there can be no gap in N. This idea would contradict later tunneling results, which showed that a gap in Cu does develop in proximity contact to Pb, though Cu is never observed to superconduct in isolation [24].

De Gennes made clearer the notion that the solution of Gor'kov's equation (1.12), at temperatures far from T_c, involves including more terms in the expansion of the kernel $K(\mathbf{r},\mathbf{r}')$. In Fourier space, this corresponds to many different decay lengths, of which the single frequency approximation decay length K^{-1} is only the one with the longest range. Thus in the region of N near the interface these other decay lengths play

27

an important role below T_c. The theory of Werthamer applies only far away where these shorter-range decay lengths are unimportant.

The behavior at very low temperatures was examined by Falk at around the same time [44], using the same Gor'kov equation. He showed that the decay of the pair potential $\Delta(r)$ became a power-law $\Delta(r) \sim 1/r$ instead of the exponential behavior predicted near T_c. Although he did not specifically give a length scale over which this dependence occurred, he still recognized that the exponential variation of $\Delta(r)$ was very much an effect of a linear perturbation, valid in the dirty limit and near T_c only.

A theory of the excitation spectrum of a normal metal slab deposited on a superconducting substrate was then constructed by de Gennes and St. James [21]. By solving the Bogoliubov-de Gennes equations [63-64] for energies $\varepsilon < \Delta$, they found that there were states at arbitrarily small energies if the electron-electron interaction V were negligibly small, as well as discrete bound states. These were supposedly seen in the oscillations of $d^2 I/dV^2$ observed by McMillan and Rowell [22].

The interesting aspect of the density of states given by de Gennes and St. James is that the proximity-coupled normal metals are evidently an example of gapless superconductivity which is **not** caused by an interaction that breaks time-reversal symmetry. This point was explored by Fulde and Maki [18]. They essentially found that pair breaking effects caused by a metallic contact occurred because of the spatial dependence of the order parameter, analogous to the current-carrying case in a homogeneous superconductor [72]. The only difference is that in the proximity effect a finite extra momentum **k** is introduced to all states via matching of boundary conditions at the S/N interface, while in the current-carrying case it is introduced externally by the applied current.

In 1975, further substantial theoretical progress on the proximity effect, this time with the aid of computers, was made. In that year, Silvert [73] published work in which computers were used to perform a variational calculation involving Gor'kov's integral

28

equation (1.12), without the restrictive approximations necessary for analytical treatment. It was found that while diffusion-based theories were fine for very thick normal films away from the S/N interface, the order parameter varied much more rapidly near the S/N interface than was predicted using the one-frequency approximation. Thus for thin films, the diffusion theories of Werthamer [70] and the Orsay group [43] were shown to be unreliable. This was supported later by the work of Mota *et al.* [41], as well as by data presented in this thesis.

Later theory papers [74-75] attempted to solve the problem of $\Delta_N(z)$ in the clean limit; these both used the Green's function method, and did not actually yield a simple expression for $\Delta_N(z)$. Their treatments lie outside the scope of this thesis and are mentioned here just for completeness. Kogan [76] obtained the temperature dependence of the correlation length $\xi_N(T)$ in the normal layer of a proximity system above T_{cN}, valid at any concentration of nonmagnetic impurities. Kresin [77] later raised the important issue of nonlocality in his treatment of electromagnetic screening in S/N bilayers, and, together with Wolf [78], went on to apply the theory of the proximity effect to layered structures in an effort to explain the anomalous behavior of high-temperature superconductors.

Chapter 2
The Parallel-Plate Resonator Technique

2.0 Resonator Description

The measurements presented in this work were performed at microwave frequencies with a resonant length of superconducting transmission line known as a parallel-plate resonator. A detailed diagram is shown in Fig. 2.1. It consists of two nominally identical superconducting films of dimensions roughly 1 cm x 1 cm, placed face-to-face, and separated by a thin layer of dielectric material to provide electrical isolation. This forms a two-conductor parallel-plate transmission line capable of guiding transverse electromagnetic (TEM) waves.

Excitation of such TEM modes is accomplished by placing a short length of microstrip line near one edge of the resonator, achieving capacitive coupling through a small gap (~ 0.1 mm). A second, identical antenna is placed further along the edge to
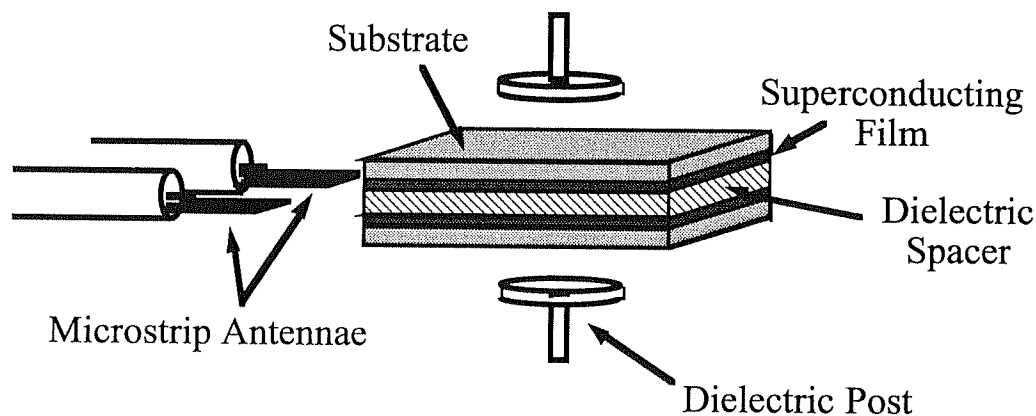
Fig 2.1. Parallel-plate resonator diagram

pick up the signal transmitted through the resonator. The experiment consists of recording the transmission coefficient S_{21}, which is the complex ratio (magnitude and phase) of the received signal at port 2 to the transmitted signal at port 1. All measurements were performed on a Hewlett-Packard 8510C vector network analyzer. The experimental setup is shown in Fig. 2.2.
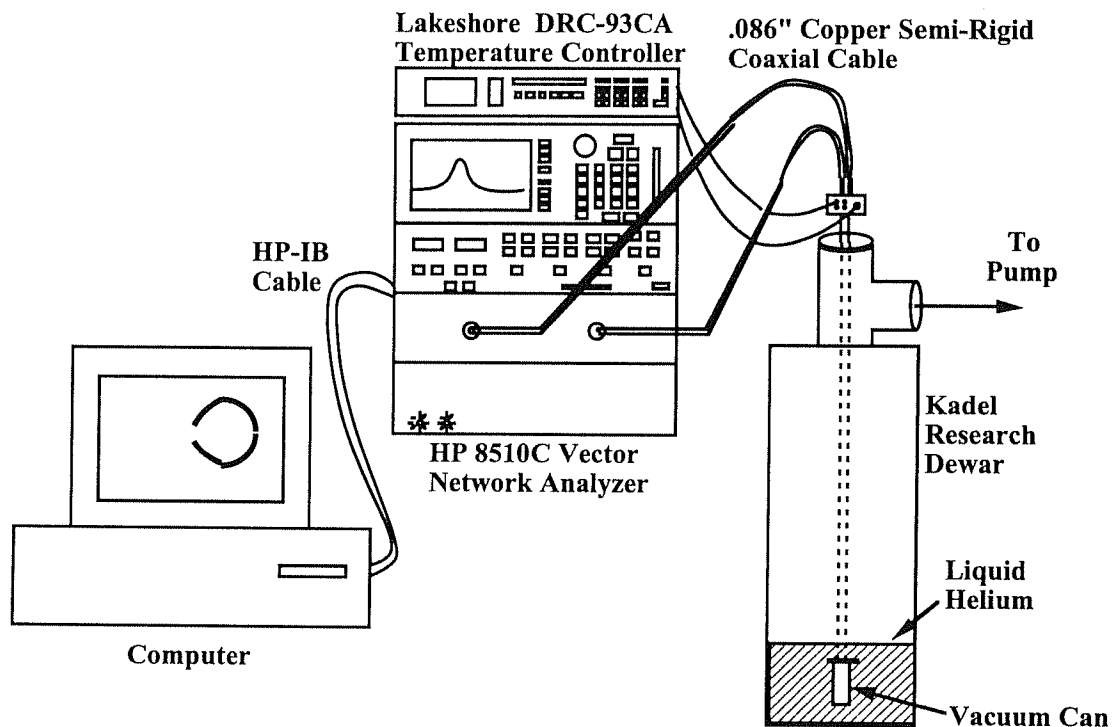
Fig. 2.2 Parallel-plate resonator measurement set-up

2.0.1 Dielectric Spacer

The dielectric spacer must be a low-loss (tan δ < 10^{-4}) material with little temperature dependence of its dielectric properties. It must also survive thermal cycling

31

to 4K and must be able to be cut exactly to the same dimensions as the films under study. Two dielectrics used in this work were Teflon™ and crystalline sapphire. Teflon has tan $\delta \sim 10^{-6}$ and $\varepsilon = 2$; typical fundamental frequencies obtained with it are in the range 10 - 11 GHz. It was cut from large sheets to exactly match each sample's dimensions, and was available in 12.5, 25, 50, 75, and 125 μm thicknesses. Sapphire was less convenient because it could not easily be cut to match sample dimensions. It mainly has the advantage of slowing the propagation of TEM waves ($\varepsilon = 9$), bringing the resonant frequency of a typical resonator down to 5 - 6 GHz. This was below the cutoff frequency of the sample housing in which the resonator was mounted, making these modes readily visible. Another advantage of sapphire is the low dielectric loss, given by tan $\delta \sim 10^{-8}$. However, fringing field losses were found to dominate over dielectric losses with the 125 μm sapphire thickness available. Because sapphire becomes brittle and does not survive thermal cycling when thinned to less than 25 μm, its primary use is for measuring very lossy films where resonant modes cannot be found at the higher frequencies obtained using a Teflon spacer.

2.0.2 Microstrip Antennae

The coupling antennae were made from 75 μm-thick Rogers Duroid™ printed circuit board. The Duroid was first cut into strips of width .086" and length 1 cm. Then one side was coated with GE varnish to protect it during etching. A thin strip of tape of width .030" was glued down the middle of the strip on the opposite side. The strip was then dipped into ferric chloride etchant, leaving only the .030" wide strip of Cu. After removing the GE varnish from the protected side (ground plane), the microstrip was cut to length $\sim$ 0.3 cm and soldered onto the end of .086" ISOCORE semirigid Cu coaxial cable with the center pin protruding .050". The microstrip signal line was soldered to the coax center pin; the ground plane was attached to the coax outer conductor. These microstrips were made in an amateur fashion without precise photolithographic

patterning. They lasted for ~ 20 measurements before fatiguing and breaking.

2.0.3 Microwave Cryostat

All parallel-plate resonator measurements were made using a cryogenic probe submerged in a liquid helium bath. A 3/4" stainless steel tube carried the two coaxial cables and the thermometer and heater wiring down to the sample stage. Two 2" lengths of coaxial cable were used at the low-temperature end of the cryostat, connected with 3.5 mm SMA connectors to the main cables running the length of the probe. The room-temperature end of the cryostat was fitted with positioning micrometers, so that coupling to the resonator could be physically varied in-situ. The positions of both microstrip antennae could be varied independently by as little as .01".

The measurements were performed using two versions of this cryostat--one for quick sample characterization and one for precise measurements. The quick measurement cryostat ("dipping probe") was dunked directly into a liquid He storage dewar. No vacuum can was placed around the sample housing, so this method was used only to screen samples for low surface resistance. More precise measurements were performed using a vacuum can with a crushed indium seal. This was placed in a research dewar, which could be cooled to 2K by pumping on the He bath. Helium has a strongly temperature-dependent dielectric constant below 10K, so measurement in weak vacuum (~ 10^{-3} Torr) was necessary to prevent the temperature dependence of ε(He) from influencing the resonant frequency of the resonator. In order to maintain this vacuum inside the cryostat while adjusting the coupling to the resonator, a home-made dynamic seal made from a Teflon™ disk was used. Undersized holes were drilled in a 1/8" thick slab of Teflon, and the .086" coaxial cables inserted. Then the Teflon disk was compressed by a retaining ring bolted on top. The Teflon flowed around the coaxes, providing a tight, dynamic seal which held 10^{-3} Torr. A separate hole into the vacuum environment for thermometer and heater wiring was sealed permanently with Torr-Seal™

33

vacuum epoxy.

2.0.4 Temperature Measurement and Control

The temperature was measured by a Lakeshore DT-470 Si-Ge diode mounted in a hole embedded in the copper sample stage block just above the sample housing. The distance from the diode to the sample was approximately 0.5 cm. This diode can measure temperatures down to 1.4K with a precision of 0.01K. Temperature stability was achieved by heating the sample block with a 25Ω 3W resistor thermally connected with Apiezon N grease while the probe was immersed in liquid helium. For the measurements performed in vacuum a small amount of He exchange gas was admitted into the can to provide better thermal anchoring to the bath. The current through the heater was regulated automatically by a Lakeshore DRC-93C temperature controller. Ramping of the temperature, stabilization, centering of the resonance in the frequency window of the network analyzer, and data transfer were all controlled automatically by computer.

2.1 Parallel-Plate Resonator Theory

2.1.1 Electromagnetic Field Configuration

The parallel-plate resonator is a two-dimensional transmission line capable of supporting transverse electromagnetic (TEM) modes. Assuming perfectly conducting plates and open circuit boundary conditions at the edges, the electric field $E(x,y,t)$ and magnetic field $B(x,y,t)$ can be found by solving the wave equation by separation of variables, as follows:

$$\frac{\partial^2 E_0}{\partial x^2} + \frac{\partial^2 E_0}{\partial y^2} - \frac{\varepsilon}{c^2}\frac{\partial^2 E_0}{\partial t^2} = 0 \qquad (2.1)$$

34

where $\mathbf{E} = \mathbf{z}\, E_0(x,y,t)$. We then separate variables, writing $E_0(x,y,t) = X(x)Y(y)T(t)$. Substituting this into (2.1) and dividing by XYT, we get

$$\frac{1}{X}\frac{\partial^2 X}{\partial x^2} + \frac{1}{Y}\frac{\partial^2 Y}{\partial y^2} - \frac{\varepsilon}{c^2}\frac{1}{T}\frac{\partial^2 T}{\partial t^2} = 0 \tag{2.2}$$

All three terms must be constants, since (2.2) must hold for all (x,y,t) and the three terms are independent of each other. We choose these constants as

$$\frac{1}{X}\frac{\partial^2 X}{\partial x^2} = -k_x^2 \tag{2.3a}$$

$$\frac{1}{Y}\frac{\partial^2 Y}{\partial y^2} = -k_y^2 \tag{2.3b}$$

$$\frac{1}{T}\frac{\partial^2 T}{\partial t^2} = -\omega^2 \tag{2.3c}$$

so that we get the dispersion relation

$$k_x^2 + k_y^2 = \frac{\varepsilon}{c^2}\omega^2 \tag{2.4}$$

Solving the equations (2.3) and employing the boundary conditions that $\mathbf{E}$ must be maximum at $x = 0,a$ and $y = 0,b$, we find

$$X(x) = \cos k_x x, \qquad k_x = \frac{n\pi}{a} \tag{2.5a}$$

$$Y(y) = \cos k_y y, \qquad k_y = \frac{m\pi}{b} \tag{2.5b}$$

$$T(t) = \cos \omega t \tag{2.5c}$$

where n,m = 0,1,2... Thus we have

$$\mathbf{E} = \mathbf{z}\, E_0 \cos \frac{n\pi x}{a} \cos \frac{m\pi y}{b} \cos \omega t \tag{2.6}$$

35

The magnetic field is found from the Maxwell equation $\nabla \times \mathbf{E} = -\partial\mathbf{B}/\partial t$:

$$\mathbf{B} = \frac{E_0 \sin \omega t}{\omega}\left[-\frac{m\pi}{b}\sin\frac{m\pi y}{b}\cos\frac{n\pi x}{a}\,\mathbf{x} + \frac{n\pi}{a}\sin\frac{n\pi x}{a}\cos\frac{m\pi y}{b}\,\mathbf{y}\right] \qquad (2.7)$$

So $\mathbf{E}$ and $\mathbf{B}$ are perpendicular to each other, 90° out of phase, and are related in magnitude by the phase velocity of the waves. A diagram of these modes is shown in Fig. 2.3. This simple picture enables one to roughly calculate the mode frequencies of any sample of interest. For example, a resonator with dimensions ~ 1 cm x 1cm with Teflon dielectric ($\varepsilon = 2$) has fundamental modes [(nm) = (01), (10)] in the neighborhood of 10 - 11 GHz.

(a)   (b)
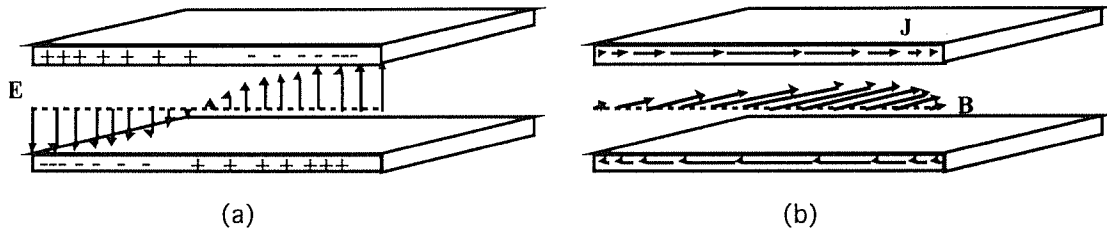
Fig. 2.3. Field configuration of the (01) mode in a parallel-plate resonator. Shown are: (a) the instant at which $\mathbf{E}$ is maximum at the edges, with no current flow (t = 0), and (b) the situation 1/4 cycle later, when maximum current flow and maximum $\mathbf{B}$ at the midpoint of the resonator occur (t = τ/4). At t = t/2, the $\mathbf{E}$ fields and charges are identical to (a), but with opposite sign. At t = 3t/4, $\mathbf{B}$ fields and currents are opposite to those shown in (b).

The assumption of perfectly conducting plates defeats the purpose of the measurement, of course; the whole idea is to measure the surface resistance (loss) and penetration depth (reactance) of the plates. Fringing fields, substrate dielectric constant, and coupling fields also complicate the picture to the extent that the above calculation only predicts the mode frequencies with an accuracy of ±10%. But the essential behavior of the fields is described by Eqs. (2.6) and (2.7).

2.1.2 Magnetic Penetration into Superconducting Plates

If we consider the plates to be real superconducting films, we must relax the assumption of perfect conductivity. This means that electromagnetic fields will penetrate into the plates. The distance they penetrate is called λ, the magnetic penetration depth, and is typically $10^2 \sim 10^3 \text{Å}$ in size. This penetration of field has a small effect on the modes calculated in section 2.1.1, and causes the resonant frequencies of all modes to be lowered a small amount. It is only a perturbation effect, so the basic mode structure still strongly resembles that of Fig. 2.3.

The effect of field penetration into the plates is to increase the inductance per unit length, since extra energy is being stored during an RF cycle in magnetic fields in a sheath of thickness λ just inside the surface of the plates. This is called **magnetic inductance**. In addition, some energy is stored as kinetic energy in the supercurrents that flow to screen out the applied field, known as **kinetic inductance**. These slow the propagating TEM waves slightly.

To calculate this effect, consider the situation shown in Fig. 2.4. The RF magnetic field is parallel to the superconducting film in the region between the plates. Outside the resonator the magnetic field is nearly zero because of currents flowing in the opposite direction in the other film.

Inside the film we have the Maxwell equation

$$\nabla \times \mathbf{B} = \mu_0 \mathbf{J} \tag{2.8}$$

where $\mathbf{J}$ is the total current density. We neglect the displacement current because, to zeroth order, $\mathbf{E} = 0$ inside the film. We neglect normal currents for the same reason, so that $\mathbf{J} \cong \mathbf{J_s}$, the supercurrent density. We then combine (2.8) with the second London equation

$$\nabla \times \mu_0 \lambda^2 \mathbf{J_s} = -\mathbf{B} \tag{2.9}$$

37
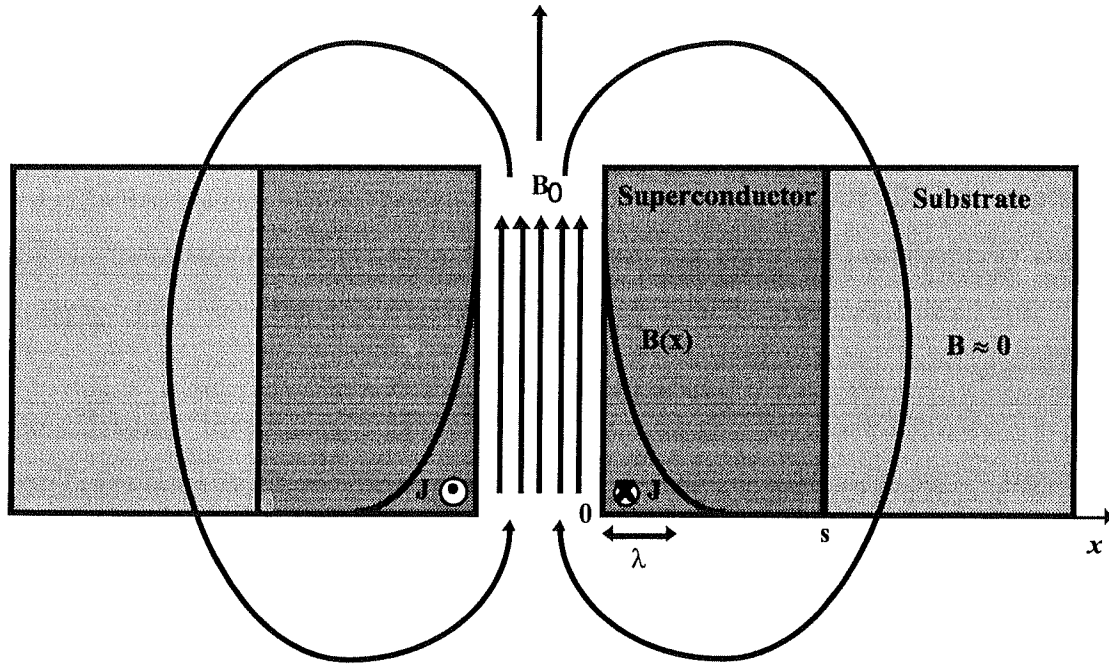
Fig. 2.4 Magnetic field profile inside superconducting plates and magnetic field lines outside. The shielding currents flow in opposite directions, creating a constant magnetic field $\mathbf{B_0}$ between the plates, and forcing the condition $\mathbf{B} \approx 0$ at the back surface of the films.

and arrive at the equation which describes Meissner screening:

$$\nabla^2 \mathbf{B} = \frac{\mathbf{B}}{\lambda^2}$$ (2.10)

The solution which matches the boundary conditions B(z=s) = 0 and B(z=0) = B_0 is:

$$B(z) = B_0 \frac{\sinh\left(\frac{s-z}{\lambda}\right)}{\sinh\left(\frac{s}{\lambda}\right)}$$ (2.11)

The supercurrent, calculated from Eq. (2.8), is:

38

$$J_s(z) = -\frac{B_0}{\mu_0\lambda}\frac{\cosh\left(\frac{s-z}{\lambda}\right)}{\sinh\left(\frac{s}{\lambda}\right)} \tag{2.12}$$

To calculate $\mathcal{L}$, the inductance per unit length of the resonator, we set the total energy stored equal to $\mathcal{L}I^2/2$, where I is the total current flowing through an element of length in a film of width W:

$$\frac{1}{2}\mathcal{L}I^2 = W\int_{-\infty}^{+\infty}\frac{B^2(z)}{2\mu_0}\,dz + W\int_{-\infty}^{+\infty}\frac{\mu_0\lambda^2 J_s^2(z)}{2}\,dz \tag{2.13}$$

The first term in (2.13) is the magnetic inductance; the second is the kinetic inductance. Since $\mathbf{B} = 0$ outside the resonator, the integrals run over the two film thicknesses and the space between the plates. Evaluating the first integral, we have

$$\frac{1}{2}\mathcal{L}_{mag}I^2 = \frac{B_0^2}{2\mu_0}Wd + \frac{B_0^2 W}{\mu_0\sinh^2\left(\frac{s}{\lambda}\right)}\left[-\frac{s}{2} + \frac{\lambda}{4}\sinh\left(\frac{2s}{\lambda}\right)\right] \tag{2.14}$$

while the second integral evaluates to

$$\frac{1}{2}\mathcal{L}_{kin}I^2 = \frac{B_0^2 W}{\mu_0\sinh^2\left(\frac{s}{\lambda}\right)}\left[\frac{s}{2} + \frac{\lambda}{4}\sinh\left(\frac{2s}{\lambda}\right)\right] \tag{2.15}$$

Adding these two terms together and using Ampere's Law to find $I = WB_0/\mu_0$, we get an expression for the total inductance per unit length:

$$\mathcal{L} = \frac{\mu_0}{W}\left\{d + \lambda\frac{\sinh\left(\frac{2s}{\lambda}\right)}{\sinh^2\left(\frac{s}{\lambda}\right)}\right\} \tag{2.16}$$

It can be shown that the capacitance per unit length is $C = \varepsilon_r\varepsilon_0 W/d$, this result being unaffected by magnetic penetration into the plates to zeroth order. We thus can calculate

the phase velocity of waves traveling between the plates:

$$v_{ph} = \left(\mathcal{L}C\right)^{-1/2} = \frac{c/\sqrt{\varepsilon_r}}{\sqrt{1 + \dfrac{\lambda}{d}\dfrac{\sinh\left(\dfrac{2s}{\lambda}\right)}{\sinh^2\left(\dfrac{s}{\lambda}\right)}}} \qquad (2.17)$$

Since the resonant frequency is proportional to the phase velocity, we arrive at

$$f_0 = \frac{f_a}{\sqrt{1 + \dfrac{2\lambda}{d}\coth\left(\dfrac{s}{\lambda}\right)}} \qquad (2.18)$$

where the denominator of (2.17) has been simplified. Here f_0 is the resonant frequency and $f_a = c/\sqrt{\varepsilon_r}$ is the "ideal" resonant frequency in the absence of magnetic field penetration, i.e., if λ were zero. The second term in the denominator of (2.18) thus describes the effect of magnetic field penetration on the resonant frequency. It is important to note, however, that since λ is never zero, experimental determination of the absolute magnitude of λ is difficult, though small changes in λ of the order of 1 Å are easy to detect.

2.1.3 RF Losses in Superconducting Films

Magnetic field penetration is also accompanied by RF losses, which occur at finite frequency because of the presence of quasiparticles thermally activated out of the superconducting condensate. An electric field $E_{\parallel}$ arises when the supercurrent is accelerated back and forth by the alternating magnetic field, according to the first London equation:

$$E_{\parallel} = \frac{d}{dt}\left(\mu_0\lambda^2 J_s\right) \qquad (2.19)$$

This electric field, parallel to the plane of the film, then drives a normal current J_n of quasiparticles given by $J_n = \sigma_1 E_{\parallel}$, where σ_1 is the real part of the conductivity. This

40

latter effect causes the RF loss, and can be described by a net component of the time-averaged Poynting vector directed into the film. It can be shown [79] that the total time-averaged power lost per radian of oscillation through both plates of the parallel-plate resonator via this mechanism is given by

$$\langle P_{dis} \rangle = 2 \left(\frac{1}{2} \right) \left(\frac{1}{2} \right) \frac{WL}{\omega} \text{Re} \int_0^s \mathbf{J}_{total} \cdot \mathbf{E} \, dz \qquad (2.20)$$

where the factors of 1/2 and 2 come from time and space averaging, and from the fact that there are two films.

The quantity actually measured experimentally is the quality factor Q, which is related to the bandwidth Δf of the resonance by $Q = f_0/\Delta f$. The Q is defined as the energy stored in the resonator divided by the energy dissipated per radian of oscillation. But the intrinsic quantity of interest which describes the electromagnetic response of a superconducting film is the surface resistance R_s. It is defined as

$$R_s = \mu_0 \, \text{Re} \left(\frac{E_\parallel(0)}{B_\parallel(0)} \right) \qquad (2.21)$$

and is a quantity independent of film dimensions that characterizes the lossiness of the sample. If we assume for the moment that all other loss mechanisms (such as radiation or coupling losses) are negligible, we can derive the relationship between R_s and the measured Q.

The energy stored in the resonator is a constant quantity, stored alternately in magnetic and electric fields during an RF cycle. If we choose the instant of maximum magnetic field storage, the energy stored is

$$U = d \int_S \frac{B_0^2(x,y)}{2\mu_0} \, dx \, dy \qquad (2.22)$$

41

We neglect the extra energy stored inside the plates calculated in section 2.1.2, since it is a very small contribution. Using (2.7), we evaluate (2.22), yielding

$$U = \frac{dWLB_0^2}{4\mu_0} \qquad (2.23)$$

The plates carry sheet current **K**, which leads to power dissipation of $K^2 R_s$ per unit area. Thus the time-averaged power dissipation per radian in both films is given by

$$\langle P_{dis} \rangle = 2 \left(\frac{1}{2}\right)\left(\frac{1}{2}\right) \frac{K^2 R_s LW}{\omega} \qquad (2.24)$$

where again the factors of 2 and 1/2 come from time and spatial averaging, and two films. Recalling that $K = I/W = B_0/\mu_0$, we can then calculate Q:

$$Q = \frac{U}{\langle P_{dis} \rangle} = \frac{\pi \mu_0 f_0 d}{R_s} \qquad (2.25)$$

We can calculate the surface resistance from (2.20) by identifying that equation with (2.24) and rearranging:

$$R_s(T) = \mu_0^2 \, \mathrm{Re} \int_0^s \frac{\mathbf{J} \cdot \mathbf{E}_{\parallel}}{B_0^2} \, dz \qquad (2.26)$$

Assuming all fields and currents are proportional to $e^{i\omega t}$, we calculate the electric field from the total current:

$$\mathbf{J}(z) = \sigma_1 \mathbf{E}_{\parallel}(z) + \frac{1}{i\omega\mu_0\lambda^2} \mathbf{E}_{\parallel}(z) \qquad (2.27)$$

42

Taking the real part of $\mathbf{J} \cdot \mathbf{E}$, we arrive at an integral for R_s:

$$R_s(T) = \int_0^s \frac{\sigma_1}{\sigma_1^2 + \left(\frac{1}{\omega\mu_0\lambda^2}\right)^2} \frac{\cosh^2\left(\frac{s-z}{\lambda}\right)}{\lambda^2 \sinh^2\left(\frac{s}{\lambda}\right)} dz \qquad (2.28)$$

The solution is

$$R_s = \frac{\sigma_1}{\sigma_1^2 + \left(\frac{1}{\omega\mu_0\lambda^2}\right)^2} \frac{1}{2\lambda^2}\left[\lambda \coth\left(\frac{s}{\lambda}\right) - s\, \mathrm{csch}^2\left(\frac{s}{\lambda}\right)\right] \qquad (2.29)$$

This result was originally derived by N. Klein et al. [80] and reduces to the familiar result

$$R_s = \frac{\mu_0^2\omega^2\lambda^3\sigma_1}{2} \qquad (2.30)$$

in the limits $\sigma_1 \ll \sigma_2$ and $s \gg \lambda$.

2.1.4 Extrinsic Losses and Resolution Limits for R_s

The aim of the parallel-plate technique is to arrange matters so that the electromagnetic response of the superconducting plates dominates the behavior of the resonator. In other words, the conductor loss in the plates must be the primary mechanism for power dissipation, and changes in magnetic field penetration the dominant cause of resonant frequency shift in the resonator. There are, however, extrinsic losses which can compete with the intrinsic film losses and even dominate the resonator behavior, particularly if the films are of very high quality. Each source of loss has its own dependence on the spacer thickness d, however, so that by varying d these factors

43

can be isolated.

The three primary sources of extrinsic loss are fringing field loss (radiation), dielectric loss, and coupling loss. The latter can be minimized by weakening the coupling between the microstrip antennae and the resonator. The other two sources are always present, and must be measured.

These two sources of extrinsic loss constitute extra energy lost from the resonator, and hence contribute to the $\langle P_{dis} \rangle$ term in the denominator of Eq. (2.25). This can be represented as a contribution to $1/Q$, as follows [55]:

$$\frac{1}{Q} = \alpha d + \tan \delta + \frac{R_s}{\pi \mu_0 f_0 d} \qquad (2.31)$$

In Eq. (2.31), the first term represents energy lost through fringing fields at the ends of the resonator. The value of α is determined by the coupling to the environment outside, the conductivity of the housing walls, substrate effects, etc. Though the energy lost is proportional to d^2 [81], this is balanced by the stored energy in the resonator, which grows linearly with d, giving a net contribution to $1/Q$ which is proportional to d.

The second term, $\tan \delta$, represents the loss caused by rapid alternating repolarization of the dielectric between the plates, and is equal to the ratio

$$\tan \delta = \frac{|\text{Im}(\varepsilon)|}{|\text{Re}(\varepsilon)|} \qquad (2.32)$$

Since the imaginary part of ε is proportional to the energy lost and the real part proportional to the electric field energy stored, this ratio already satisfies the definition of $1/Q$, and hence contributes an amount to the total $1/Q$ that is independent of d.

By varying the thickness of the dielectric spacer, one can isolate these three contributions and obtain values for α, $\tan \delta$, and R_s by fitting the quantity d/Q to a quadratic function of d, as shown by Taber [55]. This yields the true value of R_s,

separated from extrinsic losses. In practice, therefore, it is always better to measure a sample with the thinnest spacer possible, so that these extrinsic losses are minimized. At 12.5 µm spacing, the extrinsic losses can amount to a loss corresponding to as low as ~ 5 µΩ at 11 GHz. Measuring samples with R_s < 5 µΩ then becomes difficult, and thinner, less lossy dielectrics would be needed.

Figure 2.5 shows the d-dependence of 1/Q for a resonator comprised of Nb films on Si, using Teflon spacers. It is plotted as d/Q vs. d in order to obtain a quadratic dependence on d, so that a parabolic fit yields the coefficients α and tan δ, as seen by

The plot shows d/Q (µm) on the vertical axis (0.000 to 0.015) versus Dielectric thickness d (µm) on the horizontal axis (0 to 80), with annotations:

tan δ = 1 x 10^{-6}
α = 2.2194 x 10^{-6} µm^{-1}
R_s = 8.47 µΩ
f = 11.5 GHz
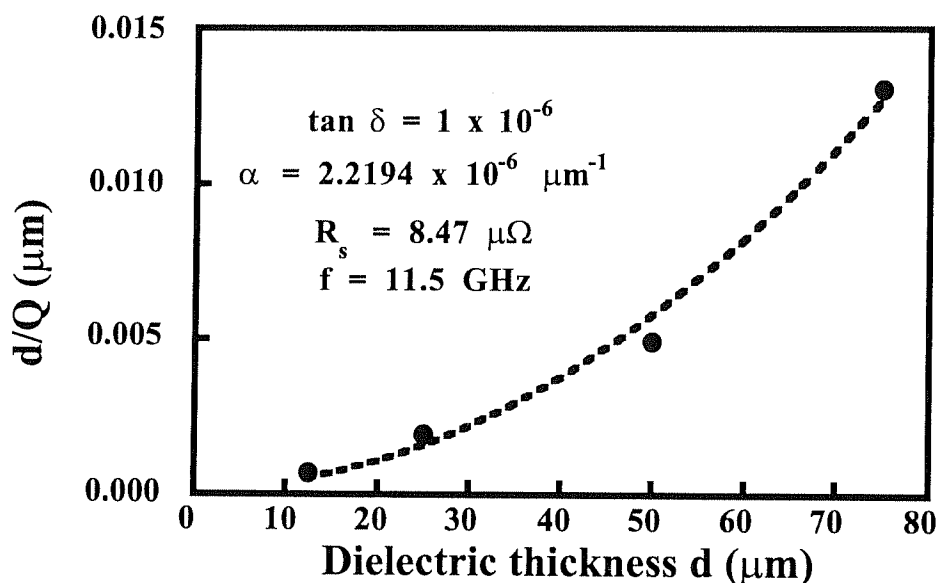
Fig. 2.5. Dependence of 1/Q on spacer thickness d for Nb films on Si substrates, at 2K. This plot is used to evaluate the relative amounts of loss caused by fringing field loss, dielectric loss, and the samples themselves in the parallel-plate measurement.

inspection of (2.31). The Nb samples measured in Fig. 2.5 thus had an intrinsic surface resistance R_s = 8.47 µΩ at 2.5K, which is the value one would obtain by using a spacer thickness of 0 µm, an impossibility. At 12.5 µm dielectric thickness, the contributions to the measured loss from dielectric loss and fringing field loss are 0.58 µΩ and 16.2 µΩ, respectively. Thus, even with the thinnest spacer available, radiation from fringing fields causes most of the measured loss. For thicker spacers, these numbers only get worse: d = 25 µm, 1.16 µΩ and 64.95 µΩ; d = 50 µm, 2.32 µΩ and 259.8 µΩ; d = 75 µΩ, 3.48

$\mu\Omega$ and 584.5 $\mu\Omega$, respectively. These numbers are very significant; radiation losses from fringing fields are far and away the largest cause of loss in the measurement, at least for the Nb samples shown here. Though this is not always the case for the thinnest spacer used (it depends on the kind of substrate, the lossiness of the films, the housing walls, etc.), it is nearly always so for thicker dielectric spacers. Quantification of each source of loss by the above method is therefore crucial when the superconducting films being studied are not very lossy and do not dominate the RF loss in the system.

2.2 Surface Impedance of Superconducting Films

Below are surface impedance data, shown as surface resistance R_s and penetration depth λ, for several superconducting samples. Where possible, fits to appropriate theory curves are provided, and quantities of interest are given.

2.2.1 Nb

Niobium is the "standard" to which many microwave measurements are compared. Though it is somewhat challenging to prepare samples with good microwave properties, they behave in a well-understood manner suitable for validating one's experimental technique. Shown in Fig. 2.6 are the surface resistance and penetration depth of 3000Å-thick Nb films grown on Si substrates by DC magnetron sputtering. The films were produced in 4 mTorr flowing Argon, after first attaining a chamber base pressure of 4×10^{-8} Torr. The substrate temperature was elevated to $450°$ C, and the high purity Nb target was sputtered using 1200W power. The low base pressure (to remove damaging oxygen) and the high substrate temperature (to evolve impurities from the substrate surface) were very important in producing high quality films with superior microwave properties. As seen in Fig. 2.6, these samples had a penetration depth $\lambda(0) =$ 353 Å $\pm$ 10 Å and T_c = 9.17 K $\pm$ .03K, found by fitting to the BCS temperature

46

dependence tabulated by Mühlschlegel [82]. The fit to this dependence is extremely good, and these numbers correspond closely to the accepted bulk value $\lambda(0) = 390$ Å and to the observed transition temperature of 9.2 K. The surface resistance drops to a value of 8.47 $\mu\Omega$ at 2.5 K and has the characteristic temperature dependence $R_s \sim \exp(-\Delta/k_B T)$, with gap ratio $2\Delta/k_B T_c = 3.6 \pm 0.1$, also in agreement with the BCS value of 3.5. These results provide a high level of confidence in the parallel-plate technique.
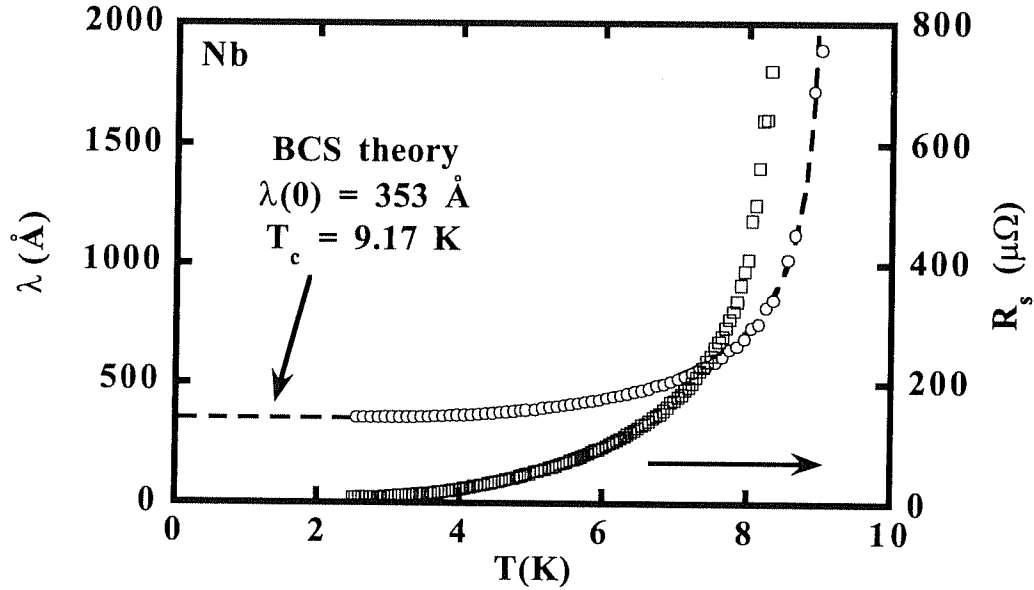
Fig. 2.6 Surface resistance (squares) and penetration depth (circles) for a 3000Å-thick Nb film on Si. The value of R_s at 2.5K is only 8.47 $\mu\Omega$ at 11.5 GHz, and varies as $\exp(-\Delta/k_B T)$ at low temperatures. The penetration depth is fit to the BCS temperature dependence tabulated by Mühlschlegel, and the parameters $\lambda(0) = 353 \pm 10$ Å and $T_c = 9.17 \pm .03$ K provide the best fit.

2.2.2 NbN

Niobium nitride films are of great technological interest because they have a much higher T_c (≤ 17 K) than elemental superconductors such as Nb. Though some have reported growing single-crystalline films of NbN [83], which they claim have penetration depths of $\lambda(0) \sim 1000$Å, most samples are granular and display penetration depths of

$\lambda(0) \sim 3000 - 4000\text{Å}$. Though this large penetration depth is less desirable than that of other superconductors, the incredibly low surface resistance found in properly grown samples still holds great interest for microwave devices[84]. The main reason for the low surface resistance is that despite the large value of λ (recall that $R_s \sim \lambda^3$), the gap over which lossy excitations must be excited is larger ($2\Delta/k_B T_c \approx 4.1$). This, coupled with a poor normal state conductivity and the fact that the reduced temperature T/T_c is lower than in elemental superconductors like Nb at that same temperature owing to the higher T_c, mean that the real part of the conductivity, σ_1, can be much smaller than in Nb, compensating for the difference in λ.

The penetration depth and surface resistance of 8000Å-thick NbN films grown on oxidized Si substrates by DC reactive magnetron sputtering are shown in Figs. 2.7 and 2.8. In Fig. 2.7, NbN was grown directly on the substrate, while in Fig. 2.8, a 200Å-thick Nb underlayer was deposited first, followed by 8000Å NbN. The purpose of comparing the two was to look for an improvement in microwave properties correlated with the improvement in crystalline orientation and the decrease in DC transition width observed in samples with the Nb underlayer [85].

As seen by comparing Figs. 2.7 and 2.8, the use of the Nb underlayer did not improve the surface resistance, which was already quite low ($< 6~\mu\Omega$) in the sample made directly on Si. Instead, the sample with the 200Å Nb underlayer had a residual surface resistance of $22~\mu\Omega \pm 4~\mu\Omega$, presumably associated with losses in the Nb. However, the penetration depths were equal to within experimental error ($\lambda(0) \sim 3800\text{Å}$) and the gap ratios derived from fitting to the temperature dependence[86]

$$\frac{\lambda(T)}{\lambda(0)} = 1 + \sqrt{\frac{\pi\Delta(0)}{2k_B T}} \exp\left(-\frac{\Delta(0)}{k_B T}\right), \qquad T < \frac{T_c}{2} \qquad (2.33)$$

were found to be $2\Delta/k_B T_c = 4.1 \pm 0.1$ in both cases. This indicates that no significant difference in superconducting properties resulted from improving the crystalline structure

48
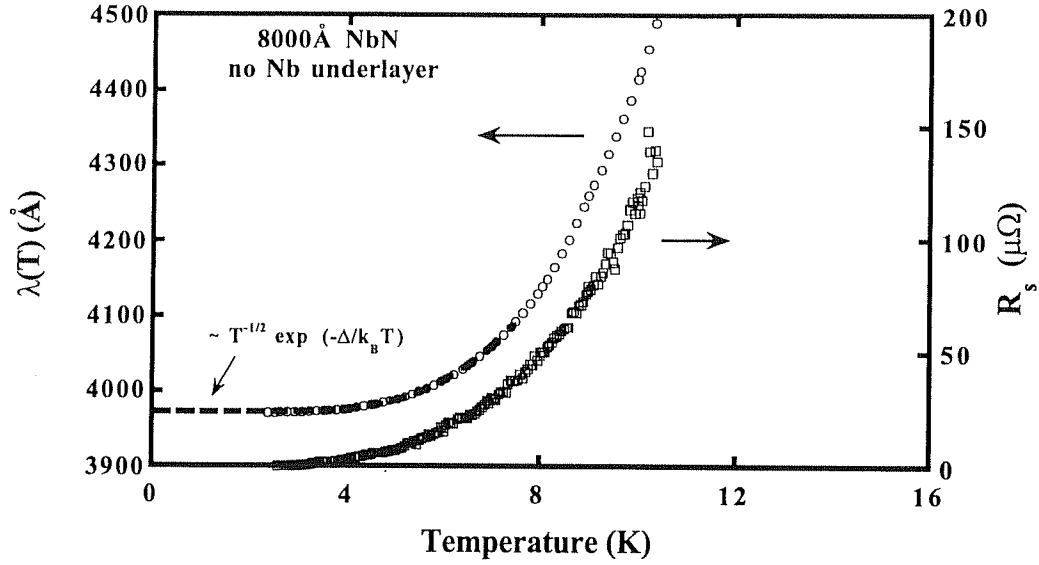
Fig. 2.7. Penetration depth and surface resistance for 8000Å NbN films on Si with no Nb underlayer, at 10.54 GHz. Dashed line is a fit to the dependence $\lambda(T)/\lambda(0) \sim 1 + T^{-1/2} \exp(-\Delta/k_B T)$. The fit yields $\lambda(0) = 3970\text{Å} \pm 200\text{Å}$ and gap ratio $2\Delta/k_B T_c = 4.1 \pm 0.1$. The surface resistance goes below the resolution limit of 6 $\mu\Omega$ at 4.2K.
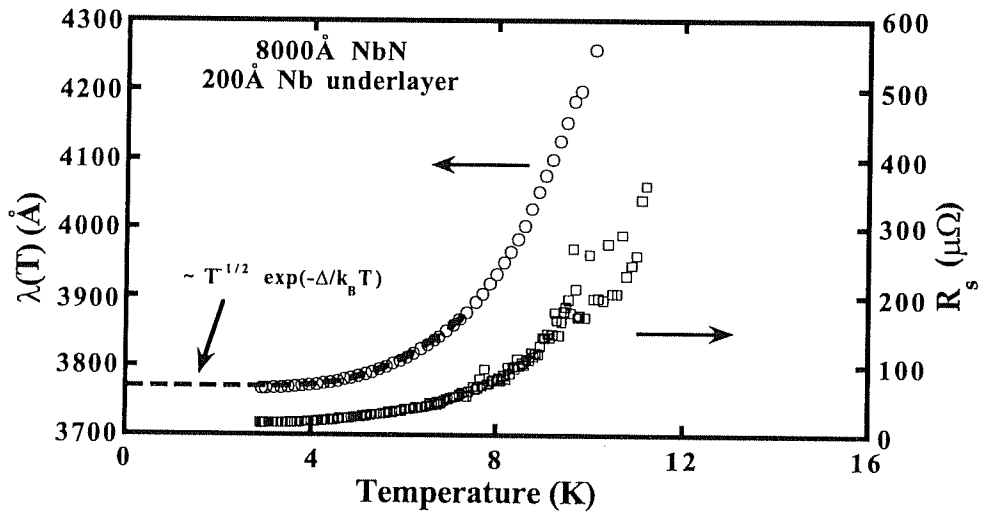
Fig. 2.8. Penetration depth and surface resistance for 8000Å NbN films on Si with 200Å Nb underlayer, at 11.39 GHz. Dashed line is a fit to the dependence $\lambda(T)/\lambda(0) \sim 1 + T^{-1/2} \exp(-\Delta/k_B T)$. The fit yields $\lambda(0) = 3770\text{Å} \pm 200\text{Å}$ and gap ratio $2\Delta/k_B T_c = 4.1 \pm 0.1$. The surface resistance hits a residual value of 22 $\mu\Omega \pm 4\ \mu\Omega$ at 3K. This is presumed to be related to the Nb underlayer.

with the Nb underlayer; the extra losses evident in Fig. 2.8 are likely due to the Nb underlayer itself, not changes in the crystalline order of NbN induced by it. The measured penetration depth and gap ratio are in full agreement with previous measurements performed by tunneling and other methods [87-88].

2.2.3 $Ba_{1-x}K_xBiO_3$

This bismuthate superconductor is of interest because it too has a relatively high T_c (15 - 26 K) and has a coherence length suitable for fabrication of tunnel junctions[89]. It is known to be a cubic superconductor and its behavior is consistent with BCS theory [85]. However, no single best method of fabrication has been found, with the result that sample properties, both microwave and otherwise, can vary greatly from sample to sample. Measurements performed by the author, when published in early 1994 [85], gave the lowest surface resistance (400 $\mu\Omega$ at 6.46 GHz) ever measured in this material.

The samples were made at AT&T Bell Laboratories by molecular beam epitaxy (MBE) [90] on (100) MgO substrates. They were 3600Å thick, had potassium doping level x = 0.49, and had a T_c = 17.2 K, typical of films grown by MBE. The penetration depth and surface resistance of these samples at 6.46 GHz are shown in Fig. 2.9.

As seen in Fig. 2.9, these samples obeyed the asymptotic BCS temperature dependence for the penetration depth, given by Eq. 2.33, with parameters $\lambda(0)$ = 3300Å ± 200Å and $\Delta(0)$ = 2.82 ± 0.35 meV. The latter quantity leads to a gap ratio $2\Delta/k_BT_c$ = 3.5 ± 0.5. The surface resistance was also fit to this theory for T < T_c/2, using the expression [87]:

$$R_s - R_s(0) \sim \frac{1}{T} \exp\left(-\frac{\Delta(0)}{k_BT}\right), \qquad T < \frac{T_c}{2} \qquad (2.34)$$

The gap ratio $2\Delta/k_BT_c$ = 3.5 ± 0.5 agreed with the value found by fitting $\Delta\lambda$ to Eq. 2.33. It also is in full agreement with tunneling measurements on polycrystalline pellets[91],

single crystals and thin films in $Ba_{1-x}K_xBiO_3/Au$ junctions[92], sputtered films in $Ba_{1-x}K_xBiO_3/I/Au$ S-I-N junctions[93], all-$Ba_{1-x}K_xBiO_3$ thin film junctions[94], and with infrared reflectivity results[95]. The penetration depth $\lambda(0) = 3300\text{Å}$ also agreed well with the value of 3400Å obtained by muon-spin-rotation[96]. Though the data
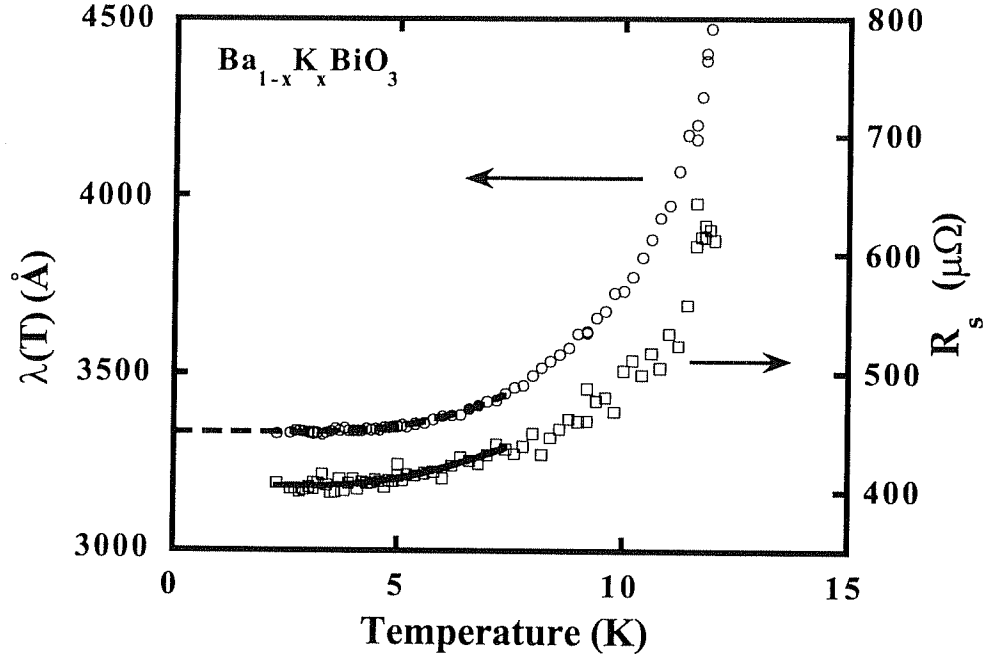
Fig. 2.9. Penetration depth and surface resistance of a 3600Å-thick $Ba_{1-x}K_xBiO_3$ film on MgO, at 6.46 GHz. The solid and dashed lines are BCS asymptotic fits for $T<T_c/2$ using Eq. 2.33. The gap ratio found from both of these fits was $2\Delta/k_BT_c = 3.5 \pm 0.5$. This was the lowest surface resistance ever measured in this material, $R_s = 400\ \mu\Omega$ at 6.46 GHz and 2.2 K. When scaled by $R_s \sim \omega^2$, it yields R_s (10 GHz) $= 958\ \mu\Omega$.

likely that further materials improvements will decrease R_s further.

2.2.4 $YBa_2Cu_3O_{7-\delta}$

By far the most widely-studied high-T_c superconductor owing to its ease of fabrication, this material behaves unlike the previous three superconducting materials in microwave measurements. Here, 3000Å-thick samples were grown by Chuhee Kwon at

Maryland, on $LaAlO_3$ substrates by pulsed-laser deposition [97-98] and had T_c = 90 K as measured by AC susceptibility. The surface impedance data are shown in Fig. 2.10, measured at 11.9 GHz. These samples were found to have very low intrinsic surface resistance R_s < 6 $\mu\Omega$ at 4.2K after the effects of dielectric and radiation loss were subtracted as described in section 2.1.4; these two extrinsic sources of loss contributed significantly (~ 70 $\mu\Omega$ total at 4.2K) to the measured loss, probably because of the involvement of the substrate (ε ~ 23) in the fringing field configuration.

As seen from Fig. 2.10, however, the penetration depth does not obey the standard BCS Mühlschlegel [82] temperature dependence the way Nb and other conventional superconductors do. Instead of varying only exponentially slowly with temperature as T -> 0, we find the dependence $\lambda(T)$ ~ T. The best fit to BCS theory is not very good, and yields parameter values of $\lambda(0)$ = 2580Å and T_c = 100.1 K, not in keeping with the more accepted value $\lambda(0)$ ~ 1250Å [99] and the transition temperature T_c = 90 K measured by AC susceptibility. In fact, without knowing the correct temperature dependence to fit $YBa_2Cu_3O_{7-\delta}$ penetration depth data to, we are not able to deduce the absolute value of $\lambda(0)$ at all; hence the plot of penetration depth change $\Delta\lambda$ vs. T in Fig. 2.10.

Data such as that shown in Fig. 2.10 has been at the root of much of the debate over the nature of the pairing state in cuprate superconductors, an issue still not completely resolved. The linear temperature dependence of λ at low temperatures is consistent with a direction-dependent energy gap which goes to zero at some points (nodes) on the Fermi surface. Since with such a gap function there are always excited states available at arbitrarily low energies for Cooper pairs whose momenta lie in the direction of these nodes, the depletion of the superfluid density, measured by the penetration depth, proceeds linearly with temperature, rather than obeying the exponentially slow depletion associated with a fully gapped spectrum. This so-called "d-wave" pairing has been postulated by some [100]; microwave measurements are often

called upon to address this issue because of the inherent high sensitivity to small changes in penetration depth which must be resolved in order to distinguish an exponential dependence from a power law at low temperature. It should be noted, however, that interpretation of microwave experimental results on $\lambda(T)$ should be performed only when careful consideration has been given to what is actually being measured, namely, a layer of thickness λ at the surface of the superconductor. In this sense, microwave experiments cannot claim to measure intrinsic, bulk properties of a superconductor unless there is every reason to
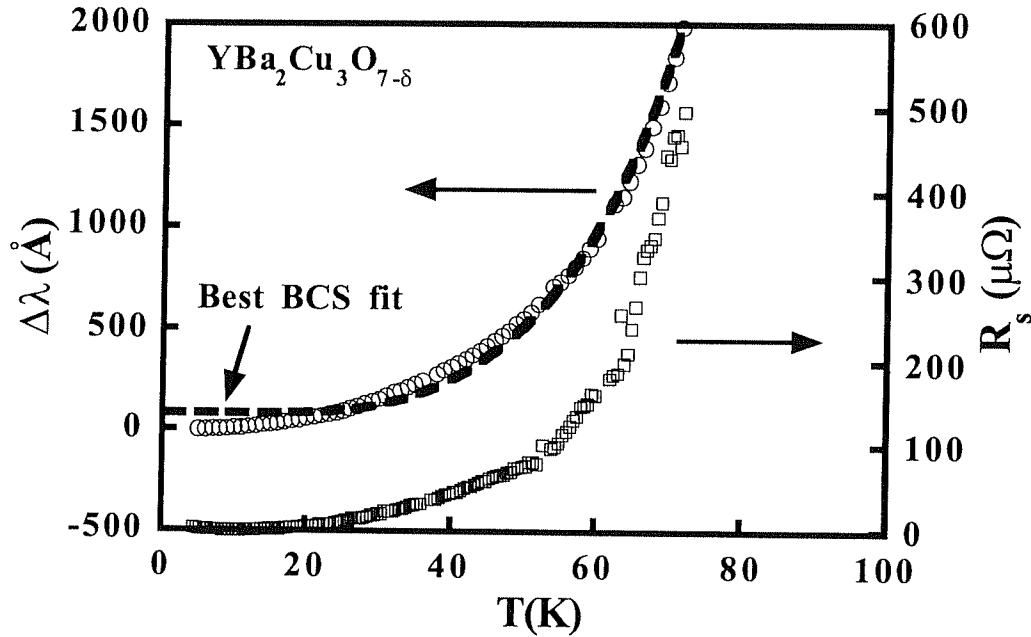
Fig. 2.10. Penetration depth and surface resistance of 3000Å-thick $YBa_2Cu_3O_{7-\delta}$ films on $LaAlO_3$ substrates. The dashed line is a fit to the temperature dependence of $\lambda(T)$ given by Mühlschlegel, which does *not* fit well. The parameters of the fit shown are $\lambda(0) = 2580$Å and $T_c = 100.1$ K.

believe that the surface region is exactly identical to the rest of the sample bulk. Surface roughness, unknown surface material, uneven doping due to oxygen loss or oxygen incorporation, fingerprints, chemical damage, and other surface defects can all be reasons why this might not be the case. Although we have shown that a proximity-coupled

metallic layer on the surface of $YBa_2Cu_3O_{7-\delta}$ cannot reasonably account for the $\lambda(T) \sim T$ behavior [101], it is nevertheless important to remember that this linear dependence is essentially a property of the surface region.

2.2.5 $GdBa_2Cu_3O_{7-\delta}$

This material is identical to $YBa_2Cu_3O_{7-\delta}$ in structure, and has the same transition temperature of $\sim$ 90K. In DC measurements, in fact, there would be no good way to tell them apart. Yet because Gd is a magnetic ion, the Gd sublattice undergoes an ordering at $\sim$ 3 K which is visible as a strong peak in electromagnetic absorption. Fig. 2.11 shows this; while normally the surface resistance would decrease monotonically as T -> 0, much of the electromagnetic energy passing through the film surface in $GdBa_2Cu_3O_{7-\delta}$ goes into disordering Gd spins which have reduced the free energy of their sublattice by ordering themselves. There is little effect on the superfluid properties, as seen in Fig. 2.12; the resonant frequency shows almost no discernible features around 3 K at all. These samples were made by S. Green at Neocera, Inc. by pulsed laser deposition, under conditions very similar to those under which the $YBa_2Cu_3O_{7-\delta}$ films were made.
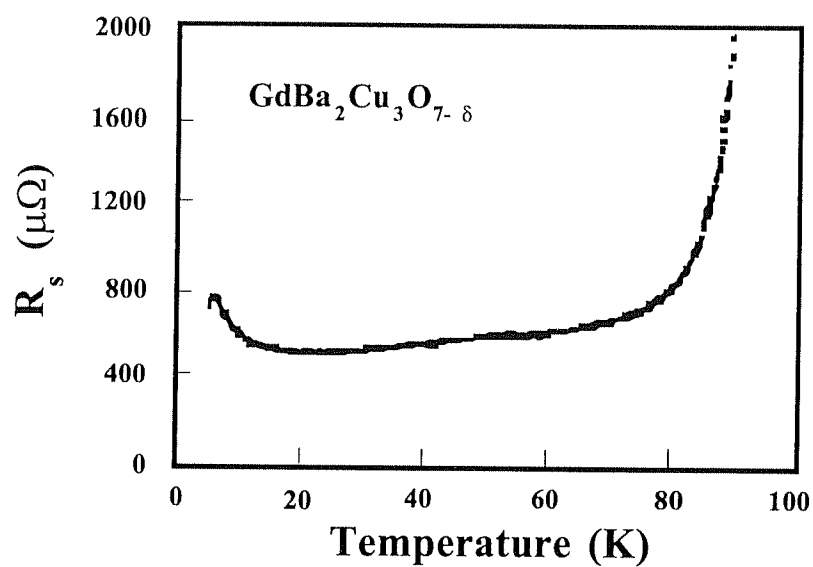
Fig. 2.11. Surface resistance of $GdBa_2Cu_3O_{7-\delta}$ films, using a 125μm Teflon spacer. Note the small peak in R_s at 3K, associated with the Gd sublattice magnetic ordering temperature.
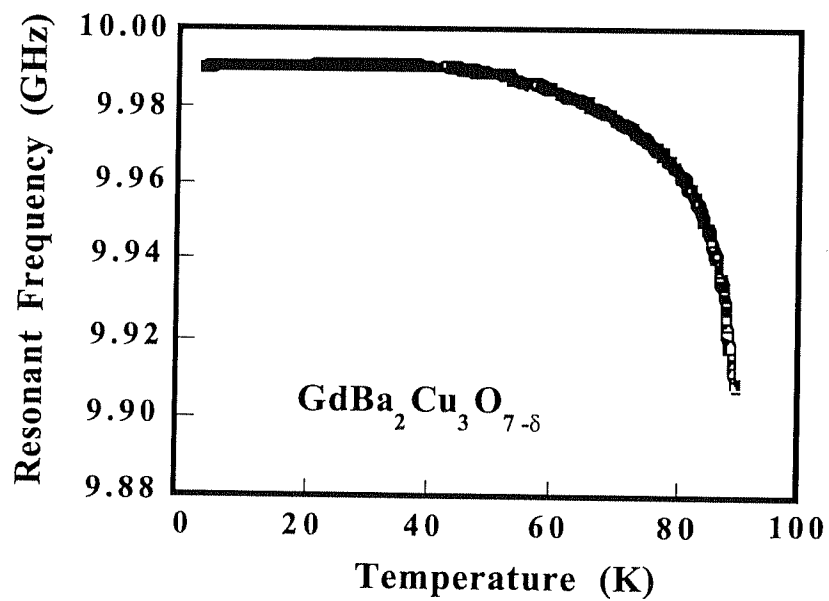
Fig. 2.12. Resonant frequency vs. temperature for $GdBa_2Cu_3O_{7-\delta}$ films, using a 125 μm Teflon spacer. The feature at 3K related to Gd magnetic ordering is hardly noticeable here.

55

Chapter 3
Surface Impedance of Conventional Low-T_c Proximity-Coupled Bilayer Films

3.0 Introduction

In contrast to the relatively well-behaved microwave properties of the single-layer superconductors shown in Ch. 2, proximity-coupled bilayers display more complex behavior due to the spatially inhomogeneous superfluid density in the proximity-superconducting normal metal and its temperature dependence. This chapter contains surface impedance data on two proximity-superconducting systems (Nb/Al and Nb/Cu), in which the normal (N) metal film is deposited on top of the superconducting (S) film. In each system, the data demonstrate that the normal metal layer behaves effectively like a superconductor, screening the applied RF magnetic field in a characteristic way. To understand this behavior, the thickness of the normal layer was varied from 0 Å (bare superconductor) to a few hundred Å. These normal metal thicknesses are much thinner than in most previous electromagnetic experiments on proximity systems, so that we are able to study the induced superconductivity in the region of the normal layer near the S/N interface.

3.1 Nb/Al Bilayers

The Nb/Al system was chosen because it has desirable properties for studying proximity effect physics; Nb is a well-characterized superconducting material, Al is a good metal which is itself a superconductor at a lower temperature $T_{cN} = 1.14$ K, and the two form clean interfaces without interdiffusing into one another [102], a requirement for optimum proximity coupling [71]. The fact that Al is itself a superconductor is

important; significant differences in behavior, such as the formation of a gap and the divergence of the decay length K^{-1} as $T \rightarrow T_{cN}$ rather than as $T \rightarrow 0$, have been postulated between proximity-coupled truly normal metals ($T_{cN} = 0$ K) and intrinsic superconductors induced into superconducting above their transition temperature [43].

3.1.1 Fabrication and Characterization of Nb/Al Bilayers

Niobium films of thickness 1 µm were first deposited on R-plane sapphire substrates by DC magnetron sputtering in 5 mTorr flowing Ar at substrate temperature $110°$ C. The chamber was evacuated to 1×10^{-7} Torr beforehand, and the Nb target presputtered to remove surface contaminants and improve oxygen gettering. Nb was deposited at a rate of 30Å/sec, and bare Nb films made this way had resistivity $\rho_n(10K) \sim 1$ µΩ-cm and resistivity ratio $\rho_n(300K)/\rho_n(10K) \sim 4$. The films were deposited by Sining Mao at Maryland.

To ensure a clean, oxide-free S/N interface, the substrate was then rotated in-situ (without breaking vacuum) and Al was deposited by RF sputtering at 12Å/sec to the desired thickness d_N, where $100\text{Å} \leq d_N \leq 600\text{Å}$. The substrate temperature while depositing Al was $\sim 100°$ C, and the total time required to rotate between sputter targets was ~ 3 sec. Resistivity measurements on Nb/Al bilayers indicated that $\rho_{Al} \geq 3\rho_{Nb}$ at 10 K, and that the same resistivity ratio $\rho_n(300K)/\rho_n(10K) \sim 4$ applied.

The Nb/Al bilayer samples produced this way exhibited transition temperatures T_c in the range 9.0 - 9.1 K, as determined by AC susceptibility measurements. These values were less than the optimum value of 9.3 K found in bulk samples, but are typical of Nb films grown at $110°$ C and are *not* lower because of the presence of Al, which would occur only with much thicker Al layers. In order to check the quality of the S/N interface, point-contact spectroscopy (PCS) measurements were performed in the manner of van Son [103] by undergraduate student Arijit Das. The dynamic resistance dV/dI fit the Blonder-Tinkham-Klapwijk [104] form with interface scattering parameter $Z < 0.2$

and attenuation factor $\Lambda_{PCS} \sim 0.5$ in Al. This indicated that the interface produced good proximity coupling, and also led to the expectation that Al would be best described by the dirty limit.

3.1.2 Magnetic Screening and Effective Penetration Depth $\Delta\lambda_{eff}(T)$

Parallel-plate resonator measurements were made using two identical samples of each Al thickness and a 25 μm-thick Teflon™ dielectric spacer. The sample dimensions (0.375" x 0.400") led to a fundamental mode frequency of ~ 11.5 GHz. As described in section 2.1.2, magnetic field penetration into the plates (now S/N bilayers instead of single-layer superconducting films) affects the resonant frequency by slowing the propagation of TEM waves. Thus by studying the dependence of the resonant frequency on temperature, one can gain information about the penetration of magnetic field into whatever material is chosen for the plates.
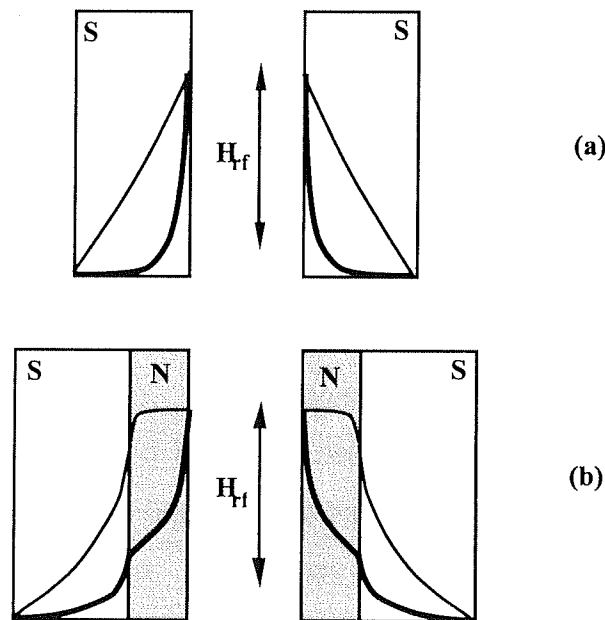
Fig. 3.1 Approximate magnetic penetration profiles inside the plates of a parallel-plate resonator for (a) homogeneous bare superconducting films and (b) proximity-coupled S/N bilayer films. The thin curves are for $T \approx T_c$, while the thick curves show the behavior for $T \ll T_c$.

$$f_o(T) = \frac{f_a}{\sqrt{1 + \frac{2\lambda}{d}}}$$

$$\left(\frac{f(T)}{f_a}\right)^{-2} = 1 + \frac{2\lambda(T)}{d}$$

$$\frac{2\lambda(T)}{d} - \frac{2\lambda(T_o)}{d} = \left(\frac{f_a}{f(T)}\right)^2 - \left(\frac{f_o}{f(T_o)}\right)^2$$

$$\lambda(T) - \lambda(T_o) = \frac{d}{2}\left[\left(\frac{f_a}{f(T)}\right)^2 - \left(\frac{f_o}{f(T_o)}\right)^2\right]$$

$$f_a^2 = \frac{f^2(T_o)}{1 + 2\frac{\lambda(T_o)}{d}}$$

$$\lambda(T) - \lambda(T_o) = \frac{d}{2}\left[\left(\frac{f(T_o)}{f(T)}\right)^2 \frac{1}{1 + \frac{2\lambda(T_o)}{d}} - \left(\frac{1}{1 + \frac{2\lambda(T_o)}{d}}\right)\right]$$

$$\lambda(T) - \lambda(T_o) = \frac{d/2}{1 + \frac{2\lambda(T_o)}{d}}\left[\left(\frac{f(T_o)}{f(T)}\right)^2 - 1\right]$$

In particular, one can hope to learn about magnetic screening done by the proximity-superconducting N metal in an S/N bilayer. Figure 3.1 shows the approximate magnetic field penetration profiles one might expect in a parallel-plate resonator composed of (a) bare superconducting films and (b) S/N bilayer films. These pictures are intended to help clarify the data presented below.

In order to compare screening behavior in a bilayer with that of a homogeneous superconductor, we transform the resonant frequency data into changes in penetration depth by means of Eq. 2.18. Rearranging that expression, we define

$$\lambda_{eff}(T) - \lambda_{eff}(T_0) = \Delta\lambda_{eff} = \frac{d}{2}\left[\left(\frac{f(T_0)}{f(T_0)}\right)^2 - 1\right] \tag{3.1}$$

where T_0 is the lowest temperature at which data was taken. We have replaced λ in (2.18) with an effective penetration depth λ_{eff} in anticipation of the fact that S/N bilayers do not have a single, well-defined value of λ, due to their spatially inhomogeneous superconducting properties. As we shall see, λ_{eff} is related to the inductance per unit length L of a superconducting transmission line by $L = (\mu_0/W)(d+2\lambda_{eff})$, where W is the film width. For systems in which the penetration profile of magnetic field is exponential (a homogeneous superconductor thicker than its penetration depth), λ_{eff} happens to equal λ, as seen in Eq. (2.16). Changes in the resonant frequency are caused by changes in inductance, however, which for inhomogeneous superconducting systems like S/N bilayers is not simply related to a single length scale. The definition given by Eq. 2.13 will be generalized to the case of S/N bilayers in Chapter 4.

Figure 3.2 shows the effective penetration depth change $\Delta\lambda_{eff}$ for Nb/Al bilayers with Al thicknesses 0Å, 100Å, 200Å, 300Å, and 600Å. The curves have been displaced vertically for clarity; only changes in λ_{eff} are meaningful here.

3.1.3 Al Layer Thickness Dependence of $\Delta\lambda_{eff}(T)$

The bare Nb sample on sapphire behaves very much in accordance with BCS theory, though because of different deposition conditions the best fit parameters were $\lambda(0) = 585\text{Å}$ and $T_c = 9.03\text{K}$, unlike the values $\lambda(0) = 353$ Å and $T_c = 9.17$ K for Nb on Si given in Fig. 2.6. Then, as successive thicknesses of Al are added, we see this BCS behavior give way to a dependence on temperature that is not well described by an exponential at low temperatures but rather by a power law of the form $\Delta\lambda_{eff}(T) \sim T^{\alpha}$,
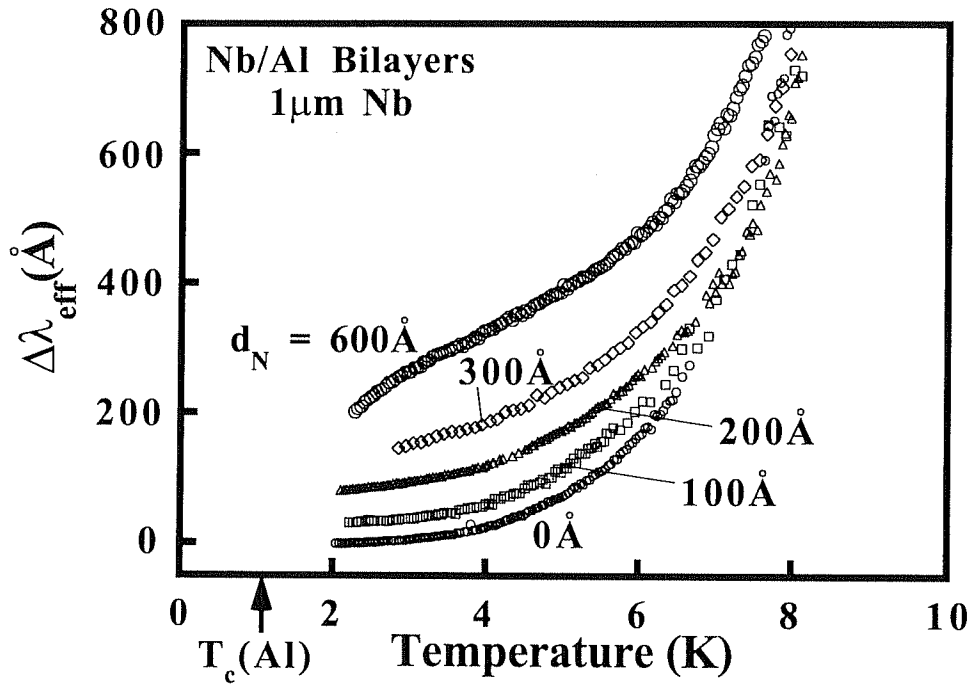
Fig. 3.2. Effective penetration depth change $\Delta\lambda_{eff}(T)$ for Nb/Al bilayers, with Nb layer thickness 1 μm and Al thickness d_N, where $100\text{Å} \leq d_N \leq 600\text{Å}$. The curves have been offset vertically for clarity; only changes in λ_{eff} are meaningful. The downturn of λ_{eff} in the 600Å sample indicates the onset of screening done by proximity-coupled Al.

with $\alpha \leq 1$. For Al thickness $d_N = 100\text{Å}$, the behavior is nearly identical to that of bare Nb; the Al is too thin to make a difference in screening properties. But for $d_N = 200\text{Å}$ and 300Å, we see a noticeably linear dependence on temperature below $0.4\ T_c$, indicating

60

that something other than simple activated depletion of the condensate is occurring. Finally, at $d_N = 600\text{Å}$, a change of curvature is evident as T decreases, signifying that the Al layer is screening the applied RF magnetic field in a strongly temperature-dependent manner. The difference between the linear behavior with T of the 200Å and 300Å samples and the sublinear dependence of the 600Å sample suggests that a characteristic length scale describing magnetic penetration in proximity-coupled Al lies between 300Å and 600Å. Such screening behavior, most active at low temperatures, has been seen in previous magnetization experiments [38,41,45,48,49]; however, not many experiments have been sensitive to it in such thin N layers. After the 300Å Al layer was stripped off, behavior obeying BCS theory was recovered in the bare Nb film.

3.1.4 Surface Resistance Dependence on Al Thickness

The surface resistance in S/N bilayers is a quantity that almost no previous work has addressed [54], yet it yields new information, available to only a few experimental techniques, and of great interest in understanding proximity-induced superconductivity. In particular, the ability of electromagnetic absorption measurements to probe the existence of coherence effects between thermally excited quasiparticles makes it a unique technique for studying these effects in a proximity-superconducting normal metal.

The surface resistance of Nb/Al bilayers is shown in Fig. 3.3 for $d_N = 0\text{Å}$, 100Å, 200Å, 300Å, and 600Å; it is in many ways similar to the $\Delta\lambda_{eff}$ data of Fig. 3.2. The bare Nb data shows a rapid drop in R_s just below T_c, followed by an exponentially slow approach to its low-temperature value of $R_s \sim 10\ \mu\Omega \pm 4\ \mu\Omega$. As thicker layers of Al are added, this behavior gives way to a second rapid decrease around 0.3 T_c, visible most clearly in the 600Å sample. Although the magnitudes of R_s shown in Fig. 3.3 do not vary monotonically with normal metal thickness due to some variations in materials parameters, the progress from exponential T-dependence at low d_N to the sublinear behavior at $d_N = 600\text{Å}$ is still very noticeable. This again points to a characteristic length

61

scale lying somewhere between 300Å and 600Å.

The similarities between the $\Delta\lambda_{eff}(T)$ and $R_s(T)$ data in Nb/Al suggest that they both may be related to the same phenomenon; a model of the electrodynamics of S/N bilayers, given in Chs. 4 and 5, show that this is the case.
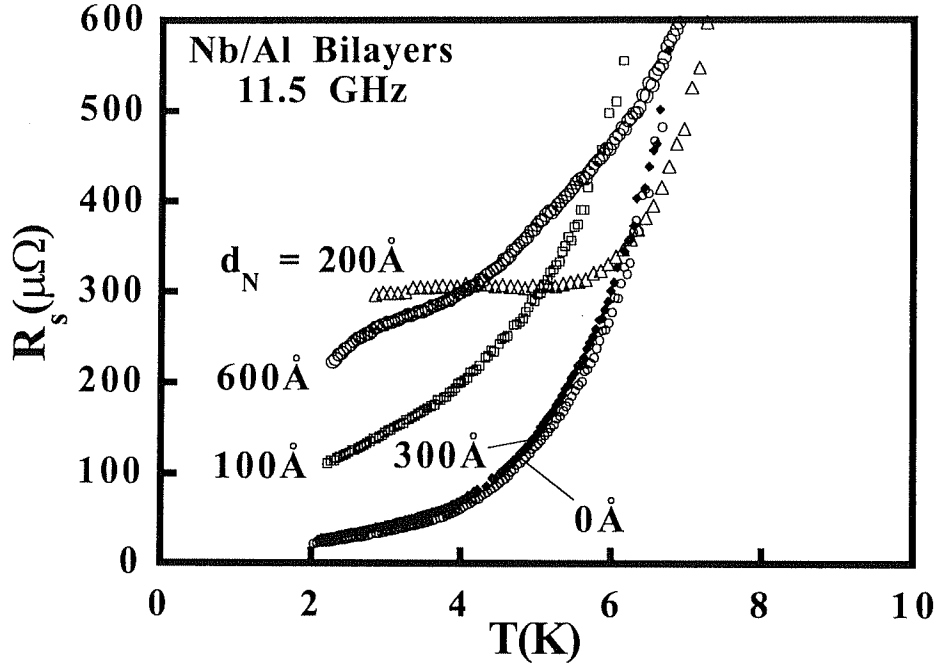
Fig. 3.3. Surface resistance data for Nb/Al bilayers with Nb layer thickness 1 μm and Al thickness d_N, where 100Å ≤ d_N ≤ 600Å. The drop in R_s of the 600Å sample at ~3K is associated with a similar feature in $\Delta\lambda_{eff}$ in Fig. 3.2, and involves the RF losses in proximity-coupled Al that is just beginning to actively screen RF magnetic field. The nonmonotonic variation of the magnitude of R_s is due to differences in materials properties between the different samples.

3.2 Nb/Cu bilayers

The Nb/Cu system is of interest for two reasons; primarily, it is a system in which the normal metal is not a superconductor at any temperature in isolation, and secondly, it is a system which has been widely studied by other methods. The ability to

compare two proximity-superconducting metals (Al and Cu) backed by the same superconductor (Nb) will prove to be of great convenience.

The Nb/Cu system has attracted experimentalists because it too has advantageous properties for studying the proximity effect. The well-understood behavior of Nb, the ideal metallic properties of Cu, and the nearly perfect immiscibility of the two at an interface contribute to this status. In previous experiments, copper samples as thick as 35 μm have excluded magnetic fields at millikelvin temperatures when in proximity-coupled contact with Nb [37-38], and strong flux exclusion at 2K has been detected in 1 μm-thick Cu backed by only 550Å Nb [45]. In addition, tunneling measurements seem to indicate a true gap in the excitation spectrum of proximity-coupled Cu [24], and the nature of coherence effects between excitations in proximity-superconducting Cu has even been investigated by NMR [62].

3.2.1 Fabrication and Characterization of Nb/Cu Bilayers

Proximity-coupled Nb/Cu bilayer films were deposited on 3" diameter Si (100) wafers by DC magnetron sputtering. They were grown using 4 mTorr flowing Ar sputter gas, after attaining a chamber base pressure of 4 x 10^{-8} Torr. Nb was deposited to 3000Å thickness first at a substrate temperature of 450° C, using 1200W power on a 3" high purity Nb target. Then the substrate was cooled in-situ and Cu was deposited at 100° C using 1000W power on a 3" high purity Cu target. The thicknesses of Cu ranged from 90Å to 760Å. Bare Nb films made this way had resistivity $\rho_n(10K)$ = 0.5 - 1.0 $\mu\Omega$-cm, with resistivity ratio $\rho_n(300K)/\rho_n(10K)$ = 6, while 2000Å-thick bare Cu films exhibited $\rho_n(10K)$ = 0.2 $\mu\Omega$-cm and $\rho_n(300K)/\rho_n(10K)$ = 10. The bilayers had superconducting transition temperatures T_c in the range 8.7 K $\leq T_c \leq$ 9.0 K, found from DC resistivity measurements. These samples were grown at Maryland by Lie Chien, a visitor from the Chinese Academy of Sciences, Beijing.

63

3.2.2 Cu Layer Thickness Dependence of $\Delta\lambda_{eff}(T)$

Parallel-plate resonator measurements at ~ 11.5 GHz were made using 12.5 μm Teflon™ dielectric spacers, for samples with Cu thicknesses d_N = 0, 90, 270, 390, and 760Å. Whereas the Al samples of section 3.1 were "dirty", these Cu samples had longer mean free paths and thus were expected to differ from Al in their proximity-superconducting behavior. These samples were also fabricated in a more controlled way, so that their microwave properties varied monotonically with Cu thickness.
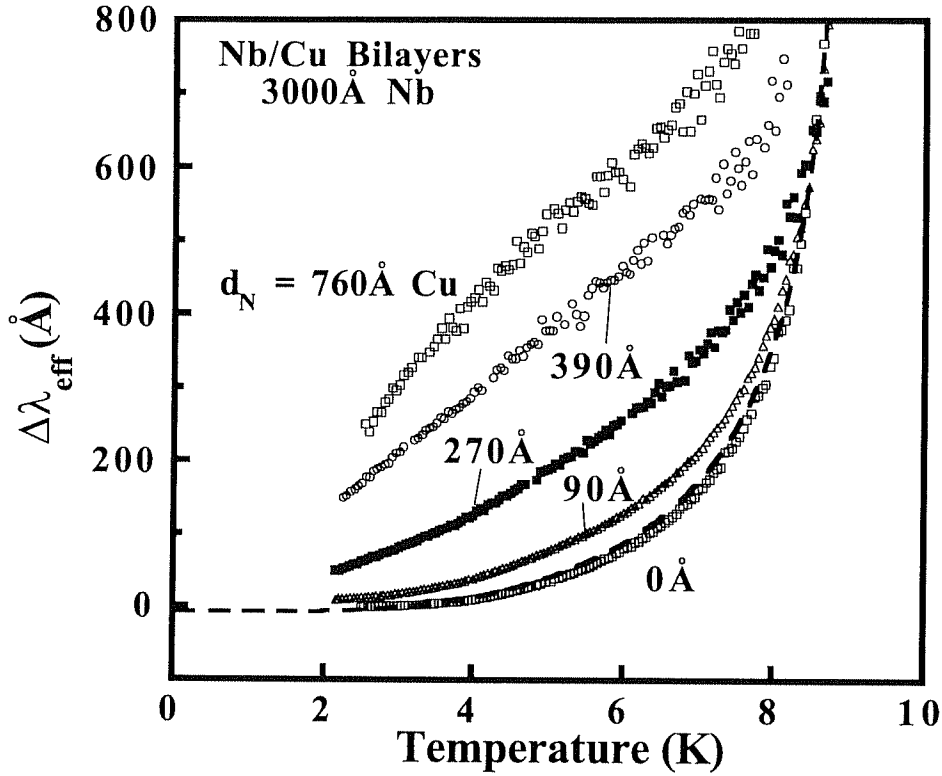
Fig. 3.4. Effective penetration depth change $\Delta\lambda_{eff}(T)$ for Nb/Cu bilayers consisting of 3000Å Nb and Cu layers of thickness d_N, where 90Å $\leq$ d_N $\leq$ 760Å. The dashed line is a fit to BCS theory [82] for the bare Nb sample. The curves have been offset vertically for clarity; no absolute values of λ_{eff} are implied.

The effective penetration depth change $\Delta\lambda_{eff}(T)$ for the Nb/Cu bilayers is shown in Fig. 3.4. Unlike the Nb/Al data given in Fig. 3.2, we see that while bare Nb fits the

64

BCS temperature dependence given by Mühlschlegel [82], Nb/Cu bilayers with Cu layers as thin as 90Å already do not. In the d_N = 90Å data, there is already a noticeably non-exponential temperature dependence at low temperature, while the 270Å and 390Å Cu samples behave linearly with temperature up to 4K and 8K, respectively. Finally, the sample with 760Å Cu shows a steeper decrease of $\Delta\lambda_{eff}$(T) and the sublinear dependence $\lambda_{eff} \sim T^\alpha$, with $\alpha \leq 1$, as T -> 2K. The characteristic change of curvature, also found in the thickest Nb/Al sample, is visible. This behavior in the 760Å Cu sample signifies that the copper layer is thick enough at d_N = 760Å to screen the RF magnetic field significantly. As with Nb/Al, the crossover from essentially Nb-like screening (0Å, 90Å, and 270Å Cu samples) to the clearly linear and sublinear T-dependence of λ_{eff} (390Å and 760Å) indicates that a characteristic length scale describing magnetic field penetration in proximity-superconducting Cu lies between 270Å and 390Å. This length scale is much smaller than any length scale in Cu found in previous magnetization measurements [36-38].

3.2.3   Surface Resistance Dependence on Cu Thickness

The surface resistances of the Nb/Cu bilayers described in section 3.2.2 are shown in Fig. 3.5. As was the case for Nb/Al, one sees a temperature dependence of R_s which is similar to that of $\Delta\lambda_{eff}$; for d_N = 0Å (bare Nb), the surface resistance approaches its limiting value exponentially slowly as T -> 0, in agreement with BCS theory. Mattis-Bardeen [59] fits on bare Nb were consistent with a Nb normal state conductivity of σ_N = 1.3659 x 10^8 Ω^{-1} m^{-1}, which agrees with the DC resistivity measured at 10 K to within experimental error. For the sample with d_N = 90Å Cu, however, this behavior was not well described by BCS theory; after dropping quickly below T_c, R_s decreases in a much more linear fashion before appearing to level off as T -> 0. In fact, as evidenced in Fig. 3.5, its surface resistance actually becomes less than that of bare Nb, reaching a low of R_s ~ 10 $\mu\Omega$ ± 4 $\mu\Omega$ at 2.1 K. At this time it is not clear whether this resulted from

superior low-loss properties of the proximity-superconducting Cu or merely from a passivation effect preventing surface oxides from forming on the underlying Nb.
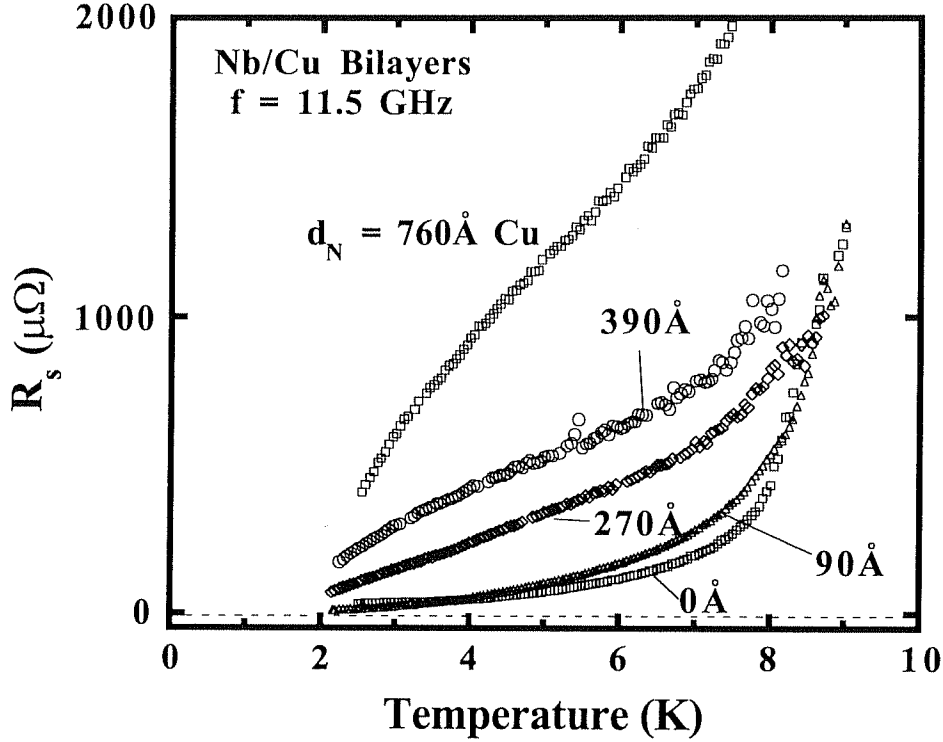
Fig. 3.5. Surface resistance of Nb/Cu bilayers with 3000Å Nb and Cu thicknesses d_N = 0Å, 90Å, 270Å, 390Å, and 760Å, at frequency 11.5 GHz. Note that the 90Å sample has a **lower** value of R_s than bare Nb at the lowest temperatures.

For the 270Å-thick sample, R_s behaved linearly with temperature all the way up to 7K, while in the 390Å and 760Å samples, a distinct change in curvature and a sublinear temperature dependence were evident, as in the $\Delta\lambda_{eff}$ data. The very rapid decrease in R_s in the 760Å sample was most noticeable; while far exceeding the R_s of the other samples at 8K, the surface resistance becomes comparable to that of the thinner samples at 2K. The Cu thickness at which the crossover from concave up to concave down occurred was 270Å; thus, as with the $\Delta\lambda_{eff}$ data, it is apparent that a characteristic screening length scale of the system lies between 270Å and 390Å. We will see in Chs. 4 and 5 that both the $\Delta\lambda_{eff}(T)$ and the $R_s(T)$ behaviors can be described by a single

66

electrodynamics model in which this characteristic screening length appears as a fitting parameter.

3.3 Comparisons Between Nb/Al and Nb/Cu Bilayers

3.3.1 Thin Normal Layer

The surface impedance data of Nb/Al and Nb/Cu are very similar, despite differences in deposition conditions, substrate, and conductivity of the normal metal layers. The general behavior of $\Delta\lambda_{eff}(T)$ in both bilayers is the same; exponentially activated temperature dependence at small normal metal thickness which gives way to a linear and then sublinear temperature dependence $\Delta\lambda_{eff}(T) \sim T^{\alpha}$, with $\alpha \leq 1$, as the normal metal thickness increases. In both bilayer systems, the thickness at which this crossover occurs is around 300Å, despite the differences in materials parameters of the two systems. The same is true for the surface resistance data; a characteristic length scale of 300Å separates essentially Nb-like behavior from essentially non-Nb-like behavior in both systems.

The reason for this is likely to be related to the thinness of the normal metal layer in both cases; while the induced order parameter far from the S/N interface depends strongly on normal metal properties, the exact behavior of the order parameter near the S/N interface may be less sensitive to these properties. This will be addressed in Chapters 4 and 5 in more detail.

3.3.2 Normal Metal Transition Temperature T_{cN}

The greatest distinction between Nb/Al and Nb/Cu is probably the fact that Al is itself a superconductor, while Cu is not (in isolation). While there are theories addressing the excitation spectrum of both types of normal metal (intrinsically superconducting versus not), there is not much difference in microwave properties other

67

than the fact that the order parameter decay length K^{-1} diverges at a finite temperature $(T_{cN} = 1.14 \text{ K})$ for Al but at $T = 0$ for Cu. In any case the data presented in this thesis does not approach either of these temperatures closely enough to discuss this. Since Al is a superconductor in isolation, it is perhaps not surprising that it may become proximity-superconducting above T_{cN}; the fact that Nb/Cu behaves the same way is, however, a significant indication that Cu is proximity-superconducting also. This is perhaps the most useful way to compare the two systems.

Chapter 4
Theory of Magnetic Field Penetration in Proximity-Coupled Systems

4.0   Overview

4.0.1 Bilayer Geometry

In order to understand the results given in Ch. 3 on proximity-coupled Nb/Cu and Nb/Al bilayers, we attempt to construct a model of proximity-effect electrodynamics. Chapter 4 addresses magnetic field penetration into proximity-superconducting bilayers as a starting point; the issue of RF losses is considered in Ch. 5.

To model the screening behavior of proximity-coupled bilayers we consider the geometry shown in Fig. 4.1. The superconducting film (S) extends from $z = 0$ to $z = d_S$, and is characterized by the quantities λ_S, ξ_S, and ℓ_S, the penetration depth, coherence length, and electron mean free path of the S material, respectively. We consider only the behavior of S below its transition temperature T_{cS}. The temperature dependences of these four quantities can be as important as those of the normal-metal (N) layer (described below) in determining the electromagnetic response of the bilayer system.

The N material may be a metal which is superconducting at a lower temperature $0 < T_{cN} < T_{cS}$ or a metal which is not superconducting in isolation at any temperature ($T_{cN} = 0$). It extends from $z = -d_N$ to $z = 0$, and is characterized by the quantities $\lambda_N(z,T)$, $K^{-1}(T)$, and ℓ_N, the induced local penetration depth, order parameter decay length, and mean free path in the N metal, respectively. We consider the behavior of the N metal at temperatures above T_{cN}, so that superconductive screening behavior can only be the result of proximity coupling to the S metal. Both layers are assumed for simplicity to extend infinitely in both the y and x directions. The interface at $z = 0$ between the two layers also affects the degree of proximity coupling, and is assumed to be sharp, i.e.,

free of oxides or insulating regions.

The pair potential $\Delta(\mathbf{r}) = V(\mathbf{r}) \langle \psi_\uparrow(\mathbf{r}) \psi_\downarrow(\mathbf{r}) \rangle$ is an appropriate order parameter with which to describe the extent of proximity coupling between the N and S layers, as explained in section 1.2.1. As indicated in Fig. 4.1, in the usual picture the order parameter is decreased from its bulk value in the vicinity of the S/N interface in the S material, and a nonzero order parameter is induced in the N metal near the S/N interface, decaying as the free surface at $z = -d_N$ is approached.
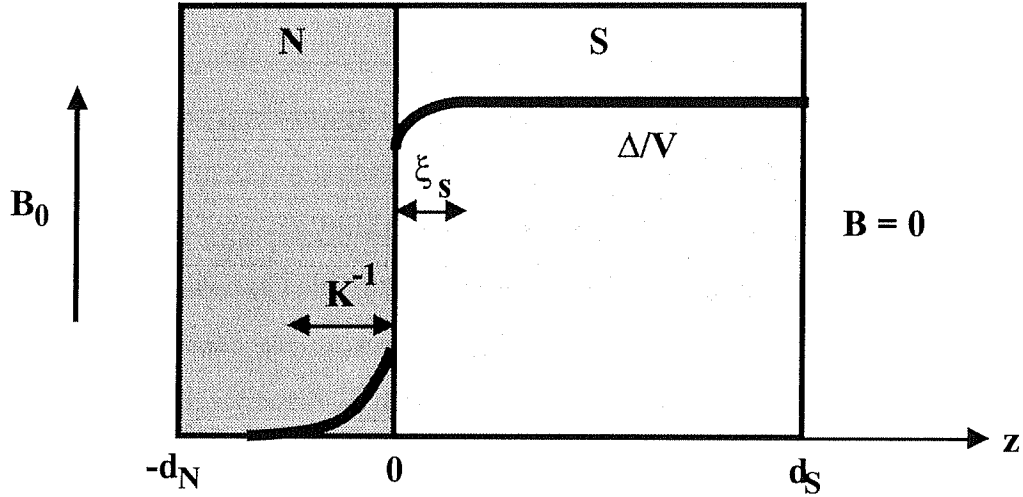
Fig. 4.1. S/N bilayer geometry, with pair amplitude $\langle \psi_\uparrow(\mathbf{r}) \psi_\downarrow(\mathbf{r}) \rangle = \Delta(z)/V(z)$ shown in N and S in the single frequency approximation.

4.0.2 Invalidity of the Single Frequency Approximation

In general, the behavior of the proximity-coupled system is determined by the behavior of the region near the interface, since far away the two materials behave as they do in isolation. If the N layer is extremely thin, the single frequency approximation described in section 1.2.3 is no longer valid, since behavior near the S/N interface may dominate the characteristics of the entire bilayer. The pairing of electrons in N is still achieved by the electronic boundary condition created by the energy gap in the excitation

spectrum of the S layer at the S/N interface (Andreév reflection), but the length scale on which the pair potential varies may be much shorter than that predicted by the single frequency approximation. In previous experiments [36-38,48-49], such rapid variation of $\Delta(r)$ near the S/N interface was not important; the samples used in those works had very thick N layers whose behavior **was** dominated by the response of the regions of the N layer far from the interface. In the samples studied in this thesis, however, such rapid variation of $\Delta(r)$ near the interface is very important. It can be detected easily in thin N films by resonant microwave experiments which are sensitive to the change in inductance caused by the additional Meissner screening occurring in the thin N layer [54,101]. This gives the work presented here its experimental value.

4.0.3 The Order Parameter in N Near the S/N Interface

The spatial dependence of the order parameter in S and N governs the distribution of Meissner screening currents and hence plays a large role in the electrodynamics of an S/N system. Because in thin N layers the higher order terms in the Gor'kov interaction kernel $K(r,r')$ cannot be neglected (see section 1.2.3), the spatial dependence of the pair potential is slightly different from that depicted in Fig. 4.1. In particular, the single frequency approximation shown there adjusts the boundary condition at the S/N interface to account for the contribution from the neglected higher-order terms in the kernel. These are replaced by a δ-function [43] at the S/N interface whose oscillator strength accounts for the higher-order Matsubara frequencies in the sum rule governing the Fourier components $K_\omega(r,r')$ of the interaction kernel. The single frequency approximation thus yields a pair amplitude $\langle \psi_\uparrow(r)\psi_\downarrow(r) \rangle = \Delta(z)/V(z)$ which is discontinuous at the S/N interface; the discontinuity approximates the rapid variation of all the higher-order terms it replaces.

In samples with thin N layers, however, this discontinuity no longer provides a reasonable approximation of the rapidly varying order parameter near the S/N interface.

The true boundary conditions (without approximation), are continuity of, and infinite slope of, the pair amplitude $\Delta/NV = \langle \psi_\uparrow(\mathbf{r})\psi_\downarrow(\mathbf{r})\rangle/N$ at the S/N interface[73]. Thus Δ/NV looks like the thin curve shown in Fig. 4.2. In fact, it was shown by Silvert and Cooper [105] that the pair amplitude is always continuous and has infinite slope at any point where the electron-electron interaction constant $V(\mathbf{r})$ changes abruptly.
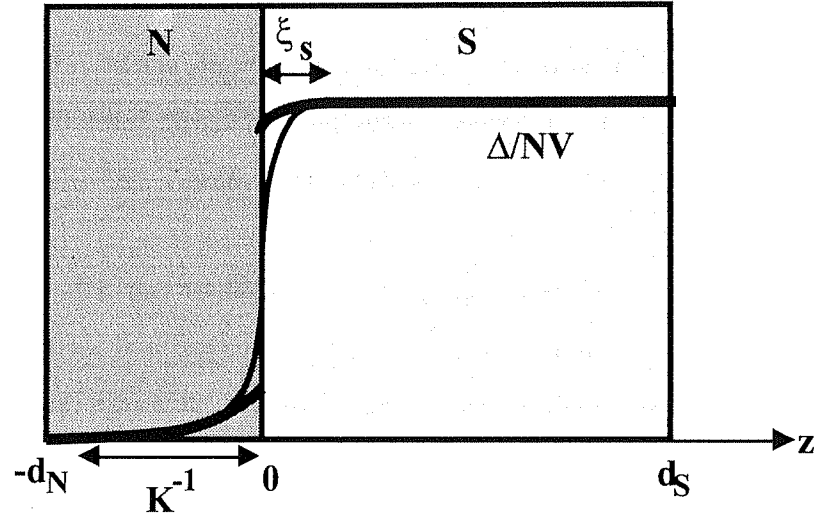
Fig. 4.2. Pair amplitude in an S/N bilayer in the single frequency approximation (thick curve) and with no approximation (thin curve).

While the distinction between the exact case and the single frequency approximation is unimportant for thick N layers, consideration of the exact case alters the profile of the pair amplitude in the case of a very thin normal layer. Since the boundary condition $d\Delta/dz = 0$ at $-d_N$ still holds, the rapid decay of the pair amplitude near the interface in N is softened, and the resulting profile looks very much like the exponential decay of the single frequency approximation, except that it occurs on a much shorter length scale, an "effective" decay length. This can be seen in Fig. 4.3. For the purposes of calculating electrodynamic properties, this "effective" exponential profile is a good enough approximation to the real situation, provided that the temperature is well above

72

T_{cN} and the induced penetration depth is larger than this effective decay length. In the remainder of this chapter, we will use an exponentially decaying function for the pair amplitude in the normal metal, keeping in mind that the effective decay lengths found in the thin normal layers presented in this thesis may be much smaller than the value of the decay length given by the one-frequency approximation for use far from the interface.
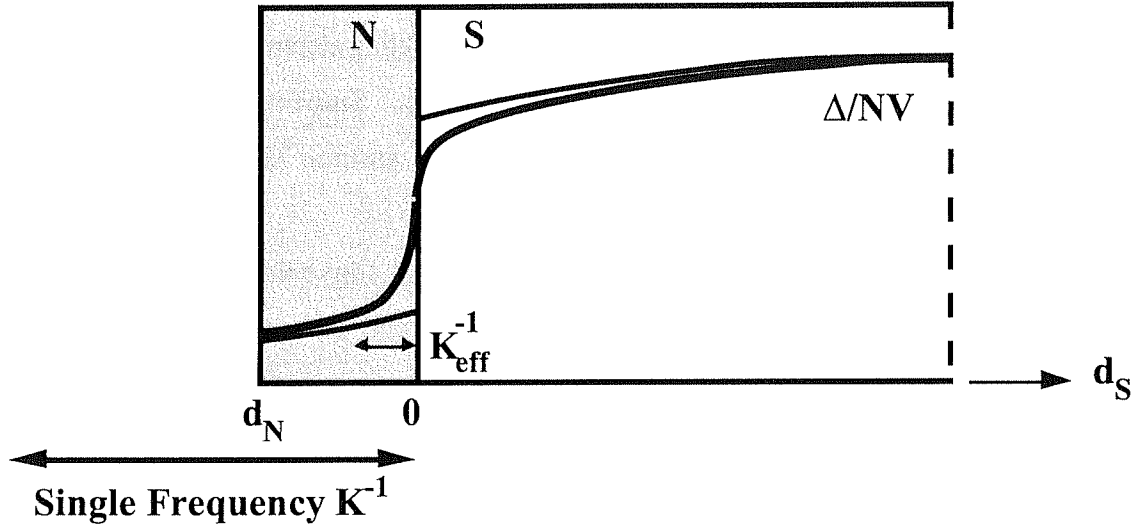
Fig. 4.3. Pair amplitude profile near the S/N interface for a normal layer thinner than the single-frequency decay length K^{-1}. In a thin normal layer, the rapid variation of the pair amplitude near the interface is more noticeable and can no longer be neglected when considering electromagnetic screening properties. Well above T_{cN} the profile can be approximated by an exponential with a much smaller effective decay length K^{-1}.

4.0.4 Spatially Dependent Penetration Depths

The penetration depth λ of a homogeneous isolated superconductor is itself a single homogeneous quantity independent of position that characterizes the superfluid response of the superconductor. It relates the vector potential $\mathbf{A}$ and the supercurrent $\mathbf{J_s}$ in a local superconductor ($\xi \ll \lambda$) according to

$$\mathbf{J_s(r)} = -\frac{\mathbf{A(r)}}{\mu_0 \lambda^2} \tag{4.1}$$

where the gauge $\nabla \cdot \mathbf{A} = 0$ has been used.

In a proximity-coupled system where the order parameter varies spatially, however, it is reasonable to expect that the superfluid response may depend on position, i.e., $\lambda = \lambda(\mathbf{r})$, and that this spatial dependence be related to that of the pair amplitude $\langle \psi_\uparrow(\mathbf{r})\psi_\downarrow(\mathbf{r})\rangle = \Delta(\mathbf{r})/V(\mathbf{r})$. Deutscher *et al.* [34] have shown that $\lambda(\mathbf{r}) \sim 1/\Delta(\mathbf{r})$ in the single frequency approximation, far from the interface, and at $\omega = 0$. Phenomenologically also, the density of "superconducting electrons" n_s is proportional to λ^{-2} via the equations describing the Meissner state. Since $n_s \sim |\langle \psi_\uparrow(\mathbf{r})\psi_\downarrow(\mathbf{r})\rangle|^2$, the square of the pair amplitude, it is reasonable to assume $\lambda(\mathbf{r}) \sim \langle \psi_\uparrow(\mathbf{r})\psi_\downarrow(\mathbf{r})\rangle^{-1} = V(\mathbf{r})/\Delta(\mathbf{r})$.

To explain experimental data, however, it is convenient to develop analytical expressions for the penetration of magnetic fields and currents, so that the problem remains as simple as possible. We therefore attempt to relax some of the constraints placed by the boundary conditions on $\Delta(\mathbf{r})$. If the N layer is not too thick, we may neglect the boundary condition $d\Delta/dz = 0$ at $z = -d_N$, obtaining a simple exponential dependence $e^{-K_{\text{eff}}(T)|z|}$. Similarly, we may neglect this boundary condition at $z = d_S$ in the S layer. We obtain the approximate spatial dependences of the penetration depths λ_N, λ_S:

$$\lambda_N(z,T) = \lambda_N(0,T)\, e^{-K_{\text{eff}}(T)z} \qquad , z < 0 \qquad (4.2a)$$

$$\lambda_S(z,T) = \lambda_\infty(T)\coth\left(\frac{z - z_0}{\sqrt{2}\,\xi_S(T)}\right) \quad , z > 0 \qquad (4.2b)$$

The latter expression is due to de Gennes [64]. Here, z_0 is given by

$$z_0 = -\frac{\xi_S}{\sqrt{2}}\ln\left[\frac{\sqrt{2}\,b}{\xi_S} + \left(\frac{2b^2}{\xi^2} + 1\right)^{1/2}\right] \qquad (4.3)$$

and b is the "extrapolation length" given by

$$b = \frac{D_S N_S}{D_N N_N} K_{eff}^{-1}(T) \coth K_{eff}(T) d_N \tag{4.4}$$

where D_S and D_N are the diffusion constants, given by $D_{S,N} = v_{FS,N} \ell_{S,N}/3$, and N_S and N_N are the densities of states at the Fermi level in S and N, respectively.

The appropriate length scale over which variations in $\Delta(z)$ occur in the S layer is the superconducting coherence length $\xi_S(T)$, according to (4.2b). Its temperature dependence is well known in BCS theory [106]. The major difference between $K_{eff}^{-1}(T)$ and $\xi_S(T)$ lies in the behaviors near T_{cN} and T_{cS}; As we shall see, $K_{eff}^{-1}(T)$ has little or no temperature dependence near T_{cS}, but diverges strongly near T_{cN}, whereas $\xi_S(T)$ is independent of T near T_{cN} and diverges near T_{cS}. This fact alone leads one to many conclusions about which layer (N or S) is most important in causing the behavior seen in proximity-coupled bilayers in sections 3.1 and 3.2.

4.1 Magnetic Field Penetration When $\lambda = \lambda(r)$

When $\lambda = \lambda(r)$, the second London equation (2.9) is altered because $\lambda(r)$ cannot be brought outside the curl as in a homogeneous superconductor.

4.1.1 Generalized London Equation and Magnetic Penetration

We apply the vector identity $\nabla \times \phi \mathbf{A} = \phi \nabla \times \mathbf{A} + \nabla\phi \times \mathbf{A}$ to (2.9), obtaining:

$$\mu_0 \lambda^2(z) \nabla \times \mathbf{J_s}(z) + \mu_0 \nabla \lambda^2(z) \times \mathbf{J_s}(z) = -\mathbf{B} \tag{4.5}$$

If we assume that $\mathbf{J_s} \approx \mathbf{J_{total}}$, we can substitute $\nabla \times \mathbf{B}/\mu_0$ for $\mathbf{J_s}$ in (4.5), obtaining

$$\lambda^2(z) \nabla \times \left(\nabla \times \mathbf{B}\right) + \nabla \lambda^2(z) \times \left(\nabla \times \mathbf{B}\right) = -\mathbf{B} \tag{4.6}$$

75

Since $\nabla \times \mathbf{B} = -\mathbf{x} \ dB/dz$ in our case, this reduces to

$$\frac{d^2B}{dz^2} + \frac{2}{\lambda(z)} \frac{d\lambda}{dz} \frac{dB}{dz} - \frac{B}{\lambda^2(z)} = 0 \tag{4.7}$$

This reduces to Eq. (2.10) as expected when $d\lambda/dz = 0$, i.e., when λ does not vary with position.

The behavior of this equation is dictated by the functional form of $\lambda(z)$. We use expressions (4.2) to describe the spatial variation of λ in a proximity-coupled bilayer system. The only assumption made is locality, i.e., that $\mathbf{J_s}$ and $\mathbf{B}$ are related at every point in space by (4.5) and (2.8).

4.1.2   Effective Penetration Depth λ_{eff} and Resonant Frequency

To calculate the effect that Eq. (4.7) has on the resonant frequency f_0, we follow the argument presented in section 2.1.2. Equation (2.13) is generally valid even when $B(z)$ is not an exponential. If we solve (4.7) for $B(z)$ and calculate the supercurrent $J_s(z)$ = $(1/\mu_0) \ dB/dz$ for a particular spatial dependence of $\lambda(z)$, we can still calculate $\mathcal{L}$, the total inductance per unit length of a parallel-plate resonator of spacer thickness d consisting of two films whose properties obey (4.7). If we define an effective penetration depth

$$\lambda_{eff} = \frac{1}{B_0^2} \int_{\substack{film \\ thickness}} B^2(z) \ dz + \frac{1}{B_0^2} \int_{\substack{film \\ thickness}} \mu_0^2 \lambda^2(z) J_s^2(z) \ dz \tag{4.8}$$

then $\mathcal{L} = \mu_0/W \ \{d + 2\lambda_{eff}\}$, where W is the width of the film. Assuming $J_s \approx J_{total} = (1/\mu_0) \ dB/dz$, the second integral in (4.8) can then be done by parts:

$$\frac{1}{B_0^2} \int \mu_0^2 \lambda^2(z) J_s^2(z) \ dz = \frac{1}{B_0^2} \int \lambda^2(z) \left(\frac{dB}{dz}\right)^2 \ dz$$

76

$$= \left[\frac{\lambda^2(z) \, B(z)}{B_0^2} \frac{dB}{dz} \right]_{z_1}^{z_2} - \frac{1}{B_0^2} \int B(z) \left[2\lambda(z)\frac{d\lambda}{dz} \frac{dB}{dz} + \lambda^2(z)\frac{d^2B}{dz^2} \right] dz$$

$$= \left[\frac{\lambda^2(z) \, B(z)}{B_0^2} \frac{dB}{dz} \right]_{z_1}^{z_2} - \frac{1}{B_0^2} \int B^2(z) \; dz \tag{4.9}$$

where the last step is a result of using Eq. (4.7). Thus the first integral in (4.8) is canceled by the second term of (4.9), leaving

$$\lambda_{eff} = \left[\frac{\lambda^2(z) \, B(z)}{B_0^2} \frac{dB}{dz} \right]_{z_1}^{z_2} \tag{4.10}$$

where z_1 and z_2 are the positions of the front and back faces of the film, respectively. In analogy with (2.18), we then write the resonant frequency as

$$f_0 = \frac{f_a}{\sqrt{1 + \frac{2}{d} \lambda_{eff}}} \tag{4.11}$$

This definition (4.11) of λ_{eff} differs from the conventional definition of $\lambda = (1/B_0)$ $\int B(z)dz$ when the decay of magnetic fields and currents is not a simple exponential; it depends on the total magnetic flux in the film **and** the manner in which it penetrates, i.e., its curvature and inflection points. The two definitions coincide for exponential penetration of field, however, in which case $\lambda_{eff} = \lambda \coth(s/\lambda)$, as seen from Eq. (2.18).

4.2 Screening Dominated by Superconducting Layer

The full spatial dependence of both $\lambda_N(z)$ and $\lambda_S(z)$ should be used to most completely describe the response of the S/N system to an applied parallel magnetic field. But it is of interest to separate out the effects induced in the two layers and consider them

separately, in order to find which effect is dominant. In many cases further simplification of the problem is then possible by neglecting the proximity-induced effects in the less dominant layer. It is advantageous computationally to do so, and may be accomplished without loss of generality if appropriate assumptions about the two layers are made.

We first consider the possibility that the magnitude of the order parameter induced in the N material is zero, but that the presence of N causes a large depression of the order parameter near the S/N interface in S. This is, for example, the expected behavior if N is a ferromagnetic material such as iron. We then expect almost no screening of field by the N film, since it is not superconducting at all and is by assumption much thinner than its skin depth, $d_N \ll \delta_N$. However, $\Delta(z)$ will be depressed to zero in the S layer at the S/N interface. If $\xi_S \approx \lambda_S$, then an appreciable thickness of the S layer will exhibit a weakened superfluid response, altering the penetration of magnetic field and current noticeably.

4.2.1 Vector Potential and Magnetic Field Solution

If the N layer is neglected, assuming that it does no screening of magnetic field at all, then the problem reduces to that of a single S layer with increased penetration depth locally near the S/N interface, according to (4.2b - 4.4). This is shown in Fig. 4.4. For this $\lambda(z)$ it turns out to be easier to solve for the vector potential $\mathbf{A}$ than to solve (4.7) for the magnetic field. Taking the curl of the relation $\nabla \times \mathbf{A} = \mathbf{B}$ and using (2.8), we find

$$- \nabla^2 \mathbf{A} - \nabla(\nabla \cdot \mathbf{A}) \approx \mu_0 \mathbf{J}_s \tag{4.12}$$

From (2.9) and the definition of $\mathbf{A}$ we can identify $\mathbf{A} = -\mu_0 \lambda^2(z) \mathbf{J}_s(z)$. If we choose the gauge so that $\nabla \cdot \mathbf{A} = 0$, combine this equation with (4.12), and insert the spatial dependence (4.2b), we obtain

$$\frac{d^2 A}{dz^2} - \frac{1}{\lambda_\infty^2} \tanh^2 \left(\frac{z - z_0}{\sqrt{2} \xi_S(T)} \right) A = 0 \tag{4.13}$$

78
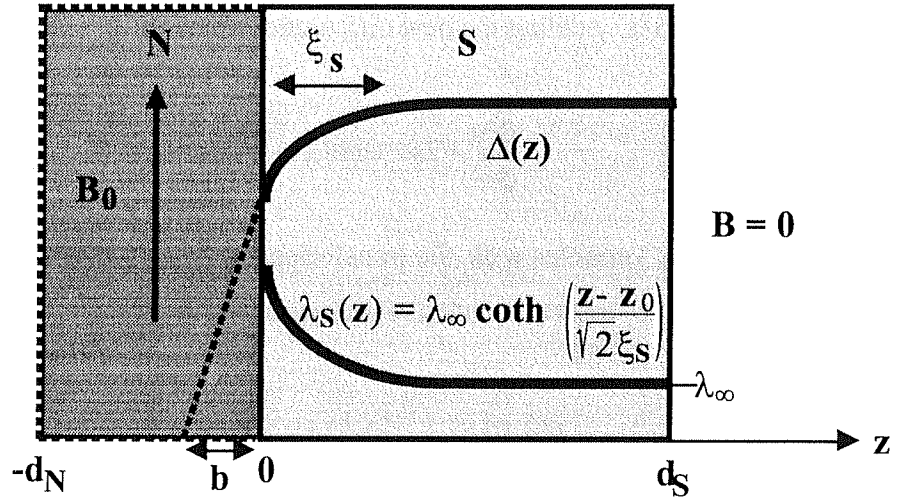
Fig. 4.4. Pair potential and position dependent $\lambda(z)$ in S layer, neglecting screening in N layer

The solution of this equation was found by de Gennes and Matricon [107], and proceeds as follows. First rewrite (4.13)

$$\frac{d^2A}{du^2} - \frac{1}{\lambda_\infty^2}\left[1 - \frac{1}{\cosh^2\alpha u}\right] A = 0 \tag{4.14}$$

where $\alpha = 1/\sqrt{2}\xi_S$ and $u = z - z_0$. Then make the change of variable $y = A\cosh^s\alpha u$, where s is a constant to be chosen conveniently below. Taking derivatives, substituting into (4.14) and canceling terms, we get

$$\frac{d^2y}{du^2} - 2s\alpha\,\tanh(\alpha u)\frac{dy}{du} + \left[s^2\alpha^2\,\tanh^2(\alpha u) - \frac{s\alpha^2}{\cosh^2(\alpha u)} - \frac{1}{\lambda_\infty^2}\left(1 - \frac{1}{\cosh^2(\alpha u)}\right)\right] y = 0 \tag{4.15}$$

We now choose s so that the term proportional to y is a constant. This yields

$$s = \frac{1}{2}\left(-1 \pm \sqrt{1 + \frac{4}{\alpha^2\lambda_\infty^2}}\right) \tag{4.16}$$

79

Either root may be used. With this choice of s the term in brackets in (4.15) takes the constant value $-\alpha^2 s$, yielding the new differential equation:

$$\frac{d^2y}{du^2} - 2s\alpha\, \tanh(\alpha u)\frac{dy}{du} - \alpha^2 sy = 0 \tag{4.17}$$

We now change variables with the transformation $p = \cosh^2\alpha u$, so that $d/du = 2\alpha(p^2 - p)^{1/2}\, d/dp$. Finally, this reduces to the differential equation:

$$p(1-p)\, y'' + \left[s(p-1) - p + \frac{1}{2} \right] y' + \frac{sy}{4} = 0 \tag{4.18}$$

where a prime indicates differentiation with respect to p. Equation (4.18) has the form of the hypergeometric equation [108] and we identify two linearly independent solutions

$$y_1(p) = p^{-a}\, {}_2F_1(a, a-c+1, a-b+1; 1/p) \tag{4.19a}$$

$$y_2(p) = p^{-b}\, {}_2F_1(b, b-c+1, b-a+1; 1/p) \tag{4.19b}$$

where $a = [-s - (s^2 + s)^{1/2}]/2$, $b = [-s + (s^2 + s)^{1/2}]/2$, $c = -s - (1/2)$, and ${}_2F_1(a,b,c;z)$ is the hypergeometric function.

The magnetic field thus has the general form $B(z) = \mathcal{A}\, B_1(z) + \mathcal{B}\, B_2(z)$, where

$$\begin{aligned} B_1 = \frac{dA_1}{dz} &= -\alpha(s+2\alpha)\, \cosh^{-(s+2a+1)}(\alpha u)\, \sinh(\alpha u)\, {}_2F_1(a, a-c+1, a-b+1; 1/\cosh^2(\alpha u)) \\ &- \frac{2\alpha a(a-c+1)}{a-b+1}\, \cosh^{-(s+2a+3)}(\alpha u)\, \sinh(\alpha u)\, {}_2F_1(a+1, a-c+2, a-b+2; 1/\cosh^2(\alpha u)) \end{aligned} \tag{4.20}$$

and B_2 is exactly the same but with a and b switched. We then solve for $\mathcal{A}$ and $\mathcal{B}$ using the boundary conditions $B = B_0$ at $z = 0$, $B = 0$ at $z = d_s$. We define a matrix M, where

80

$$M = \begin{pmatrix} B_1(d_s) & B_2(d_s) \\ B_1(0) & B_2(0) \end{pmatrix} \qquad (4.21)$$

Then $\mathcal{A} = -B_2(d_s)/\det(M)$ and $\mathcal{B} = B_1(d_s)/\det(M)$.

4.2.2 Distribution of Fields and Currents

The penetration of $B(z)$, neglecting screening in the N layer, is shown for a typical parameter set in Fig. 4.5. The RF magnetic field amplitude at the surface of the sample is 1 Gauss, and the sample being simulated consists of 3000Å Nb and 500Å Cu, with Nb parameters $\lambda(0) = 350$Å, $\xi_S(0) = 380$Å and $T_c = 9.3$K. The Cu is characterized only by its effective order parameter decay length, given by $K_{eff}^{-1}(T) = 180$Å $(4°K/T)^{1/2}$. The nature of the spatial dependence of $\lambda(z)$, given by (4.2b), causes the magnetic field $B(z)$ to always have positive curvature. In fact, as seen in Fig. 4.5, the penetration of magnetic field when the normal metal layer is neglected looks remarkably similar to the penetration profile of the bare unperturbed superconductor, despite the fact that the local penetration depth in S is as much as a factor of two larger near the S/N interface than it is deep inside S, even at modest temperatures. The current density profile for this same sample calculation is shown in Fig. 4.6; It too resembles the current profile in a bare superconducting film of Nb, except that at 8K a small change in curvature is perceptible. This effect is quite small, however, so that significant departure from pure superconducting behavior is only evident very near T_c.

4.2.3 Sample Calculations of $\Delta\lambda_{eff}(T)$

Figure 4.7 shows the expected behavior of $\Delta\lambda_{eff}(T)$ for normal layer thicknesses 800Å and 1500Å, neglecting normal layer screening. In the curves shown, the decay length in the normal layer was given by $K_{eff}^{-1}(T) = 180$Å $(4°K/T)^{1/2}$. The temperature dependence for $\Delta\lambda$ is apparently independent of normal layer thickness for $d_N > 800$Å,
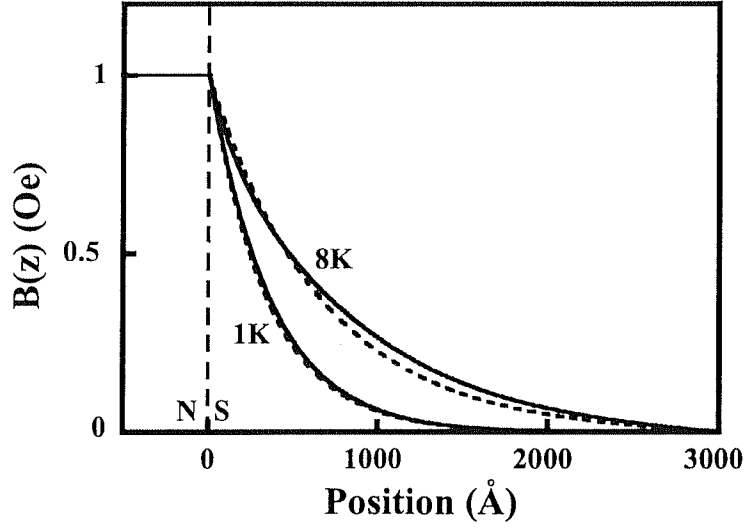
Fig. 4.5. RF magnetic field penetration into a Nb/Cu bilayer with attributes d_N = 500Å, d_S = 3000Å, $\lambda_S(0)$ = 350Å, $\xi_S(0)$ = 380Å, and $K_{eff}^{-1}(4K)$ = 180Å, neglecting the N layer entirely but considering the effect of the depression of order parameter Δ it causes near the S/N interface in the S layer. Solid lines are the model calculation, and dashed lines are the magnetic field profiles for bare Nb without the depression of Δ. The two are remarkably similar even at 8K, differing noticeably only very near T_c.
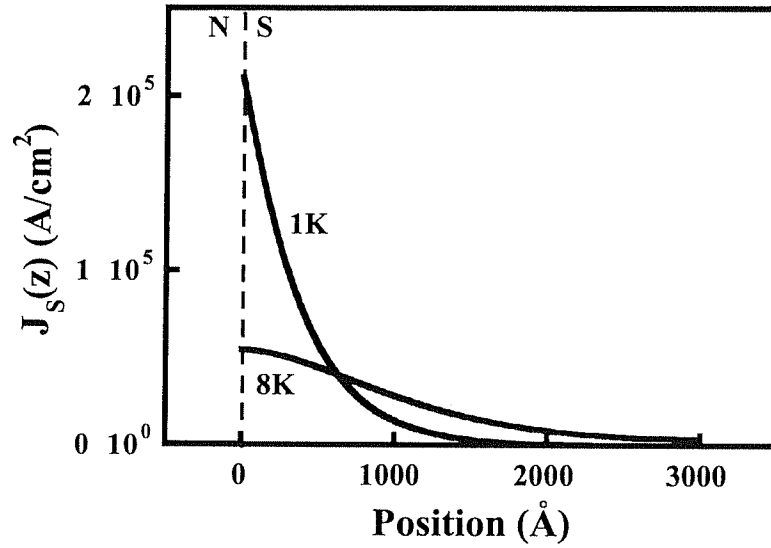
Fig. 4.6. Current density profile calculation for the sample described in Fig. 4.5, again neglecting normal layer screening. The change in curvature from pure exponential penetration of current is noticeable at 8K.
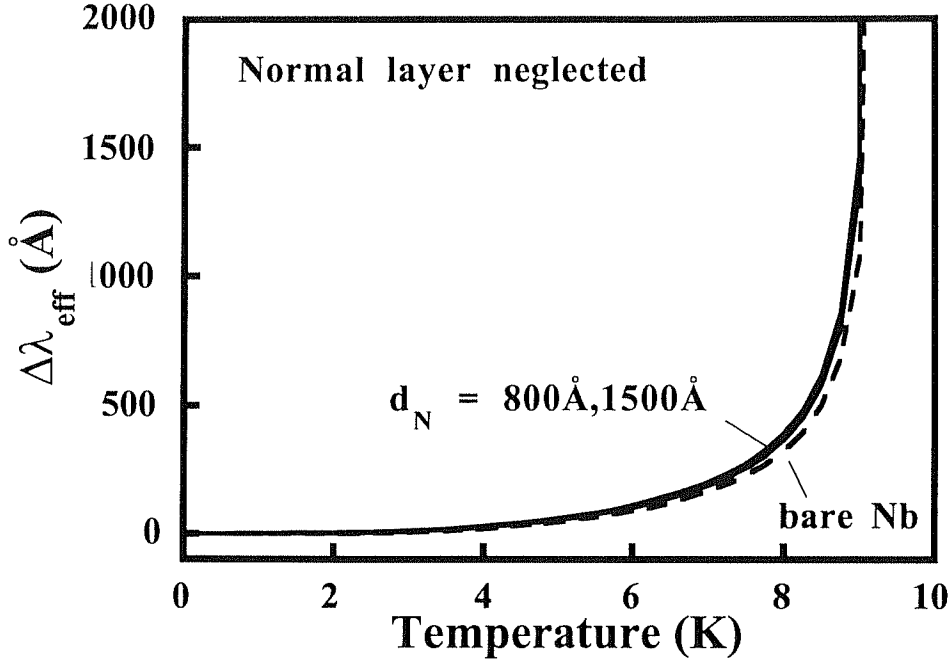
Fig. 4.7. Effective penetration depth calculation for a Nb/Cu bilayer containing 3000Å Nb, ignoring N layer screening but considering depression of Δ in S near the interface. Although the region of depressed Δ extends to a depth $\xi_S \sim 400$Å into S, the effect of this depression is not important, even with 1500Å of normal metal.

and does not ever appear to deviate much from that of a bare superconductor. Figure 4.8 shows a close-up view of the low temperature behavior. Although there is a change in the behavior of $\Delta\lambda_{eff}(T)$ from exponentially flat to linear for T < 3K, the magnitude of the change is very small, on the order of 10Å. In no way does $\Delta\lambda_{eff}(T)$ appear to drop rapidly below 2K, as is found in the actual $\Delta\lambda_{eff}(T)$ data.

The effect of varying the size of the order parameter decay length in N is shown below in Fig. 4.9 for a fixed normal layer thickness 500Å and superconducting layer thickness 3000Å. For effective decay lengths at T = 4.6K = T_c/2 which vary from 50Å to 500Å one sees only modest deviation from bare superconducting behavior, and then only near T_c. Although the calculations shown here in Figs. 4.7 - 4.9 are not a comprehensive compilation of the behaviors of all samples of interest, it is apparent that they all have one attribute in common -- the fact that at low temperature they act **more**

83
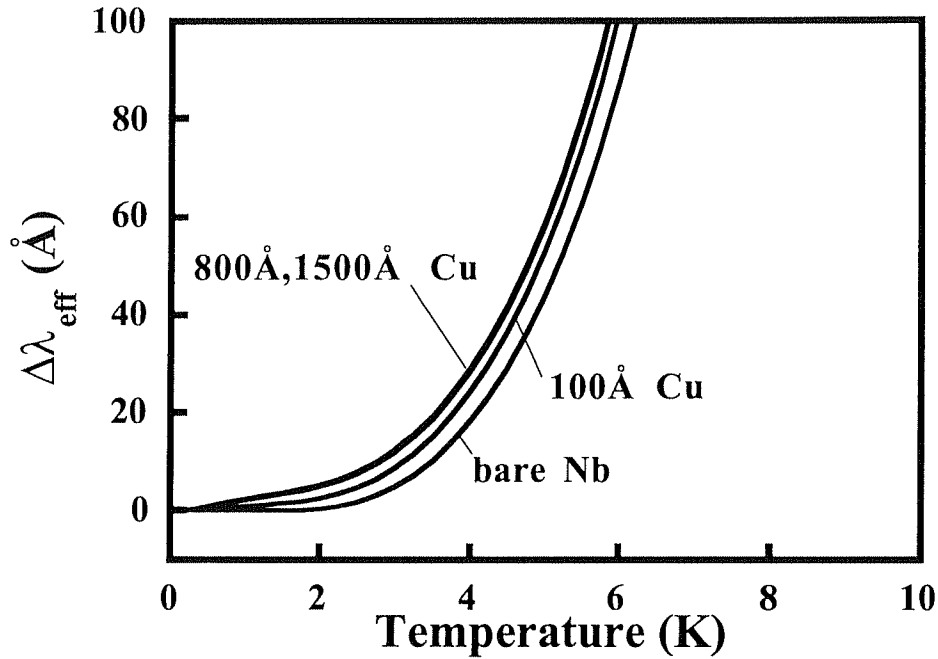
Fig. 4.8. Low-temperature behavior of the calculated effective penetration depth in a Nb/Cu bilayer containing 3000Å Nb, ignoring the normal layer, with the same parameters as used in Fig. 4.7. Note that for T < 3K the effective penetration depth depends linearly on temperature, though the deviation from the exponential behavior of bare Nb is only ~ 10Å. Also, there is no transition to downward curvature as T -> 0, as was observed in the $\Delta\lambda_{eff}$(T) data of section 3.1 and 3.2.

like a bare superconductor; the effect of the depressed order parameter is apparent only very near T_c. Since the $\Delta\lambda_{eff}$(T) data given in sections 3.1 and 3.2 all show the most marked departure from the behavior of a bare superconductor at low temperature, we conclude that **the most important physics in the problem are neglected if the screening effects of the normal layer are neglected**. We also conclude that it is not necessary to even consider the depression of the order parameter in S at all, since it has almost no effect except very near T_c. This conclusion leads to the next section, which considers the screening done by the proximity-superconducting normal layer.

84
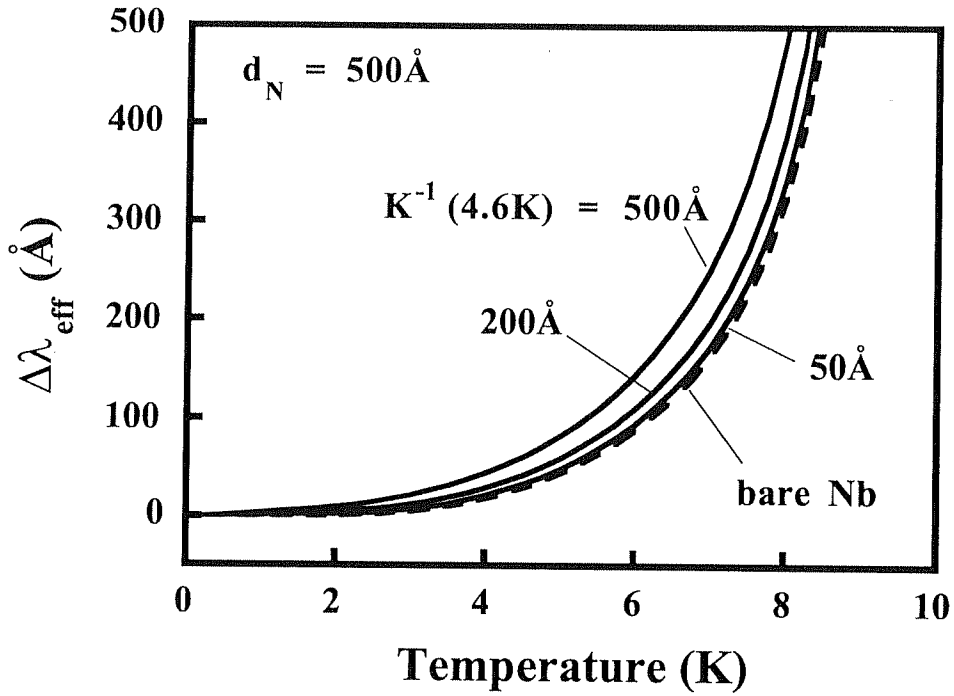
Fig. 4.9. Penetration depth calculation for fixed normal layer thickness 500Å and superconductor thickness 3000Å, varying the size of the effective order parameter decay length K_{eff}^{-1} in the N layer. Again, the behavior differs from that of a bare superconductor most strongly near T_c, but not at low temperature.

4.3 Screening Dominated by Normal Layer

In most proximity-coupled S/N systems, the effects of the N layer cannot be neglected, even when N is quite thin. If the N layer is deposited on top of the S layer, it is exposed to the full RF magnetic field, and hence must truly be entirely nonsuperconducting in order to be neglected. This is not the case, evidently, for the Nb/Al and Nb/Cu samples examined in sections 3.1 and 3.2. In this section we treat the behavior of proximity-induced screening currents in the N layer, with an eye toward reproducing the low temperature departure from homogeneous superconducting behavior seen in Nb/Cu and Nb/Al. In accordance with the results of the last section, we neglect the depression of $\Delta(z)$ entirely in the S layer.

85

4.3.1 Magnetic Field Solution with Losses Neglected

To calculate $B(z)$ inside both the normal and superconducting layers we need to solve Eq. (4.7) for the appropriate $\lambda(z)$ in N and S. Because we ignore the depression of $\Delta(z)$ in S near the S/N interface expressed in (4.2b), we assume $\lambda = \lambda_S(T)$, constant across the S layer. For $\lambda(z)$ in N we take the exponential dependence given by Eq. (4.2a), which, as pointed out in section 4.0.4, does not satisfy the true boundary condition on $\Delta(z)$ at $z = -d_N$, and which may be characterized by an effective decay length K_{eff}^{-1} much shorter than the decay length predicted by the dirty-limit single-frequency approximation.

In addition, we neglect any skin-effect screening done by the normal excitations present in the N layer. This is permissible because for the samples under study, the N layer thickness is much smaller than the skin depth δ, which is typically of order 1 μm at 10 GHz. In fact, we know that not much normal screening is occurring because it would inevitably be accompanied by large RF losses, which are not observed for our thin normal layers. The presence of normal excitations in N will, of course, contribute to the measured RF loss in the form of normal currents, but these may be treated as a first-order perturbation to the much larger Meissner screening currents and need not be considered for calculating the magnetic field profile.

If we put the dependence given by (4.2a) into (4.7), we get

$$\frac{d^2B}{dz^2} - 2K_{eff}(T)\frac{dB}{dz} - \frac{1}{\lambda_N^2(0,T)}e^{2K_{eff}(T)z}B = 0 \quad , \; z < 0 \qquad (4.22)$$

We make the change of variable

$$p(z,T) = \frac{1}{K_{eff}(T)\lambda_N(0,T)}e^{K_{eff}(T)z} \qquad (4.23)$$

obtaining

$$\frac{d^2B}{dp^2} - \frac{1}{p}\frac{dB}{dp} - B = 0 \tag{4.24}$$

Finally, we make the transformation $B = pM$, and obtain

$$p^2 \frac{d^2M}{dp^2} - p \frac{dM}{dp} - (1+p^2)M = 0 \tag{4.25}$$

This is the modified Bessel's equation of order one, with solutions $M(p) = I_1(p)$, $K_1(p)$. Hence the general solution for the magnetic field is

$$\frac{B(p)}{B_0} = \mathcal{A}\, p\, I_1(p) + \mathcal{B}\, p\, K_1(p), \quad z < 0 \tag{4.26}$$

with $p(z,T)$ given by (4.23).

In the superconducting metal S, the assumption of a homogeneous penetration depth $\lambda(z,T) = \lambda_S(T)$ yields simple exponential solutions for $z > 0$:

$$\frac{B(z)}{B_0} = \mathcal{C}\, e^{z/\lambda_S(T)} + \mathcal{D}\, e^{-z/\lambda_S(T)}, \quad z > 0 \tag{4.27}$$

We must solve for $\mathcal{A}$, $\mathcal{B}$, $\mathcal{C}$ and $\mathcal{D}$ subject to the appropriate boundary conditions. Since we treat two layers in this case, and solve for four amplitudes using four boundary conditions, this problem is more complicated than that treated in section 4.2. The appropriate boundary conditions are:

$$B(-d_N) = B_0$$

$$B(d_S) = 0$$

$$B(0) \text{ continuous}$$

$$E_{\parallel}(0) \text{ continuous}$$

\tag{4.28}

Using the first London equation $\mathbf{E} = d/dt\,(\mu_0\lambda^2\mathbf{J_s})$ and neglecting normal currents, the last of (4.28) can be expressed as

$$\lambda^2(0)\left[\frac{dB}{dz}\right]_{z=0} \text{ continuous} \tag{4.29}$$

Equation (4.29) proves convenient to use, provided the lossy currents are negligible, but it is important to note that the continuity of $\mathbf{E}$ is the actual correct boundary condition. The constants $\mathcal{A}$, $\mathcal{B}$, $\mathcal{C}$ and $\mathcal{D}$ are as follows:

$$\mathcal{A} = \frac{1}{p_1}\,\frac{\left[\dfrac{RK_0(p_0) - K_1(p_0)}{RI_0(p_0) + I_1(p_0)}\right]}{K_1(p_1) + I_1(p_1)\left[\dfrac{RK_0(p_0) - K_1(p_0)}{RI_0(p_0) + I_1(p_0)}\right]} \tag{4.30}$$

$$\mathcal{B} = \frac{1}{p_1}\,\frac{1}{\left\{K_1(p_1) + I_1(p_1)\left[\dfrac{RK_0(p_0) - K_1(p_0)}{RI_0(p_0) + I_1(p_0)}\right]\right\}} \tag{4.31}$$

$$\mathcal{C} = -\frac{p_0}{p_1}\,\frac{1}{2e^{d_s/\lambda_s}\sinh\!\left(\dfrac{d_s}{\lambda_s}\right)}\,\frac{K_1(p_0)}{K_1(p_1) + I_1(p_1)\left[\dfrac{RK_0(p_0) - K_1(p_0)}{RI_0(p_0) + I_1(p_0)}\right]}\,\frac{R\dfrac{K_0(p_0)}{K_1(p_0)} + R\dfrac{I_0(p_0)}{I_1(p_0)}}{1 + R\dfrac{I_0(p_0)}{I_1(p_0)}} \tag{4.32}$$

$$\mathcal{D} = \frac{p_0}{p_1}\,\frac{e^{d_s/\lambda_s}}{2\sinh\!\left(\dfrac{d_s}{\lambda_s}\right)}\,\frac{K_1(p_0)}{K_1(p_1) + I_1(p_1)\left[\dfrac{RK_0(p_0) - K_1(p_0)}{RI_0(p_0) + I_1(p_0)}\right]}\,\frac{R\dfrac{K_0(p_0)}{K_1(p_0)} + R\dfrac{I_0(p_0)}{I_1(p_0)}}{1 + R\dfrac{I_0(p_0)}{I_1(p_0)}} \tag{4.33}$$

where R is given by the dimensionless ratio

88

$$R(T) = \frac{\lambda_N(0,T)}{\lambda_S(T)} \tanh \frac{d_S}{\lambda_S(T)}$$
(4.34)

and $p_1 = p(-d_N,T)$, $p_0 = p(0,T)$.

4.3.2 Penetration Profiles in Various Limits

We now calculate magnetic field profiles for S/N bilayers using the full screening behavior of the N layer described in the last section. Because screening activity occurs in both layers, the behavior can be much more varied due to the many length scales involved. Some of the possible combinations of λ_S, λ_N, K_{eff}^{-1}, and d_N are either trivial or not relevant to most systems encountered in experiment; these will be discussed only briefly. The interesting cases will be explored in detail.

Electrodynamics experiments on superconductors probe properties of the sample which vary on the scale of the penetration depth λ, or in the case of the normal layer of an S/N bilayer, on some effective length scale related to $\lambda_N(z)$. As such, it is clear that N layers thinner than this effective length scale will not appear to screen the applied RF field very effectively, and these samples will behave very much like the superconductor that lies underneath the thin N layer. This is apparent in several of the curves in Fig. 3.3 and 3.4 where the N layers are too thin to produce anything more than a slight linear term in $\Delta\lambda^{eff}(T)$ at low temperature.

If the normal layer is thick enough, however, then at some temperature the effective screening length will become smaller than d_N, and the characteristic rapid decrease of $\Delta\lambda^{eff}(T)$ can be observed as $T \rightarrow 0$, as seen in the thickest normal metal layers of the samples shown in Figs. 3.2 and 3.4. So in order to observe the behavior associated with the proximity effect, namely, a divergence of the effective order parameter decay length K_{eff}^{-1}, the normal layer thickness must be comparable, roughly speaking, to the induced penetration depth $\lambda_N(0,0)$ in N. We now explore some

examples, in which we set the parameters of the S layer to be $d_S = 3000\text{Å}$, $\lambda_S(0) = 350\text{Å}$, and $T_c = 9.2\text{K}$, simulating Nb.

We can distinguish three basic types of behavior out of the various possible combinations of $K_{eff}^{-1}(T_c/2)$, $\lambda_N(0,0)$ and d_N. These are:

(a) $d_N < \lambda_N(0,0)$

Here, as explained above, the normal layer is too thin to do any screening. Consequently, the divergence of K_{eff}^{-1} at low temperature will not be apparent in an electrodynamics measurement, though such a divergence certainly occurs. The magnetic field and current density profile of such a situation is illustrated below by Figs. 4.10 and 4.11.

(b) $d_N > \lambda_N(0,0) > K_{eff}^{-1}(T_c/2)$

In this situation, the normal layer is thick enough to screen the magnetic field. But since K_{eff}^{-1} is quite small at moderate temperatures, not much of the N layer possesses the ability to screen magnetic field, so Meissner currents flow only in a sheath of thickness $\sim K_{eff}^{-1}$ near the S/N interface in the N layer. As $T \rightarrow 0$, K_{eff}^{-1} diverges and the onset of Meissner screening across the entire N layer appears to occur suddenly. In such a sample, the bilayer will appear to undergo a second superconducting transition at the temperature where $K_{eff}^{-1} \sim d_N$. The magnetic field and current profiles for such a sample appear in Figs. 4.12 and 4.13.

(c) $d_N, K_{eff}^{-1}(T_c/2) > \lambda_N(0,0)$

In this situation, the normal layer is thick enough to screen magnetic field appreciably, and the penetration length of order parameter, K_{eff}^{-1}, is large enough so that Meissner screening currents flow across most of the normal layer, even at moderately high temperatures. As the decay length K_{eff}^{-1} diverges with decreasing temperature now, the transition to the regime where N screens the applied field is not so sudden, since it is already doing so partially at higher temperatures. Thus, this sample will not appear to have a sharp second superconducting transition, but will appear to undergo a more
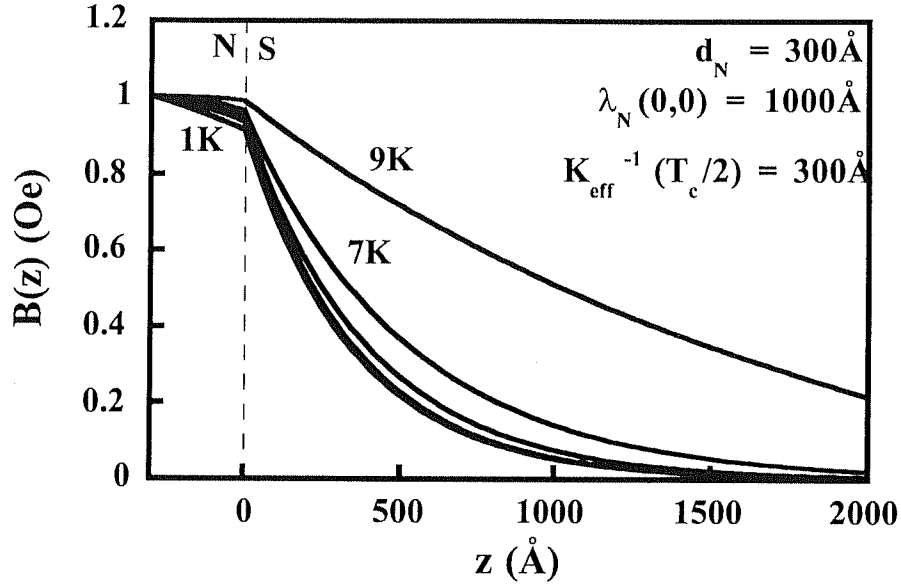
Fig. 4.10. Magnetic field profile for a bilayer with $d_N = 300\text{Å}$, $\lambda_N(0,0) = 1000\text{Å}$, and $K_{eff}^{-1}(4.6K) = 300\text{Å}$. Here, the N layer is thinner than $\lambda_N(0,0)$, so screening currents are ineffective in N and the divergence of $K_{eff}^{-1}(T)$ is not very apparent, though it is clearly occurring.
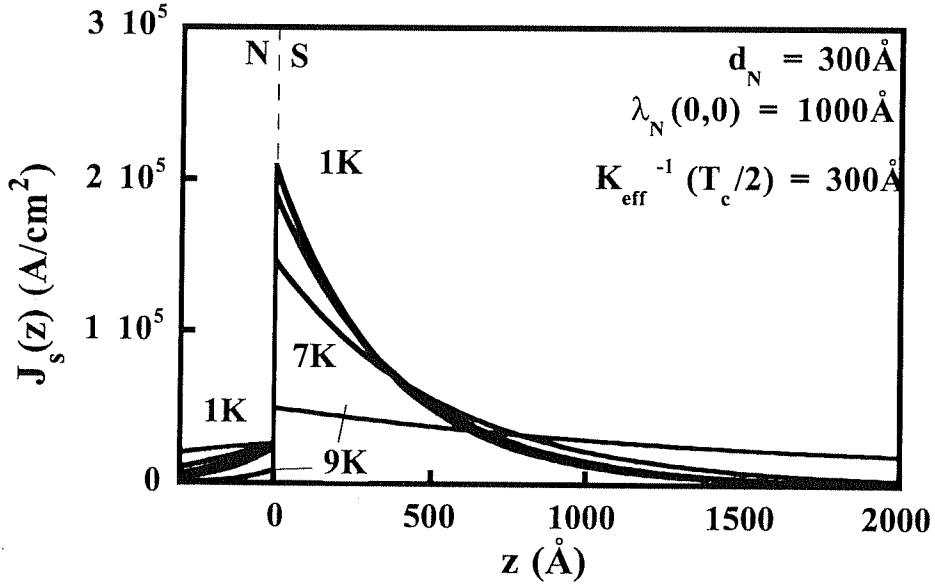
Fig. 4.11. Current density profile for the bilayer shown in Fig. 4.10. Because the N layer is too thin to screen field effectively, most of the screening current flows in the S layer. This sample will behave much like the underlying superconductor in its screening properties.

91
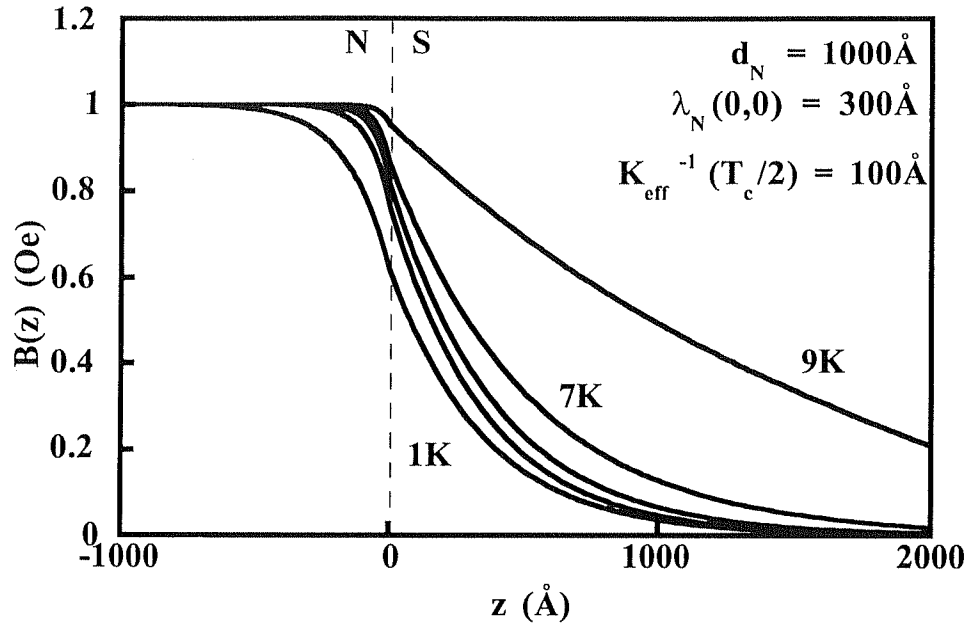
Fig. 4.12. Magnetic penetration profile for $d_N = 1000\text{Å}$, $\lambda_N(0,0) = 300\text{Å}$, and $K_{eff}^{-1}(4.6K) = 100\text{Å}$, assuming $K_{eff}^{-1} \sim T^{-1/2}$. Temperatures shown are 1K, 3K, 5K, 7K, and 9K.
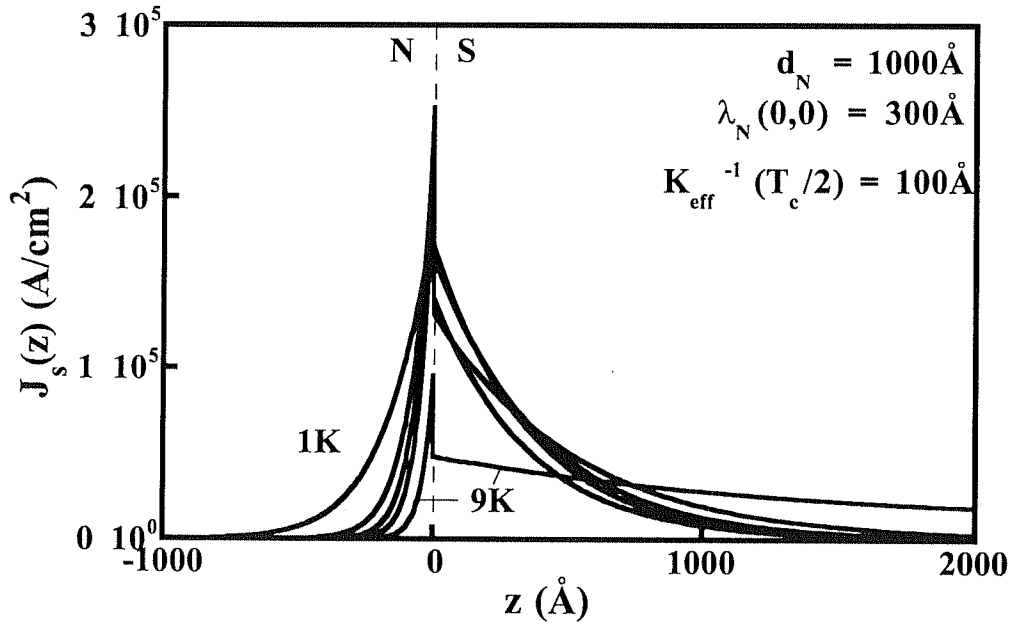
Fig. 4.13. Current density profile for the parameter set described in Fig. 4.12. The distribution of current shifts from being primarily located in N at 1K to primarily located in S at 9K.
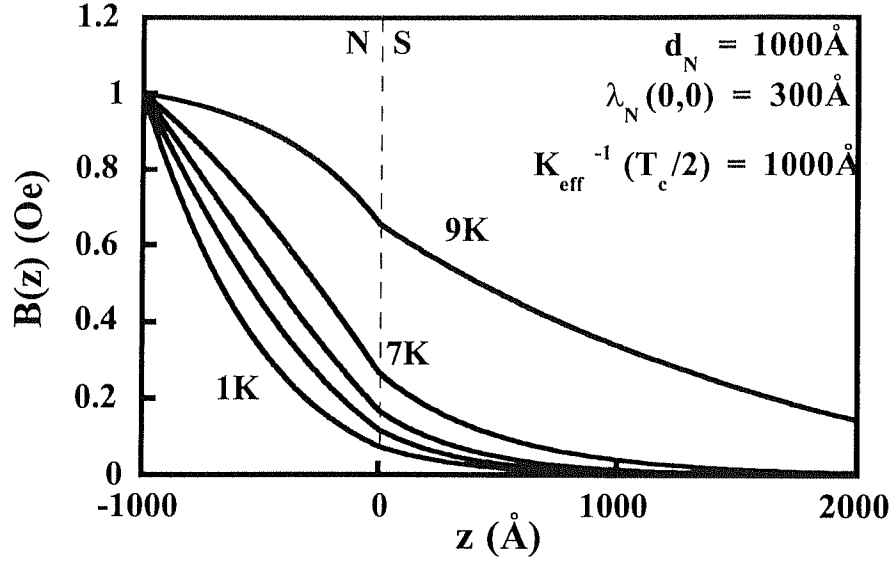
Fig. 4.14. Magnetic field profile for a bilayer with $d_N = 1000\text{Å}$, $\lambda_N(0,0) = 300\text{Å}$ and $K_{eff}^{-1}(4.6K) = 1000\text{Å}$. Since the induced order parameter extends deeper into N here, screening in N reminiscent of a homogeneous superconductor can be seen at low temperature. This behavior then gives way to the opposite screening curvature at high temperature, as in Fig. 4.10.
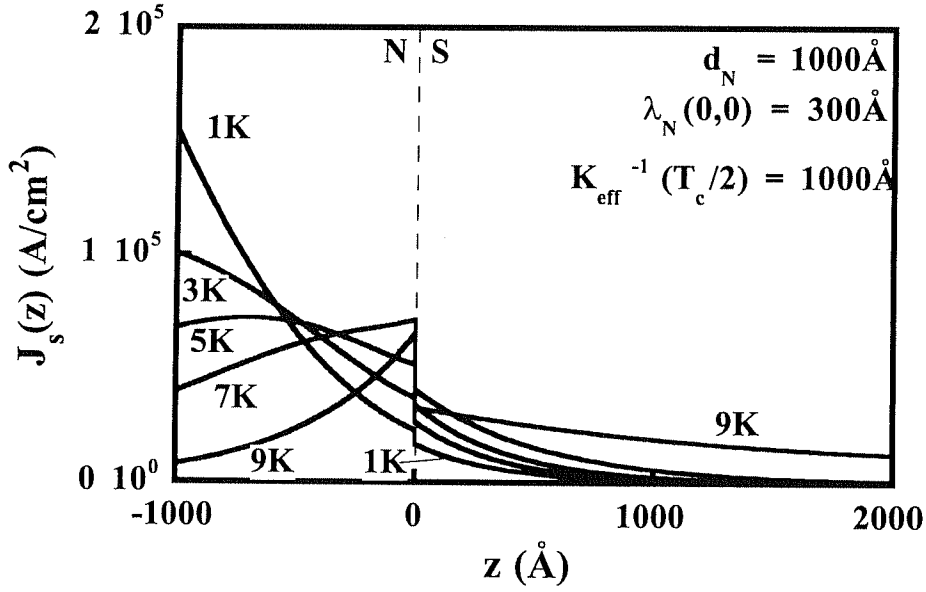
Fig. 4.15. Current density profile for the bilayer of Fig. 4.12. The shift in the location of screening currents from near the free surface at 1K to near the interface at 9K is especially evident, and has important implications for $\Delta\lambda_{eff}(T)$.

gradual shift from screening done primarily in S to primarily in N. Also, the N layer will essentially be screening the applied field as a superconductor would, even at relatively high temperatures. This can be seen in the magnetic field and current density profiles given in Figs. 4.14 and 4.15.

These three cases represent the range of screening behavior found in most bilayer samples suitable for microwave resonant experiments; they all are predicated on the existence of a thick superconducting backing layer which is thicker than its penetration depth, and whose penetration depth is comparable or smaller than the induced penetration depth in the N layer. Samples with thin S layers are important in other experiments, such as the one used by Claassen *et al.* [45], in which the vector potential needs to be constant across the bilayer; in a parallel-plate resonator measurement, however, such a sample would be forced to screen the applied RF field in a shorter distance than it would in a bulk sample, driving enormous currents and causing huge RF loss. It would not resonate, plainly stated. For reasons of inapplicability, then, such bilayer samples and their screening properties are not discussed here.

4.3.3 Calculations of $\Delta\lambda_{eff}(T)$ Including Normal Layer Screening

The magnetic field penetration and current density profiles shown in the last section both contribute to the behavior of $\Delta\lambda_{eff}(T)$, according to Eq. (4.8). In particular, when large currents flow near the S/N interface the effective penetration depth in Eq. (4.8) may be quite large. When the temperature decreases and the decay length K_{eff}^{-1} becomes comparable to d_N, these currents become distributed over a larger region of the N layer, decreasing the effective penetration depth. As we shall see, this effect is responsible for the change in curvature and rapid decrease of $\Delta\lambda_{eff}(T)$ observed in Nb/Al and Nb/Cu at low temperature. This effect is most noticeable in the samples with largest d_N, in accordance with the results of section 4.3.2.

The calculated behavior of $\Delta\lambda_{eff}(T)$ is shown in Fig. 4.16 for the three cases
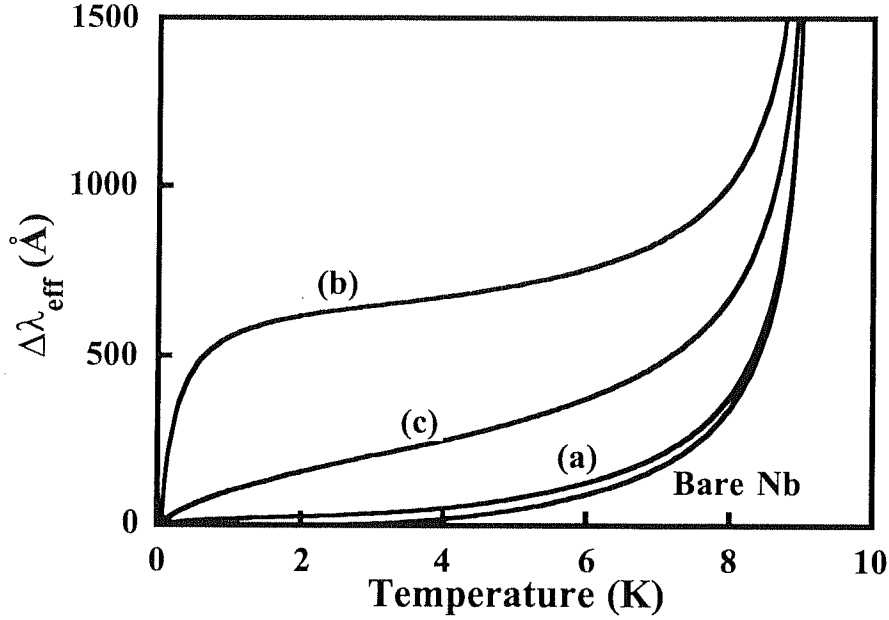
Fig. 4.16. Calculated change in effective penetration depth vs. temperature for the three types of S/N bilayer, as described above. Parameters are: (a) d_N=300Å, $\lambda_N(0,0)$=1000Å, $K_{eff}^{-1}(T_c/2)$=300Å; (b) d_N=1000Å, $\lambda_N(0,0)$=300Å, $K_{eff}^{-1}(T_c/2)$=100Å; (c) d_N=1000Å, $\lambda_N(0,0)$=300Å, $K_{eff}^{-1}(T_c/2)$=1000Å. Note that (b) has the most noticeable low-temperature behavior, showing a large decrease at T ~ 1K, where K_{eff}^{-1} ~ d_N.

examined in Figs. 4.10 - 4.15. The behavior is in agreement with the descriptions given above. Curve (a) gives the temperature dependence of $\Delta\lambda_{eff}(T)$ for a sample with a normal layer too thin to screen much magnetic field. Except for the slight linear dependence of $\Delta\lambda_{eff}(T)$ at very low temperature, curve (a) resembles the behavior of a bare superconductor very much. Curve (c), which has a thicker normal layer, displays more temperature dependence at low temperature. Yet because that sample also has a relatively large order parameter decay length, much of the N layer is already exhibiting Meissner screening even at moderately high temperatures. It does not show a spectacular rapid drop at low temperature, since the diverging quantity, K_{eff}^{-1}, is already much larger than d_N. Curve (b) represents the set of parameters which yields the most noticeable departure from the behavior of a bare superconducting film; one sees what appears to be

95
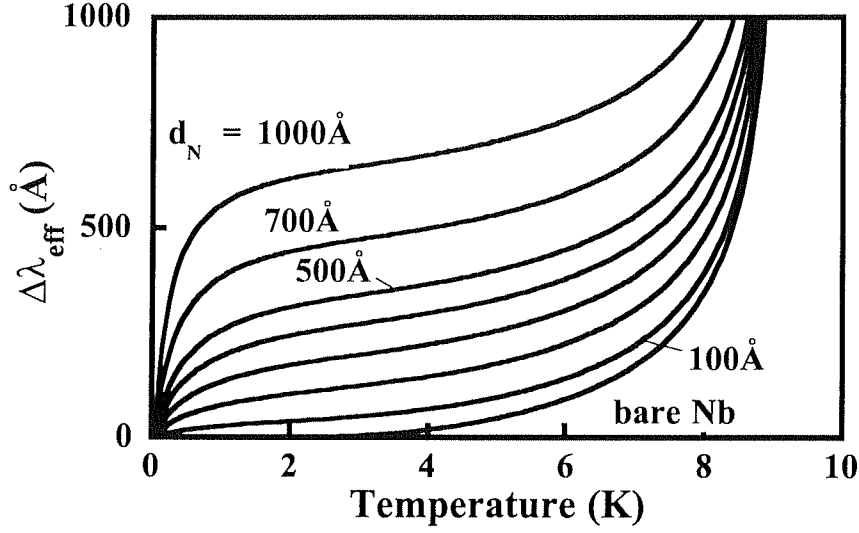
Fig. 4.17. Calculated dependence of $\Delta\lambda_{eff}(T)$ on normal layer thickness for bilayers with $d_S = 3000\text{Å}$, $\lambda_S(0) = 350\text{Å}$, $K_{eff}^{-1}(T_c/2) = 100\text{Å}$, and $\lambda_N(0,0) = 300\text{Å}$. Normal layer thicknesses shown are $d_N = 0\text{Å}$, 100Å, 200Å, 300Å, 400Å, 500Å, 700Å, and 1000Å. The N layer is assumed to be a nonsuperconducting metal in isolation.

a second superconducting transition around 1K, corresponding to the normal layer rapidly becoming essentially superconducting as K_{eff}^{-1} becomes comparable to d_N.

In order to gain a deeper perspective on the behavior of the $\Delta\lambda_{eff}(T)$ data on Nb/Al and Nb/Cu, shown in section 3.1 and 3.2, we now explore the temperature dependence of $\Delta\lambda_{eff}(T)$ as a function of normal layer thickness. Fig. 4.17 shows $\Delta\lambda_{eff}(T)$ for seven normal metal thicknesses, using the fixed parameters $d_S = 3000\text{Å}$, $\lambda_S(0) = 350\text{Å}$, $\lambda_N(0,0) = 300\text{Å}$, and $K_{eff}^{-1}(T_c/2) = 100$. While thin normal layers ($d_N < 300\text{Å}$) do not show much low temperature behavior except for a small linear term, thicker normal layers ($d_N > 300\text{Å}$) show a marked drop in $\Delta\lambda_{eff}$ occurring around the temperature where $K_{eff}^{-1} \sim d_N$. The two length scales characterizing the normal layer can thus be obtained, at least roughly; $\lambda_N(0,0)$ is given approximately by the normal layer thickness above which a significant rapid drop in $\Delta\lambda_{eff}(T)$ at low temperature is

observed, and $K_{eff}^{-1}(T)$ can be mapped out by examining the temperature at which that drop occurs for each value of d_N. Although we have assumed temperature dependences for $K_{eff}^{-1}(T)$ and $\lambda_N(0,T)$, the exact dependences are not really needed; all one needs to know is that K_{eff}^{-1} diverges as $T \rightarrow 0$ and $\lambda_N(0,T)$ becomes constant at low temperature. The utility of this method depends on the sample being studied, of course, since the parameters describing the bilayer must satisfy $d_N > \lambda_N(0,0)$, $K_{eff}^{-1}(T_c/2)$. But the ability to ascertain these length scales even approximately, without having to assume exact temperature dependences for $K_{eff}^{-1}(T)$ and $\lambda_N(0,T)$, gives the technique its experimental value.

4.4 Model Fits to Bilayer $\Delta\lambda_{eff}(T)$ Data

We now compare the model, including screening done in the normal layer, with actual data on Nb/Al and Nb/Cu bilayers presented in Ch. 3. We hope to extract parameter values for the normal layer by fitting to the model.

4.4.1 Nb/Al

The data of Fig. 3.2, with fits to the electrodynamics model added in, appears in Fig. 4.18, using a decay length temperature dependence $K_{eff}^{-1}(T) \sim T^{-1/2}$. The fit curves reproduced the $\Delta\lambda_{eff}$ data quite convincingly, particularly for the samples with 300Å and 600Å Al layers. The parameter values describing each fit are given below in Table 4.1. The values of $\lambda_N(0,0)$ and $K_{eff}^{-1}(T_c/2)$ for the 300Å and 600Å samples are quite similar, giving a level of confidence to those values. For the thinner normal layers ($d_N = 100$Å, 200Å), the values of these parameters are not in agreement. However, if $d_N < \lambda_N(0,0)$ holds for these samples, as it seems to in light of the values of $\lambda_N(0,0) \approx 360$Å found in the thicker normal layer samples, then these parameter values must be given large error bars. The parameters derived by this fitting procedure agree with the general guidelines
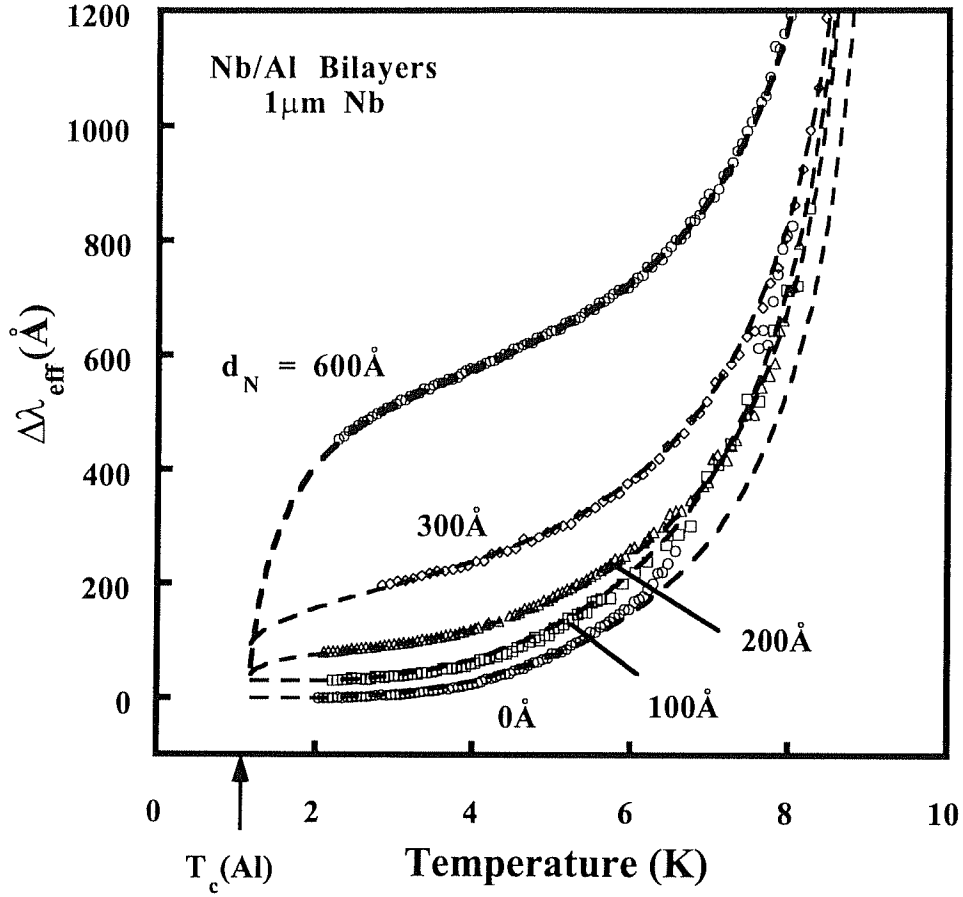
Fig. 4.18. $\Delta\lambda_{eff}(T)$ for Nb/Al bilayers, with curves fit to the model described in sections 4.3. The curves are all displaced vertically for clarity; only the change $\Delta\lambda_{eff}$ has meaning. The order parameter decay length obeys the dependence $K_{eff}^{-1}(T) \sim T^{-1/2}$.

Table 4.1. Normal metal layer thicknesses and fitting parameters for $\Delta\lambda_{eff}(T)$ data on Nb/Al bilayers. The results of a BCS fit to single-layer Nb ($d_N = 0$) data obtained by removing the Al from the 300Å Al bilayer sample are also given.

d_N (Å)	$\lambda_N(0,0)$ (Å)	K_{eff}^{-1}(4.6K) (Å)	$\lambda_S(0)$ (Å)	T_c (K)
0	----	-----	585 ± 15	$9.0 \pm .05$
100	792 ± 120	1342 ± 150	700 ± 20	$9.2 \pm .05$
200	1390 ± 230	218 ± 25	600 ± 20	$9.3 \pm .05$
300	380 ± 10	122 ± 7	600 ± 20	$9.2 \pm .05$
600	361 ± 10	130 ± 6	560 ± 20	$9.2 \pm .05$

given in section 4.3.3; samples with $d_N < \lambda_N(0,0) \approx 360\text{Å}$ show only a small linear temperature dependence at low temperature, while samples with $d_N > 360\text{Å}$ show a large decrease in $\Delta\lambda_{eff}$ at low temperature. The temperature at which this decrease occurs is roughly where $K^{-1} \sim d_N$, which for $d_N = 600\text{Å}$ samples is around 2K, in agreement with Fig. 4.18. Thus the model, inasmuch as the approximation of exponential magnetic field penetration applies, reproduces $\Delta\lambda_{eff}(T)$ data on Nb/Al bilayers very well. The error bars quoted in Table 4.1 reflect the range over which the goodness of fit is within 5% of its maximum value.

4.4.2   Nb/Cu

The behavior of $\Delta\lambda_{eff}(T)$ in the Nb/Cu samples discussed in section 3.2 is very similar to that of Nb/Al, as remarked in section 3.3. However, it was found that the dirty limit temperature dependence $K_{eff}^{-1}(T) = (\hbar D/2\pi k_B T)^{1/2}$ does not describe the $\Delta\lambda_{eff}(T)$ data very well. When the corresponding clean-limit temperature dependence $K_{eff}^{-1}(T) \sim T^{-1}$ was tried, it was found to fit only the Nb/Cu sample with $d_N = 760\text{Å}$. In addition, the fit required a local penetration depth in Cu of $\lambda_N(0,0) = 110\text{Å}$ and a decay length $K_{eff}^{-1}(T_c/2) = 78\text{Å}$, both of which are much too small given the guidelines of section 4.3.3.

The temperature dependence of $K_{eff}^{-1}(T)$ which did ultimately work turned out to be $K_{eff}^{-1}(T) \sim T^{-2}$. This temperature dependence is not predicted in the single frequency approximation under any circumstances, but has been observed previously in magnetization [41] and AC susceptibility [47] experiments on other low-T_c systems. It is related to activity of shorter decay length scales associated with the higher-order terms of the interaction kernel $K(\mathbf{r}, \mathbf{r'})$, which are relevant in such thin normal layers but are not treated by the single-frequency approximation. The $\Delta\lambda_{eff}(T)$ data of Fig. 3.4 is reproduced in Fig. 4.19 with fits to the electrodynamics model, this time using the decay length dependence $K_{eff}^{-1}(T) \sim T^{-2}$. The appropriate parameters describing the fits are given in Table 4.2.

99
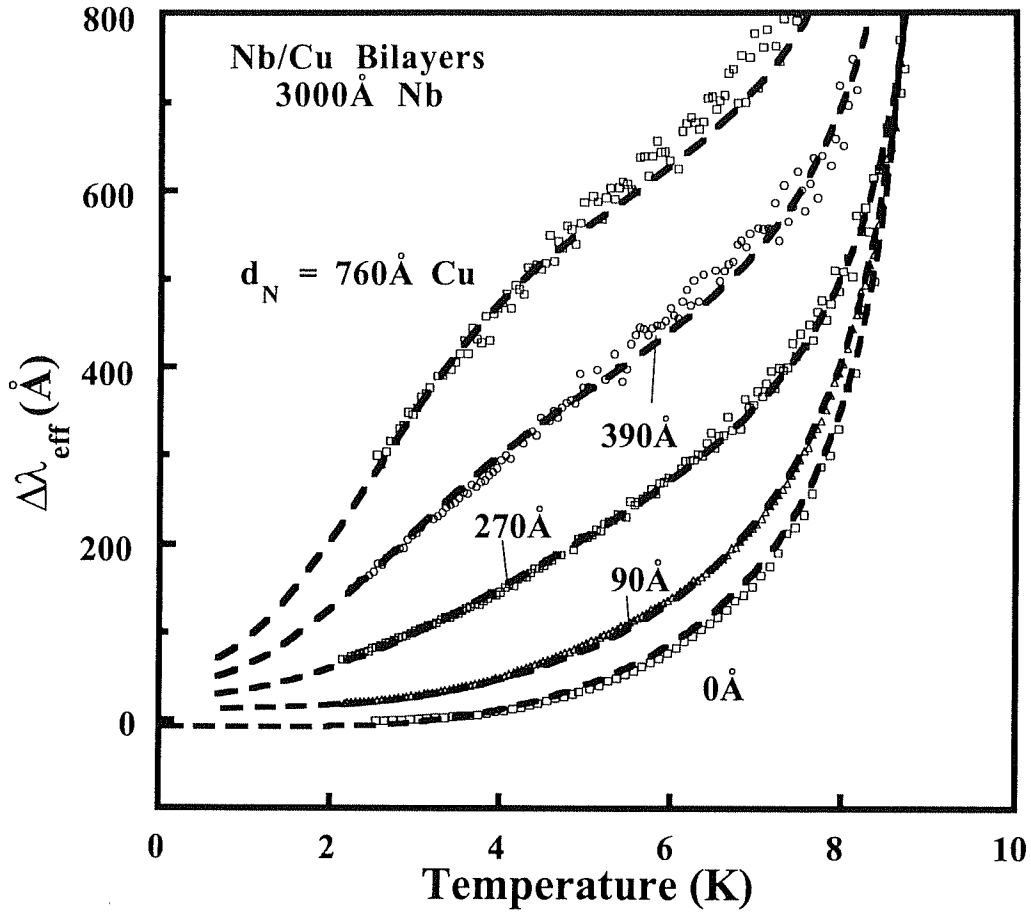
Fig. 4.19. Effective penetration depth vs. temperature for Nb/Cu bilayers, with fits to the model treating screening in the normal layer. The temperature dependence of the effective decay length was found to be $K_{eff}^{-1}(T) \sim T^{-2}$.

Table 4.2. Normal metal layer thicknesses and fitting parameters for $\Delta\lambda_{eff}(T)$ data on Nb/Cu bilayers, using the temperature dependence $K_{eff}^{-1}(T) \sim T^{-2}$ for the decay length.

d_N (Å)	$\lambda_N(0,0)$ (Å)	$K_{eff}^{-1}(4.6K)$ (Å)	$\lambda_S(0)$ (Å)	T_c (K)
0	----	-----	353 ± 5	9.17 ± .03
90	470 ± 40	225 ± 10	400 ± 50	9.3 ± .05
270	318 ± 15	227 ± 15	300 ± 50	9.3 ± .05
390	363 ± 15	160 ± 20	350 ± 50	9.3 ± .05
760	578 ± 40	285 ± 23	340 ± 20	9.3 ± .05

100

The parameter values of Table 4.2 are quite reasonable and agree fairly well across all of the samples, particularly in the parameters describing the Nb layer. These values also reflect the general behavior described in section 4.3.3. The samples which show a small change of curvature in $\Delta\lambda_{eff}(T)$ at low temperature have a normal layer thickness comparable to or slightly larger than $\lambda_N(0,0)$; these are the samples with $d_N = $ 390Å and 760Å. The other samples ($d_N = $ 90Å and 270Å) have normal layers too thin to screen the RF magnetic field very much, so they exhibit $\Delta\lambda_{eff}(T)$ curves which behave as $\Delta\lambda_{eff}(T) \sim T$ at low temperature, with no visible change in curvature. Additionally, for the $d_N = $ 390Å and 760Å samples, the value of K_{eff}^{-1} is comparable to d_N around the temperature where the change in curvature of $\Delta\lambda_{eff}(T)$ occurs (3.5K for $d_N = $ 390Å and 3K for $d_N = $ 760Å). Again, the error bars quoted in Table 4.2 reflect the range of values for which the goodness of fit is within 5% of its maximum value.

4.5 Summary

The object of this chapter has been to explore the effect inhomogeneous superconducting properties found in S/N bilayers have on the screening of an applied RF magnetic field, and to develop a method of deducing the two important length scales, $\lambda_N(0,0)$ and $K_{eff}^{-1}(T_c/2)$, in the N layer of proximity-coupled S/N bilayer systems. Since the normal metal layers presented in this thesis are quite thin, the single-frequency approximation of de Gennes and Werthamer could no longer be rigorously applied. Instead, we assumed that the order parameter decays into the N layer on a length scale much smaller than that predicted by the single-frequency approximation, in accordance with the rapid variation of the pair amplitude expected near the interface when the higher-order terms of the kernel $K(\mathbf{r},\mathbf{r}')$ are considered. We approximated the penetration of pair amplitude into N by a decaying exponential function $e^{-K_{eff}(T)|z|}$. The function $K_{eff}^{-1}(T)$ diverges as $T \rightarrow T_{cN}$ ($T \rightarrow 0$ for a nonsuperconducting N metal), as a power

101

law $K_{eff}^{-1} \sim T^{-\alpha}$, where $\alpha \leq 2$. The exponent α is not predicted by theory, since it describes the behavior of an effective decay length, itself only an approximation. It was found that $\alpha = 1/2$ in Al, while $\alpha = 2$ described the behavior of $K_{eff}^{-1}(T)$ in Cu.

The conditions necessary for observing proximity-coupled behavior most prominently in S/N bilayers with the parallel-plate technique are $d_N > \lambda_N(0,0) > K_{eff}^{-1}(T_c/2)$. The approximate values of $\lambda_N(0,0)$ and $K_{eff}^{-1}(T_c/2)$ may be ascertained independent of any assumption about the temperature dependence of $K_{eff}^{-1}(T)$; $\lambda_N(0,0)$ is given approximately by the normal layer thickness beyond which a change in curvature of $\Delta\lambda_{eff}(T)$ is observed as $T \to T_{cN}$, while K_{eff}^{-1} is approximately equal to d_N at the temperature where this change of curvature and more rapid drop occur. By varying d_N, $K_{eff}^{-1}(T)$ may be mapped out in this way. More exact fitting procedures for $\Delta\lambda_{eff}(T)$ on Nb/Al and Nb/Cu, using exponents $\alpha = 1/2$ and $\alpha = 2$ respectively, yielded values of $K_{eff}^{-1}(T_c/2)$ and $\lambda_N(0,0)$ in full accordance with these general guidelines.

Finally, we note that the effect of the suppression of the order parameter $\Delta(z)$ in the S layer due to the presence of N was found to be negligible, and that, except for the case where N is a ferromagnetic material, the induced superconductivity in the N layer is primarily responsible for the altered screening properties at low temperature observed in S/N bilayers.

Chapter 5
Theory of RF Loss in Proximity-Coupled Systems

5.0 Chapter Overview

This chapter explores some new territory which has not been accessible to previous experiments - the absorption of electromagnetic radiation by the spatially inhomogeneous spectrum of normal excitations above the induced superconducting condensate in very thin proximity-coupled normal metal films. We seek in this chapter to develop a model which can provide an intuitive understanding of this absorption process from the viewpoint of an experimentalist, without getting too deep in theory. We show in particular that in the normal metal layer, a local real part of the conductivity $\sigma_{1N}(z,T)$, possessing the same effective decay length scale $K_{eff}^{-1}(T)$ as that used to describe the local penetration depth $\lambda_N(z,T)$ in Chapter 4, can reproduce the surface resistance data on proximity-coupled Nb/Al and Nb/Cu bilayers given in Ch. 3. We find that the decrease in R_s as $T \rightarrow T_{cN}$ ($T \rightarrow 0$ for Cu) can result either from a shift in the location of screening currents or from a shift in the spatial distribution of normal excitations, and plots of the local RF loss profile in S/N bilayers are provided. Finally, we conclude that any correct treatment of the problem must address the existence of coherence effects between the normal excitations above the condensate in the normal layer, and demonstrate that these coherence effects are very much in evidence in thin proximity-coupled Al and Cu layers.

The chapter begins by developing the concept of surface impedance, relating it to the complex Poynting vector integrated over the film surface. This leads to a derivation of how to calculate the surface impedance of a film with spatially inhomogeneous superconducting properties described by a position dependent real part of the conductivity $\sigma_{1N}(z,T)$. It then considers the particular dependence on temperature and

position appropriate to $\sigma_{1N}(z,T)$, and demonstrates some sample calculations of $R_S(T)$ for typical bilayer parameters using two models for $\sigma_{1N}(z,T)$. Finally, fits to the R_S data of Ch. 3 are performed, and the conclusions regarding coherence effects in the N layer are explained.

5.1 The Poynting Vector and Surface Impedance

To discuss absorption of radiation we consider the flow of electromagnetic energy into a superconducting film, using the Poynting vector. The energy flow along a transmission line can be described by the Poynting vector $\mathbf{S} = (\mathbf{E} \times \mathbf{B})/\mu_0$, which in the absence of field penetration into the plates always points in the direction parallel to the superconducting plates, transporting energy along the transmission line. When fields and currents penetrate into the plates, however, an electric field $\mathbf{E}_{||}$ arises parallel to the plates. Since $\mathbf{B}$ is always parallel to the plates as well, this creates a component of the Poynting vector $\mathbf{S}_\perp = (\mathbf{E}_{||} \times \mathbf{B})/\mu_0$ pointing into the films at the surface. If a current of
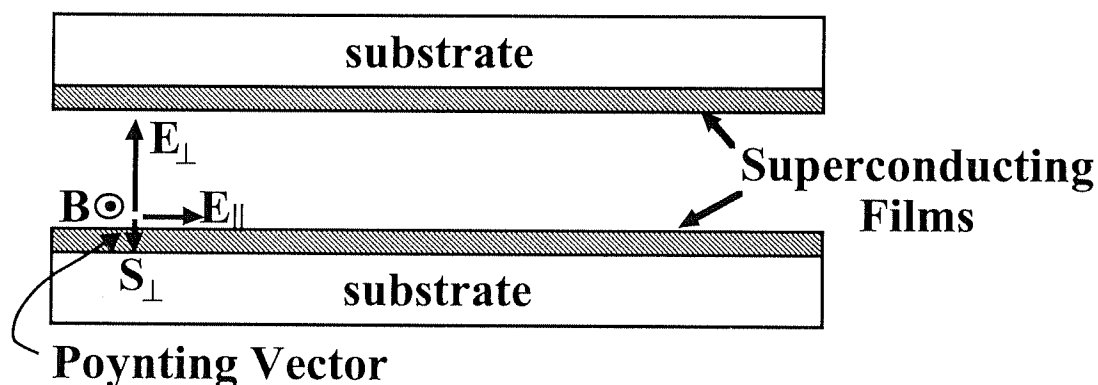
Fig. 5.1. Diagram showing the electromagnetic field components and the resulting Poynting vector pointing into the superconducting plates of a parallel-plate resonator.

104

thermally activated normal excitations flows in response to this electric field, $E_{||}$ develops a real component and work is done by the currents flowing in the film. Of course, the large imaginary component of $E_{||}$ still causes most of the energy flowing into the film to be stored in magnetic fields and in the kinetic energy of supercurrents, leading to inductance. This situation is depicted in Fig. 5.1.

For RF fields which vary as $e^{i\omega t}$, we may calculate the Poynting vector in terms of complex field and current amplitudes inside the film. We begin by considering a portion of film, with top surface area A and film thickness s, shown in Fig. 5.2. We assume that the area A is small, so that the fields $E_{||}$ and B are constant across A. The rate of energy flow into the volume of film is given by the integral of the perpendicular component of the Poynting vector over all surfaces of the volume $V = As$:
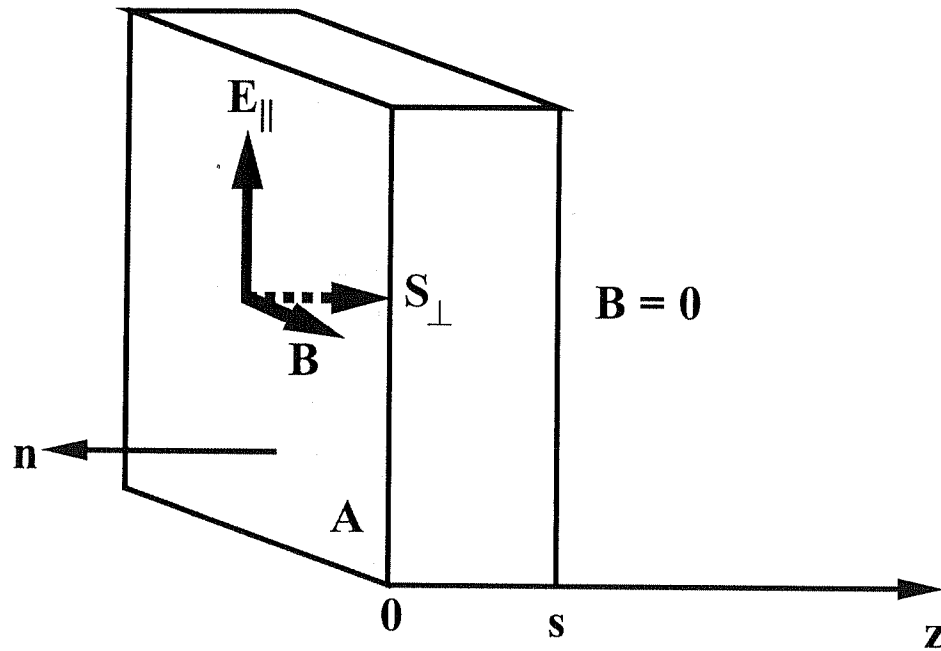
Fig. 5.2. Columnar section of a thin film, showing fields $E_{||}$ and B, and the perpendicular Poynting vector $S_{\perp}$.

$$P = - \int_{\substack{\text{all} \\ \text{surfaces}}} \frac{(\mathbf{E}_\parallel \times \mathbf{B})}{\mu_0} \cdot d\mathbf{n} = - \int_V \nabla \cdot \frac{(\mathbf{E}_\parallel \times \mathbf{B})}{\mu_0} dV \qquad (5.1)$$

where the normal $\mathbf{n}$ is directed outward, the negative signs represent flow into the volume V, and the divergence theorem has been used to obtain the right side of (5.1). Since the fields $\mathbf{E}_\parallel$ and $\mathbf{B}$ are parallel to the surface, the Poynting vector $\mathbf{S}_\perp$ has no components normal to the side walls of the volume V, so only the front and back surfaces of the volume need be considered for the integral. Furthermore, since $\mathbf{B} = 0$ for $z > s$ in a parallel-plate resonator, the Poynting vector is zero on the back surface of the film. Hence only the front surface contributes. The left side of (5.1) is equal to $- (A/\mu_0) \, (\mathbf{E}_\parallel \times \mathbf{B})_{z=0}$, since the integrand can be moved outside the integral. Dividing both sides of (5.1) by A, we get

$$- \frac{\mathbf{E}_\parallel(0) \times \mathbf{B}(0)}{\mu_0} = - \int_0^s \nabla \cdot \frac{(\mathbf{E}_\parallel \times \mathbf{B})}{\mu_0} dz \qquad (5.2)$$

$$= - \frac{1}{\mu_0} \int_0^s \left[\mathbf{B} \cdot \left(\nabla \times \mathbf{E}_\parallel \right) - \mathbf{E}_\parallel \cdot \left(\nabla \times \mathbf{B} \right) \right] dz \qquad (5.3)$$

If we assume that $\mathbf{B}, \mathbf{E}_\parallel \sim e^{i\omega t}$, then two of Maxwell's equations take the forms $\nabla \times \mathbf{E}_\parallel = -i\omega\mathbf{B}$ and $\nabla \times \mathbf{B} = \mu_0\mathbf{J} + i\omega\varepsilon_0\mu_0\mathbf{E}_\parallel$ inside the film. Inserting these into (5.3), we find

$$-\frac{\mathbf{E}_{\parallel}(0) \times \mathbf{B}(0)}{\mu_0} = \frac{1}{\mu_0}\left(\frac{\mathbf{E}_{\parallel}(0)}{\mathbf{B}(0)}\right)B^2(0) = i\omega\int_0^S \left[\frac{B^2(z)}{\mu_0} + \varepsilon_0 E_{\parallel}^2(z)\right]dz + \int_0^S \mathbf{E}_{\parallel}(z)\cdot\mathbf{J}(z)\,dz \quad (5.4)$$

Recognizing the first and second terms on the right side of (5.4) as the rate of increase of electric and magnetic field energy per unit area and the work done per unit area in the film, respectively, we see that Eq. (5.4) is a statement of energy conservation. If we choose $\mathbf{B}$ and $\mathbf{J}$ to be real for simplicity, $\mathbf{E}$ is in general complex. This equation is therefore complex; the real part of Eq. (5.4) represents the energy lost as heat, while the imaginary part represents energy stored inductively.

If we define the surface impedance by $Z_S = R_S + iX_S = \mu_0(E_{\parallel}(0)/B(0))$, then the real part of (5.4) yields

$$R_S = \frac{\omega\mu_0^2\varepsilon_0}{B^2(0)}\,\mathrm{Im}\int_0^S E_{\parallel}^2(z)dz + \frac{\mu_0^2}{B^2(0)}\,\mathrm{Re}\int_0^S \mathbf{E}_{\parallel}(z)\cdot\mathbf{J}(z)\,dz \quad (5.5)$$

and the imaginary part yields

$$X_S = \frac{\omega\mu_0}{B^2(0)}\int_0^S B^2(z)dz + \frac{\omega\mu_0^2\varepsilon_0}{B^2(0)}\,\mathrm{Re}\int_0^S E_{\parallel}^2(z)dz + \frac{\mu_0^2}{B^2(0)}\,\mathrm{Im}\int_0^S \mathbf{E}_{\parallel}(z)\cdot\mathbf{J}(z)\,dz \quad (5.6)$$

If we neglect the displacement current term in Maxwell's equations, then the terms in $E_{\parallel}^2$ do not appear in (5.5) and (5.6); since $E_{\parallel}$ is very small in superconducting systems, we may safely neglect these second order terms. If we do, we see that (5.5) is identical to Eq. (2.26). Equation (5.6) in turn is very simply related to the effective penetration

107

depth λ_{eff} defined in Eq. (4.8), by the relation $X_S = \mu_0 \omega \lambda_{eff}$. So in fact the $\mathbf{E}_{||} \cdot \mathbf{J}$ terms are the most important ones for calculating the surface impedance; the constitutive relation which relates $\mathbf{J}$ and $\mathbf{E}_{||}$ contains all of the physics of the problem. Since the expressions (5.5) and (5.6) provide a relation between the surface impedance and the distribution of fields and currents in a film, they represent a way to calculate R_S and X_S in an inhomogeneous superconducting system such as an S/N bilayer, as long as we know the field and current penetration profiles $B(z)$, $E_{||}(z)$, and $J(z)$.

5.2 Electromagnetic Absorption in Proximity-Coupled S/N Bilayers

In contrast to homogeneous superconducting systems, S/N bilayers exhibit superconducting properties which vary with position. In Ch. 4, a model of the penetration of magnetic field in S/N bilayers was presented, in which the concept of a spatially inhomogeneous superfluid density appeared. This took the form of a position-dependent local penetration depth $\lambda_N(z,T) = \lambda_N(0,T)\, e^{-K_{eff}(T)z}$ in the normal layer, from which the penetration of fields and screening currents was derived.

In a similar fashion, we expect the real part of the conductivity, σ_1, to depend on position in an S/N bilayer, since it is related to the density of thermally excited quasiparticles, which depends on position. This is turn means that the surface resistance of S/N bilayers, which will eventually be calculated with the use of (5.5), may be quite different from that of a homogeneous superconductor. Since the R_s data on Nb/Al and Nb/Cu bilayers presented in Ch. 3 does display interesting low-temperature behavior not characteristic of homogeneous superconducting films, we hope to reproduce the behavior by choosing the correct position and temperature dependence of $\sigma_1(z,T)$.

108

5.2.1 Normal Currents and First-Order Electric Field

The contribution of normal screening currents to the magnetic field penetration profile can be neglected in most superconductors, since the skin depth δ greatly exceeds the penetration depth λ over most of the temperature range $0 < T < T_c$. An exception to this statement occurs very near the transition temperature where thermally excited quasiparticles grow in number, causing δ to decrease, and the superfluid becomes depleted, causing λ to increase. When $\delta \sim \lambda$, a full treatment of the screening of magnetic field, including normal currents, becomes necessary. In a proximity-coupled S/N bilayer, such a consideration may be necessary even far below T_c for regions of the N layer far from the interface. However, in the thin films under study in this thesis, this is not likely the case. It suffices to use the screening model of section 4.3, in which normal currents were not included, to calculate $B(z)$, and then add normal currents afterward as a first order perturbation for consideration of RF losses.

The parallel electric field is related to the acceleration of the superfluid, which in an S/N bilayer may be expressed by a local version of the 1st London equation:

$$E_{\parallel}(z,T) = \frac{d}{dt}\left[\mu_0\lambda_N^2(z,T)J_S(z,T)\right]$$

$$= i\omega\mu_0\lambda_N^2(z,T)J_S(z,T) \tag{5.7}$$

This electric field also drives a normal current $J_N(z,T)$ given by

$$J_N(z,T) = \sigma_1(z,T)E_{\parallel}(z,T) \tag{5.8}$$

These two currents add, yielding the relation

$$J(z,T) = J_N(z,T) + J_S(z,T) = \left[\sigma_1(z,T) - i\sigma_2(z,T)\right]E_{\parallel}(z,T) \tag{5.9}$$

where we have made the substitution $\sigma_2(z,T) = [\omega\mu_0\lambda_N^2(z,T)]^{-1}$. Inverting (5.9) to obtain the expression for the first-order electric field, we can then use (5.5) to obtain the expression for surface resistance:

$$R_S = \frac{\mu_0^2}{B^2(0)} \int_0^s \frac{\sigma_1(z,T)}{\sigma_1^2(z,T) + \sigma_2^2(z,T)} J^2(z,T)dz \qquad (5.10)$$

It should be noted at this point that it is not correct to simply take the real part of the ratio of electric and magnetic fields at the surface, as defined by Eq. (2.21); this would yield

$$R_S = \mu_0 \frac{\sigma_1(0,T)}{\sigma_1^2(0,T) + \sigma_2^2(0,T)} \frac{J(0,T)}{B(0)} \qquad (5.11)$$

which would give the same value of R_S regardless of what function $\sigma_1(z,T)$ was used, so long as it had the same value at $z = 0$. Such a result would therefore be independent of the particular spatial dependence of $\sigma_1(z,T)$, which clearly cannot be the case, since the local loss must depend on the local current **and** the local excited quasiparticle density. The reason Eq. 2.21 cannot be used is that the function $\sigma_1(z,T)$ has not been used in calculating the field profiles, so that the influence of its spatial dependence has not been incorporated into any of the constants $\mathcal{A}$, $\mathcal{B}$, $\mathcal{C}$, or $\mathcal{D}$ appearing in the magnetic field expressions (4.26) and (4.27). For this reason, the first-order surface resistance can only be calculated by integration using (5.10); this usually means numerical integration.

5.2.2 Surface Resistance Expression in S/N Bilayers

To write down a final expression for R_s in S/N bilayers, we use the expressions for the current density $J(z) = (1/\mu_0) \, dB/dz$, calculated from the magnetic field profiles given in (4.26) and (4.27). The approximation made here is simply to assume that these magnetic field profiles are exact, though they were derived neglecting normal currents. The total current densities in the N and S layers are then:

110

where we have made the substitution $\sigma_2(z,T) = [\omega\mu_0\lambda_N^2(z,T)]^{-1}$. Inverting (5.9) to obtain the expression for the first-order electric field, we can then use (5.5) to obtain the expression for surface resistance:

$$R_S = \frac{\mu_0^2}{B^2(0)} \int_0^S \frac{\sigma_1(z,T)}{\sigma_1^2(z,T) + \sigma_2^2(z,T)} J^2(z,T)dz \qquad (5.10)$$

It should be noted at this point that it is not correct to simply take the real part of the ratio of electric and magnetic fields at the surface, as defined by Eq. (2.21); this would yield

$$R_S = \mu_0 \frac{\sigma_1(0,T)}{\sigma_1^2(0,T) + \sigma_2^2(0,T)} \frac{J(0,T)}{B(0)} \qquad (5.11)$$

which would give the same value of R_S regardless of what function $\sigma_1(z,T)$ was used, so long as it had the same value at $z = 0$. Such a result would therefore be independent of the particular spatial dependence of $\sigma_1(z,T)$, which clearly cannot be the case, since the local loss must depend on the local current **and** the local excited quasiparticle density. The reason Eq. 2.21 cannot be used is that the function $\sigma_1(z,T)$ has not been used in calculating the field profiles, so that the influence of its spatial dependence has not been incorporated into any of the constants $\mathcal{A}$, $\mathcal{B}$, $\mathcal{C}$, or $\mathcal{D}$ appearing in the magnetic field expressions (4.26) and (4.27). For this reason, the first-order surface resistance can only be calculated by integration using (5.10); this usually means numerical integration.

5.2.2 Surface Resistance Expression in S/N Bilayers

To write down a final expression for R_s in S/N bilayers, we use the expressions for the current density $J(z) = (1/\mu_0)$ dB/dz, calculated from the magnetic field profiles given in (4.26) and (4.27). The approximation made here is simply to assume that these magnetic field profiles are exact, though they were derived neglecting normal currents. The total current densities in the N and S layers are then:

110

$$\frac{J(z,T)}{B(0)} = \frac{J(p)}{B(0)} = \frac{K_{eff}(T)}{\mu_0} \left[\mathcal{A}p^2 I_0(p) - \mathcal{B}p^2 K_0(p) \right] \qquad , \quad z < 0 \qquad (5.12)$$

$$\frac{J(z,T)}{B(0)} = \frac{1}{\mu_0\lambda_S(T)} \left[\mathcal{C} e^{z/\lambda_S(T)} - \mathcal{D} e^{-z/\lambda_S(T)} \right] \qquad , \quad z > 0 \qquad (5.13)$$

in the normal and superconducting layers, respectively. Here, $p = p(z,T)$ is given by (4.23) and the constants $\mathcal{A}$, $\mathcal{B}$, $\mathcal{C}$, and $\mathcal{D}$ are given by (4.30) - (4.33). Thus the integral expression for R_s in S/N bilayers is:

$$R_s(T) = \int_{-d_N}^{0} \frac{\sigma_{1N}(z,T)}{\sigma_{1N}^2(z,T) + \left[\dfrac{1}{\omega\mu_0\lambda_N^2(z,T)}\right]^2} \left(p^2 K_{eff}(T)\right)^2 \left[\mathcal{A}I_0(p) - \mathcal{B}K_0(p)\right]^2 dz + $$

$$\qquad (5.14)$$

$$\int_{0}^{d_S} \frac{\sigma_{1S}(T)}{\sigma_{1S}^2(T) + \left[\dfrac{1}{\omega\mu_0\lambda_S^2(T)}\right]^2} \frac{1}{\lambda_S^2(T)} \left[\mathcal{C} e^{z/\lambda_S(T)} - \mathcal{D} e^{-z/\lambda_S(T)}\right]^2 dz$$

Here, $\sigma_{1N}(z,T)$ and $\sigma_{1S}(T)$ are the real parts of the conductivity in the N and S layers, respectively; they may be different, in general. Since all properties of the S layer are assumed to be homogeneous, $\sigma_{1S}(T)$ is given no dependence on z. While the first integral must be done numerically, the second can be done exactly. The final result is

111

$$R_s(T) = \int_{-d_N}^{0} \frac{\sigma_{1N}(z,T)}{\sigma_{1N}^2(z,T) + \left[\dfrac{1}{\omega\mu_0\lambda_N^2(z,T)}\right]^2} \left(p^2 K_{eff}(T)\right)^2 \left[\mathcal{A}I_0(p) - \mathcal{B}K_0(p)\right]^2 dz +$$

$$\frac{\sigma_{1S}(T)}{\lambda_s^2(T)} \frac{1}{\sigma_{1S}^2(T) + \left[\dfrac{1}{\omega\mu_0\lambda_s^2(T)}\right]^2} \left\{\frac{\lambda_s(T)\,\mathcal{C}^2}{2}(e^{2d_s/\lambda_s}-1) - 2\mathcal{C}\mathcal{D}d_s - \frac{\lambda_s(T)\,\mathcal{D}^2}{2}(e^{-2d_s/\lambda_s}-1)\right\}$$

(5.15)

5.3 Temperature and Position Dependence of $\sigma_{1N}(z,T)$

The temperature and spatial dependence chosen for $\sigma_{1N}(z,T)$, the real part of the conductivity in the N metal, is extremely important because it needs to correctly reflect both the penetration of superconducting order into the N layer and the nature of the transitions between the quasiparticle states associated with that induced superconductivity. Two possibilities are given below.

5.3.1 Two-Fluid Model

A simple model of a superconductor which is often used for phenomenological interpretation despite being incorrect is the **two-fluid model**. This model states that, of the electrons available in the superconductor, a fraction $n_S(T)$ are "superconducting" and the rest $n_N(T)$ are "normal". The normal and superconducting fractions are functions of temperature designed so that $n_N(T) + n_S(T) = 1$, i.e., the total number of electrons is constant over the temperature range $0 < T < T_c$. Thus the temperature dependence chosen for $n_S(T)$, which is related to the penetration depth temperature dependence by $\lambda(T) \sim n_S(T)^{-1/2}$, determines the temperature dependence of $n_N(T)$, which would

112

presumably be related to the real part of the conductivity by $\sigma_1(T) \sim n_N(T)$.

In a proximity-coupled S/N bilayer, one can apply a two-fluid model generalized to account for the spatial variation of the order parameter. If we adopt the model of section 4.3 and only give the normal layer spatially inhomogeneous properties, we write $n_N(z,T) + n_S(z,T) = 1$ for the normal layer, where now the temperature **and** position dependences of the normal fraction $n_N(z,T)$ are completely determined by those of the superconducting fraction $n_S(z,T)$. In the superconducting layer the original position-independent expression applies. If we assume that $\sigma_{1N}(z,T) \sim n_N(z,T)$, which seems reasonable enough, then we can use the assumed temperature and position dependences of $\lambda_N(z,T)$ introduced in Chapter 4 to derive the appropriate functional dependences of $\sigma_{1N}(z,T)$, which is the quantity sought.

While it is evident that $n_N(z,T_c) = 1$ (all carriers everywhere are normal at T_c), it is not necessarily the case that $n_N(z,0) = 0$ in a proximity coupled normal metal, since the induction of superconducting properties into the N metal may occur only partially even at $T = 0$. We therefore must assume that a position dependent residual normal fraction $n_R(z)$ exists at $T = 0$. The remaining fraction of the carriers, $1 - n_R(z)$, are "superconducting" at $T = 0$. Hence the local superconducting fraction is given by

$$n_S(z,T) = [1 - n_R(z)] \frac{\lambda_N^2(z,0)}{\lambda_N^2(z,T)} \qquad (5.16)$$

The local normal fraction is therefore given by

$$n_N(z,T) = n_R(z) + [1 - n_R(z)]\left(1 - \frac{\lambda_N^2(z,0)}{\lambda_N^2(z,T)}\right) \qquad (5.17)$$

Since the real part of the conductivity in N must converge to the normal state conductivity

113

σ_N of the N layer at $T = T_c$, we can write

$$\sigma_{1N}(z,T) = \sigma_N \, n_N(z,T) \qquad\qquad (5.18)$$

Chapter 4 introduced the functional dependence of $\lambda_N(z,T)$, so only the residual normal fraction $n_R(z)$ remains unknown.

For thin normal layers, however, $n_R(z)$ is likely to be nearly zero everywhere, since we expect very good superconducting properties to appear across the entire thickness of the N layer near zero temperature. In the superconducting layer, we may assume zero residual normal fraction, and also no z-dependence, so that (5.17) is simplified greatly. An expression for $\sigma_{1S}(T)$ equivalent to Eq. (5.18) is used in the S layer, although the normal state conductivity σ_S in S may be quite different from that of the N layer. With these functional dependences derived, we now explore some implications of the two-fluid model in an effort to reproduce R_S data in real S/N bilayers.

Figure 5.3 shows the surface resistance vs. temperature for a typical Nb/Cu bilayer with $d_N = 3000\text{Å}$ and $d_S = 1000\text{Å}$, using the two-fluid model locally to obtain the temperature dependence of $\sigma_{1N}(z,T)$. The normal state conductivity in the S layer was chosen to be $\sigma_S = 10^8$ $(\Omega\text{-m})^{-1}$, and the value of that quantity in the N layer was allowed to vary from 10^7 to 10^9 $(\Omega\text{-m})^{-1}$. These parameters were chosen because they are typical of the bilayer films for which data was presented in Ch. 3. Evidently, these curves do not reproduce the data of Figs. 3.3 and 3.5; the downturn in $R_s(T)$ as $T \rightarrow T_{cN}$ observed in the bilayer data does not come close to the huge peak in R_s predicted here by the two-fluid model. Even for $\sigma_N = 0.1 \, \sigma_S$ (the lowest curve), there is still a shallow peak at low temperature.

Figure 5.4 depicts the expected dependence on normal layer thickness using the two fluid model for the temperature dependence of $\sigma_{1N}(z,T)$. The same parameters as in Fig. 5.3 are used, with $\sigma_S = 10^8$ $(\Omega\text{-m})^{-1}$ and $\sigma_N = 2 \times 10^8$ $(\Omega\text{-m})^{-1}$. Although the

114

calculation for a bilayer with d_N = 200Å does seems to reproduce the general downturn of the bilayer R_s data given in Ch. 3, the dependence on d_N does not agree with experiment. There is, as discussed above, no feature resembling the large peak in R_s at
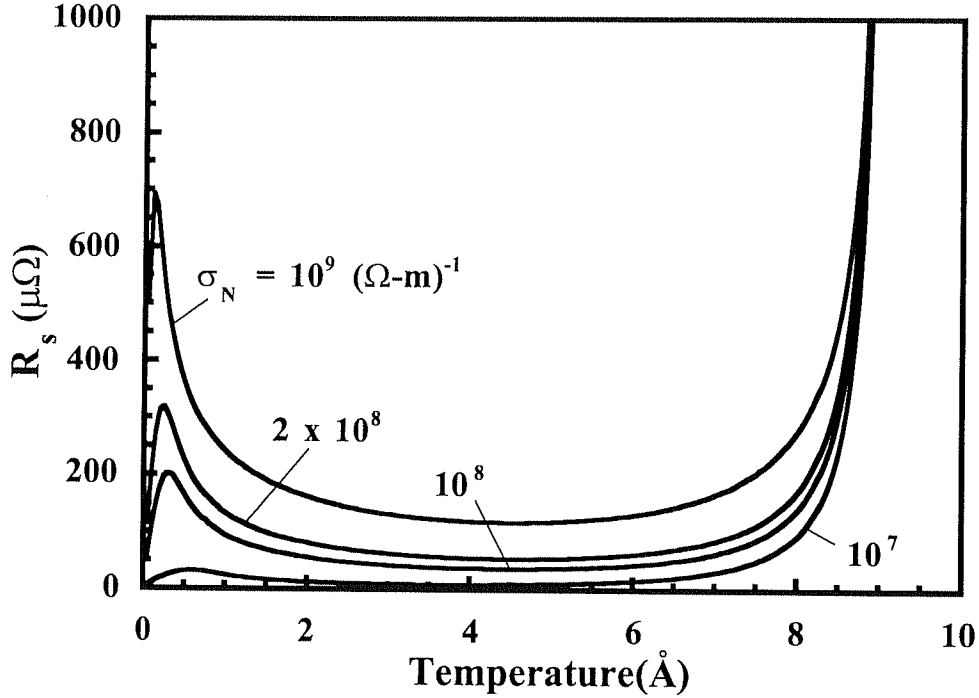
Fig. 5.3. Calculated surface resistance vs. temperature for a hypothetical Nb/Cu bilayer using the generalized two-fluid model for $\sigma_{1N}(z,T)$, and varying the normal state conductivity σ_N of the N layer from 10^7 to 10^9 $(\Omega\text{-m})^{-1}$. Parameter values are: d_S = 3000Å, d_N = 1000Å, $\lambda_N(0,0)$ = 300Å, $K_{eff}^{-1}(T_c/2)$ = 100Å, $\lambda_S(0)$ = 350Å, T_c = 9.2K, and normal state conductivity of the S layer $\sigma_S = 10^8$ $(\Omega\text{-m})^{-1}$. The prominent peak at low temperature is not seen in the data.

low temperature like the one predicted by the two-fluid model in Fig. 5.4. Though the temperature dependence of R_s does become stronger at low temperature as d_N increases, no peak is observed.

This peak was always present at some low temperature in calculations employing the two fluid model, and could never be reconciled with the actual data, which decreases more rapidly at low temperature, but never exhibits a pronounced peak like that shown in

Figs. 5.3 and 5.4. Eventually it became clear that the two fluid model was too phenomenological in nature, and a more fundamental model for $\sigma_{1N}(z,T)$ was sought.
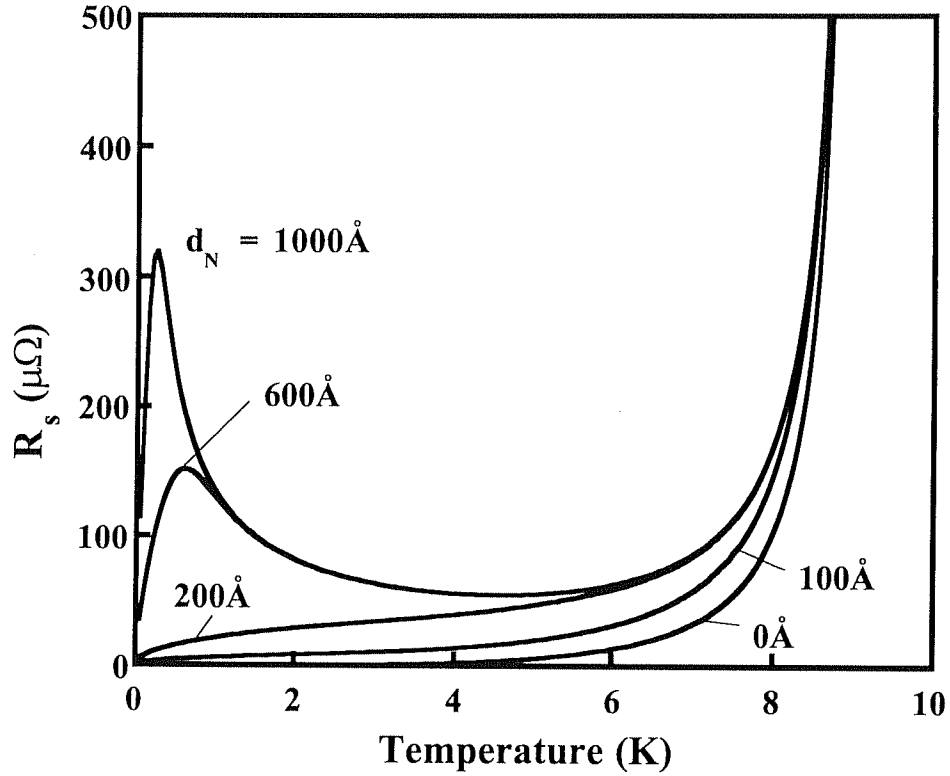
Fig. 5.4. Normal layer thickness dependence of $R_s(T)$ using the two fluid model. Parameters identical to those of Fig. 5.3 were used. The normal state conductivities were $\sigma_S = 10^8$ $(\Omega\text{-m})^{-1}$ and $\sigma_N = 2 \times 10^8$ $(\Omega\text{-m})^{-1}$. Although the parameters used in this calculation are entirely typical, the large peak in R_s at low temperature, which increases in size as d_N increases, is not observed in the R_s data of either Nb/Al or Nb/Cu.

5.3.2 Mattis-Bardeen Theory

The two fluid model presented in the previous section, while convenient for a phenomenological understanding of the electrodynamics of superconductors, falls short in many fundamental ways. In particular, it utterly fails to describe any sort of quantum mechanical transition process, which in the end must underlie the absorption of electromagnetic radiation. Evidently a much more fundamental description of

116

electromagnetic absorption is required.

The Mattis-Bardeen theory [59] achieves such a description for homogeneous superconductors. It essentially does the following: for radiation of frequency ω, it calculates the transition rate for all possible transitions from energy E to energy E + $\hbar\omega$, minus the emission rates for the reverse processes, taking into account the thermally excited population of states at energies E and E + $\hbar\omega$ and the gapped density of states N(E) given by the BCS theory. It then sums the net transition rates over all values of E, yielding the real part of the conductivity expressed relative to its normal state value. It also includes the effect of pair breaking transitions if $\hbar\omega$ > 2Δ, where Δ is the superconducting energy gap. It is a much more agreeable method on theoretical grounds, since it incorporates the singular density of states just above the gap edge and since its temperature dependence comes only from Fermi functions and the temperature dependence of the gap Δ(T). It is not important to the goals of this thesis to describe the Mattis-Bardeen theory in greater detail, so only the final result for σ_1 in a homogeneous superconductor is quoted here [59]:

$$\frac{\sigma_1}{\sigma_N} = \frac{\sigma_1(\omega,\Delta,T)}{\sigma_N} = \frac{2}{\hbar\omega} \int_{\Delta}^{\infty} \left[f(E) - f(E+\hbar\omega) \right] g(E) \, dE + \frac{1}{\hbar\omega} \int_{\Delta - \hbar\omega}^{-\Delta} \left[1 - 2f(E+\hbar\omega) \right] g(E) \, dE$$

(5.19)

with

$$g(E) = \frac{E \, (E+\hbar\omega) + \Delta^2}{\left[E^2 - \Delta^2 \right]^{1/2} \left[(E+\hbar\omega)^2 - \Delta^2 \right]^{1/2}}$$

(5.20)

The second integral in (5.19) is only performed if $\hbar\omega$ > 2Δ.

Figure 5.5 shows the temperature dependence of σ_1(T) in a homogeneous superconductor, calculated using the two fluid model and the Mattis-Bardeen theory. The peak in σ_1(T) at T = 0.7 T_c is a feature observed in real data and predicted by the

117
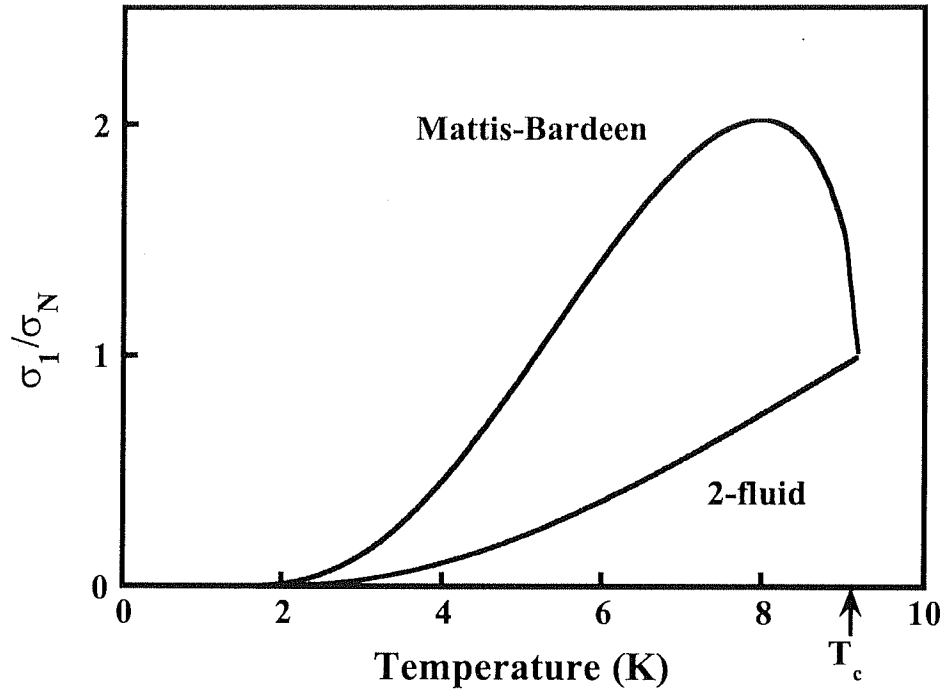
Fig. 5.5. Temperature dependence of the real part of the conductivity $\sigma_1(T)$ in a homogeneous superconductor, using the two fluid model and the Mattis Bardeen model at 10 GHz, and assuming a gap equal to 1.76 $k_B T_c$.

Mattis-Bardeen theory - it is one of the great successes of the theory. A glance at Fig. 5.5 clearly shows that something important is being neglected when the two-fluid model is used. The peak in the Mattis-Bardeen σ_1 is due to case II coherence effects [109], which are a consequence of phase coherence between excitations above the superconducting condensate, and which are only detectable with experiments whose perturbation Hamiltonian is odd under time-reversal of the electronic states participating in Cooper pairing. Since electromagnetic absorption is such an experiment, such effects must be considered in any model of RF loss in a superconducting system.

5.3.3 Coherence Effects in the N Metal and the Adapted Mattis-Bardeen Model

In light of the above statement, it stands to reason that case II coherence effects may occur, at least partially, between excitations above the induced superconducting condensate in a proximity-coupled normal metal. Since many of the previous experiments on S/N bilayer systems have not been sensitive to these effects, this idea has not been explored much. The nuclear spin-lattice relaxation rate $1/T_1$ of Cu ions in Nb/Cu multilayers measured by Zheng [62] was consistent with the concept of coherence effects in the Cu layers; we show below that the behavior of the surface resistance in Nb/Cu and Nb/Al bilayers is also consistent with a model in which case II coherence effects in the normal layer play a role.

The model used to calculate $\sigma_{1N}(z,T)$ is an adapted Mattis-Bardeen model, in which a local BCS gap $\Delta_N(z,T)$ replaces the spatially constant one found in homogeneous superconductors. The Mattis-Bardeen expression (5.19) is used to calculate $\sigma_{1N}(z,T) = \sigma_{1N}(\omega, \Delta_N(z,T), T)$, from which the surface resistance may be calculated using (5.15). The local gap $\Delta_N(z,T)$ is given an exponentially decaying dependence on z, with the same decay length $K_{eff}^{-1}(T)$ as was used to describe the local penetration depth:

$$\Delta_N(z,T) = \frac{\Delta_S(T)}{\alpha} \exp\left(-K_{eff}(T)|z|\right) \quad , \quad z < 0 \qquad (5.20)$$

Here, $\Delta_S(T)$ is the temperature-dependent energy gap in the adjoining S layer, and α is a factor usually found to be approximately unity. Because in theory it is the pair potential $\Delta(z)$, and not a true energy gap $\Delta_N(z)$, which penetrates into the N layer in this way, equation (5.20) is not actually rigorous. However, it does allow one to form an equivalent picture of the absorption of energy occurring locally and still includes the primary length scale $K_{eff}^{-1}(T)$.

5.3.4 Sample Calculations of $R_s(T)$

Figure 5.6 shows the dependence of the calculated $R_s(T)$ curves on normal layer thickness, for an S/N bilayer with $d_S = 3000\text{Å}$, $\lambda_N(0,0) = 300\text{Å}$, $K_{eff}^{-1}(T_c/2) = 100\text{Å}$, and $\lambda_S(0) = 350\text{Å}$, using the adapted Mattis-Bardeen model with $\Delta_S(0) = 1.76\ k_B T_c$ and $\alpha = 1$. Here, the normal state conductivities were taken to be $\sigma_N = \sigma_S = 10^8\ (\Omega\text{-m})^{-1}$. In contrast to the two-fluid behavior of Fig. 5.4, the curves in Fig. 5.6 do resemble the R_s data on Nb/Al and Nb/Cu data very much. For small d_N, a linear term in the temperature dependence of R_s appears at low temperature, while for thicker samples, a distinct drop seems to occur at a temperature which varies with normal layer thickness. This is the temperature where $K_{eff}^{-1} \approx d_N$, and this condition occurs at progressively lower temperatures as d_N increases. For very thick normal layers, the sample would seem to
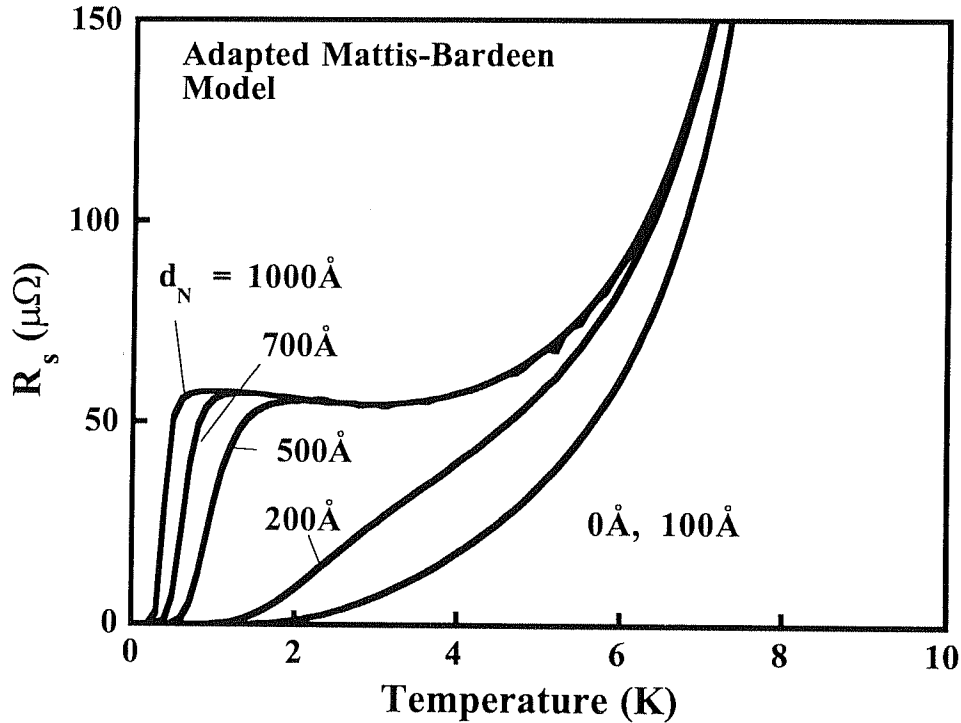

Fig. 5.6. Dependence of $R_s(T)$ on normal layer thickness d_N, calculated using the adapted Mattis-Bardeen model at 11 GHz, with parameters $\lambda_S(0) = 350\text{Å}$, $\lambda_N(0,0) = 300\text{Å}$, $K_{eff}^{-1}(T_c/2) = 100\text{Å}$, and $\sigma_N = \sigma_S = 10^8\ (\Omega\text{-m})^{-1}$.

120

have a second, relatively sharp transition at a lower temperature, while thin N layers would simply show the linear behavior of R_S with temperature, without a precipitous drop. In the example shown in Fig. 5.6, the thickness of normal metal which separates these two behaviors is $d_N \sim \lambda_N(0,0) = 300\mathring{A}$, the same condition found in the analysis of the $\Delta\lambda_{eff}$ data. So we see that the R_s data can be used to verify the magnitudes of the length scales $\lambda_N(0,0)$ and $K_{eff}^{-1}(T)$ estimated from the $\Delta\lambda_{eff}$ data.

Figure 5.7 shows the effect of varying the ratio of the normal state conductivities, σ_N/σ_S. This figure used all of the same parameters used in Fig. 5.6, and assumed $d_N = 1000$ and $d_S = 3000\mathring{A}$. According to these calculations, no large peak in R_s should ever occur at low temperature, though nonmonotonic behavior of R_s is possible when
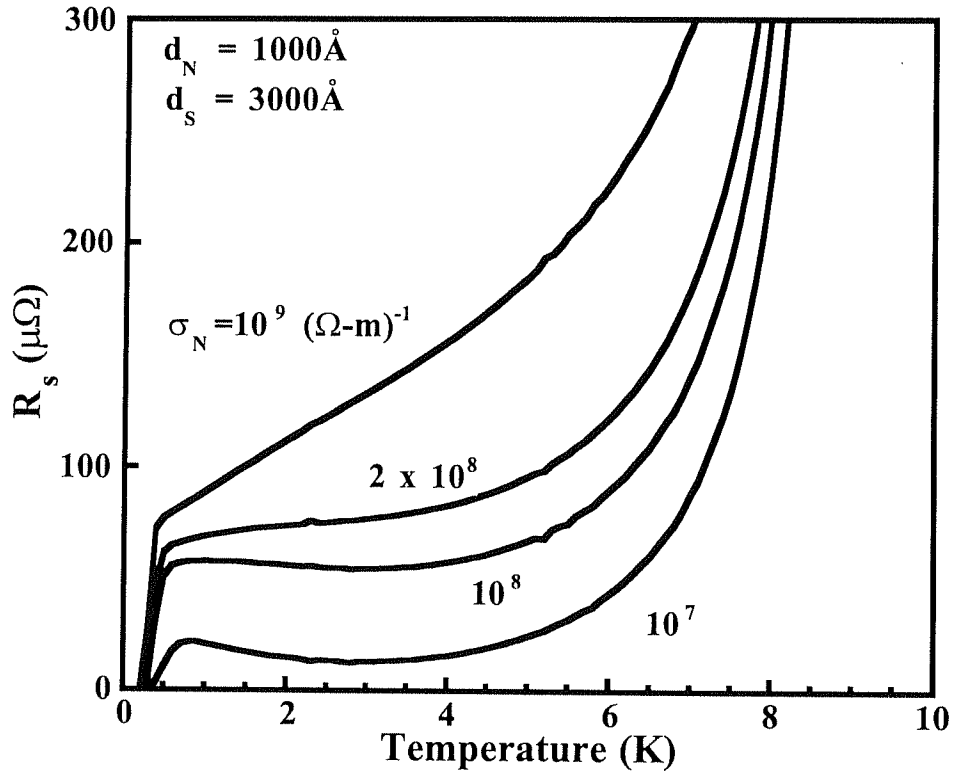

Fig. 5.7. Calculated dependence of $R_s(T)$ on the normal state conductivity σ_N of the normal layer, assuming normal state conductivity $\sigma_S = 10^8$ $(\Omega$-m$)^{-1}$ in the S layer. All other parameters are the same as those used in Fig. 5.6.

121

$\sigma_N << \sigma_S$. Conversely, if $\sigma_N >> \sigma_S$, the losses in the normal layer dominate the total loss in the bilayer, so that a strongly linear dependence on temperature persists down to quite low temperatures.

5.3.5 Local Loss Profiles

To understand the temperature dependences shown in Figs. 5.6 and 5.7 in more detail, it is instructive to plot the local effective resistivity, given by $\rho_{eff}(z,T) = \sigma_{1N}(z,T)/[\sigma_{1N}^2(z,T) + \sigma_{2N}^2(z,T)]$, and the local RF loss, given by $\rho_{eff}(z,T)J^2(z,T)$, as a function of position across the thickness of the bilayer. As Fig. 5.8(a) shows, the distribution of currents does not necessarily change much over the entire temperature range; currents flow more in the N layer at low temperature and more in the S layer at high temperature, but always in the vicinity of the S/N interface in a bilayer with the parameters given above. What does have a strong temperature dependence is the spatial profile of the effective resistivity $\rho_{eff}(z,T)$. As seen in Fig. 5.8(b), it actually has a maximum value at some point **inside** the N layer, a result due to a combination of both of the dependences $\sigma_{1N}(z,T)$ and $\sigma_{2N}(z,T)$. This peak in $\rho_{eff}(z,T)$ moves further out toward the free surface as T -> 0. The resulting local loss $\rho_{eff}(z,T)J^2(z,T)$ therefore is also strongly peaked within the N layer, and this peak diminishes in magnitude and moves further toward the free surface as T -> 0. The surface resistance of the entire bilayer at a given temperature is equal to the area under each curve in Fig. 5.8(c). The diminishing area under each curve in Fig. 5.8(c) explains the decrease in $R_s(T)$ observed in Nb/Al and Nb/Cu bilayer films.

5.4 Fits to R_s Data

Since the adapted Mattis-Bardeen model seems to reproduce much of the behavior observed in S/N bilayers, including the rapid drop at low temperature, we may try to fit
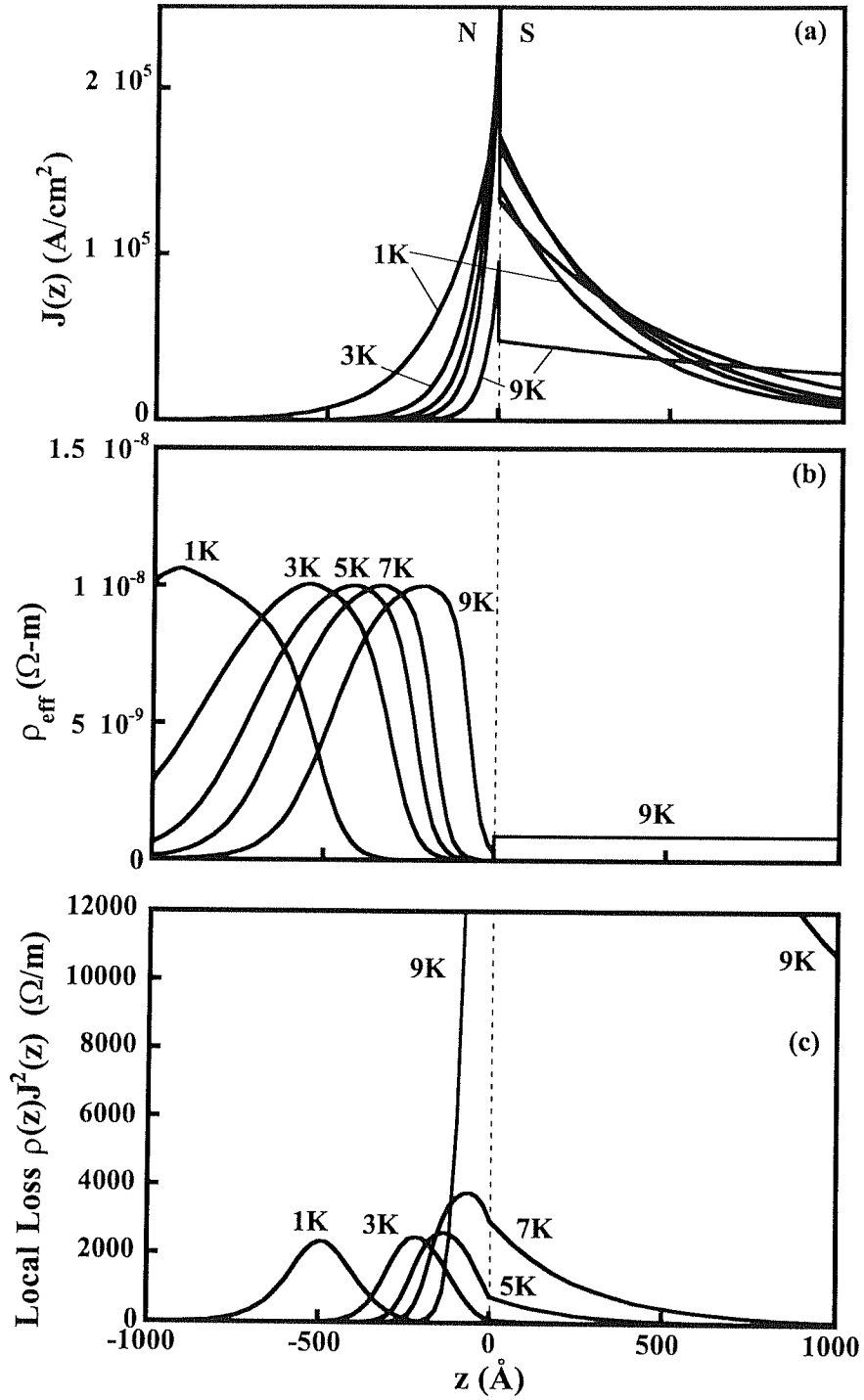
Fig. 5.8. Current density J(z), local resistivity $\rho(z)$, and local loss $\rho(z)J^2(z)$ for an S/N bilayer with layer thicknesses $d_N = 1000\text{Å}$, $d_S = 3000\text{Å}$ and the same parameter values as in Fig. 5.6.

123

this data by assuming a temperature dependence for $K_{eff}^{-1}(T)$ as was done for the $\Delta\lambda_{eff}$ data. If possible, we would like to use the same screening parameters $\lambda_N(0,0)$ and $\lambda_S(0)$, and the same value of $K_{eff}^{-1}(T_c/2)$, as were used in the $\Delta\lambda_{eff}$ fits. The two additional parameters necessary for these fits are the two normal state conductivities σ_N and σ_S.

5.4.1 Nb/Al

The data of Fig. 3.3, which shows the R_s data vs. temperature for Nb/Al bilayers, indicates that there are probably some differences in materials properties among the samples, since R_s does not vary monotonically with d_N. This fact is borne out by the values of σ_N and σ_S emerging from the fitting process. Fig. 5.9 shows the data of Fig. 3.3, together with fits to the adapted Mattis-Bardeen model using a temperature dependence $K_{eff}^{-1}(T) \sim T^{-1/2}$ for the order parameter decay length. The parameters of the fits appear in Table 5.1, with error bars describing the range over which a 5% variation from maximum fit goodness occurs.

While the penetration depth $\lambda_N(0,0)$ and the decay length $K_{eff}^{-1}(T_c/2)$ parameter values for the samples with 100Å and 200Å Al did not agree with the parameter values found by fitting the corresponding $\Delta\lambda_{eff}(T)$ data, the values were in both cases much larger than d_N and therefore acquired large error bars. The values of $\lambda_N(0,0)$ and $K_{eff}^{-1}(T_c/2)$ for the 300Å and 600Å samples are much more in line with the values obtained from $\Delta\lambda_{eff}(T)$ fits.

The values of the normal state conductivity in the normal layer, however, are a bit higher than expected, and in particular do not agree with DC resistivity results. They are instead a result of the adapted Mattis-Bardeen model, which, as was pointed out, is not a rigorous formalism. Essentially the size of the gap $\Delta_N(z)$ which allowed for the best fits to the data, was large and implied a smaller quasiparticle population, requiring a larger σ_N to account for the observed data. So although the model does allow one to discern the
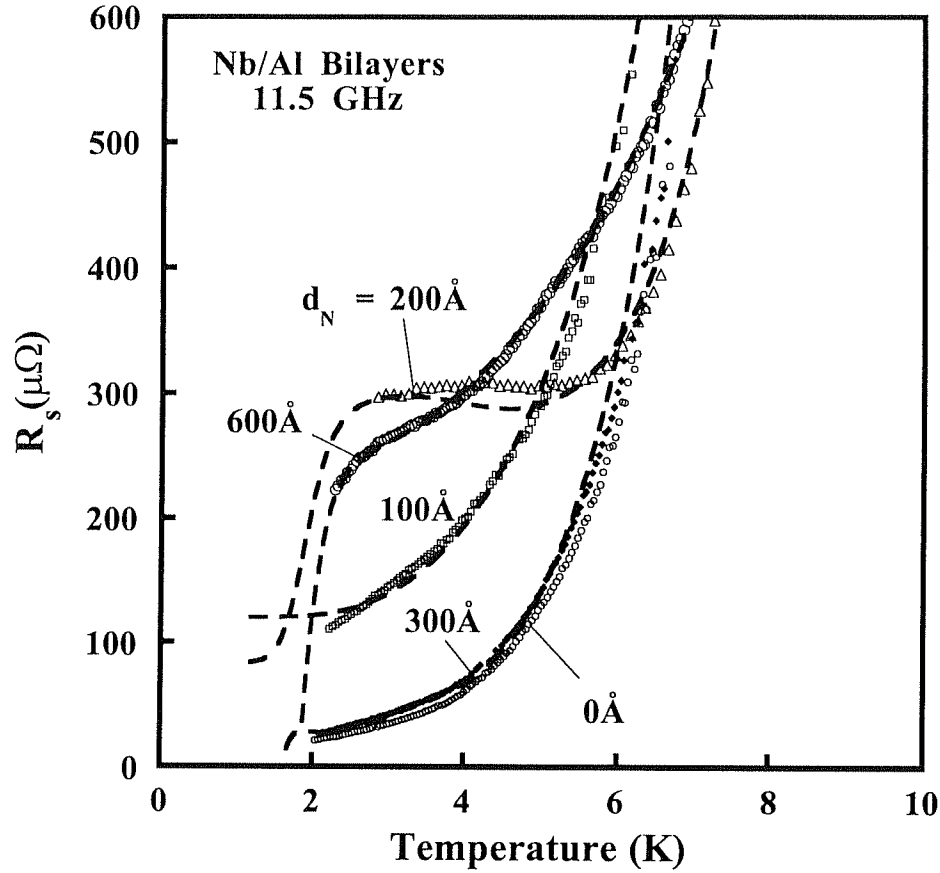
124

Fig. 5.9. Surface resistance data for Nb/Al bilayers with $d_S = 1$ μm and $0 \leq d_N \leq 600$Å, showing fits to the adapted Mattis-Bardeen model. The temperature dependence $K_{eff}^{-1}(T)$ ~ $T^{-1/2}$ was used.

Table 5.1. Normal metal thicknesses and fitting parameters for $R_s(T)$ data on Nb/Al bilayers. Bare Nb data ($d_N = 0$), obtained by removing the Al from the 300Å sample, was fit using the homogeneous Mattis-Bardeen theory. These fits used the same values of $\lambda_S(0)$ and T_c given in Table 4.1. The parameter α was taken to be unity.

d_N (Å)	$\lambda_N(0,0)$ (Å)	$K_{eff}^{-1}(T_c/2)$(Å)	σ_N (10^8 $\Omega^{-1}m^{-1}$)	σ_S(10^8 $\Omega^{-1}m^{-1}$)
0	----	-----	------	0.87 ± 0.05
100	700 ± 300	435 ± 100	$.011 \pm .02$	4.05 ± 0.20
200	600 ± 200	154 ± 40	26.6 ± 9.2	0.81 ± 0.12
300	300 ± 25	125 ± 40	39.8 ± 0.9	2.13 ± 0.11
600	360 ± 20	240 ± 30	10.0 ± 0.7	2.62 ± 0.07

length scale $K_{eff}^{-1}(T_c/2)$, the values of σ_N may not be physically reasonable when $K_{eff}^{-1}(T_c/2) << d_N$.

5.4.2 Nb/Cu

The Nb/Cu R_s data indicates that a penetration depth on the order of 300Å and a decay length $K_{eff}^{-1}(T_c/2) = 400$Å are reasonable. Since the $\Delta\lambda_{eff}(T)$ data was fit well with a temperature dependence $K_{eff}^{-1}(T) \sim T^{-2}$, the R_s data should also follow this dependence as well. Figure 5.10 shows the R_s data for Nb/Cu bilayers, along with fits to this temperature dependence. The fits seem qualitatively correct at high temperature, but they all fail at low temperature, where T^{-2} diverges the most. Hence, it does seem that other fitting functions may be possible. The parameter values given in Table 5.2 for the normal state conductivities, on the other hand, are not inconsistent with observed values. Further investigation of this discrepancy in the temperature dependence of $K_{eff}^{-1}(T)$ is in progress.

5.5 Chapter Summary

The surface resistance of S/N bilayers can be calculated by an integral over the film thickness involving fields and currents, derived from considerations of the perpendicular component of the Poynting vector integrated over the film surface. If one knows the functional dependence for the real part of the conductivity $\sigma_{1N}(z,T)$, one can calculate the surface resistance as a function of temperature. It has been shown in this chapter that a model based on the Mattis-Bardeen theory, adapted for spatially inhomogeneous superconducting systems, can reproduce many features of the surface resistance data observed in S/N bilayers of Nb/Al and Nb/Cu. This model, while nonrigorous, contains many essential features that an exact model would, such as coherence effects between excitations above the induced condensate in the normal layer.

126

It was demonstrated that a simple two-fluid model, applied locally, cannot account for the observed behavior of $R_s(T)$ or its dependence on d_N.
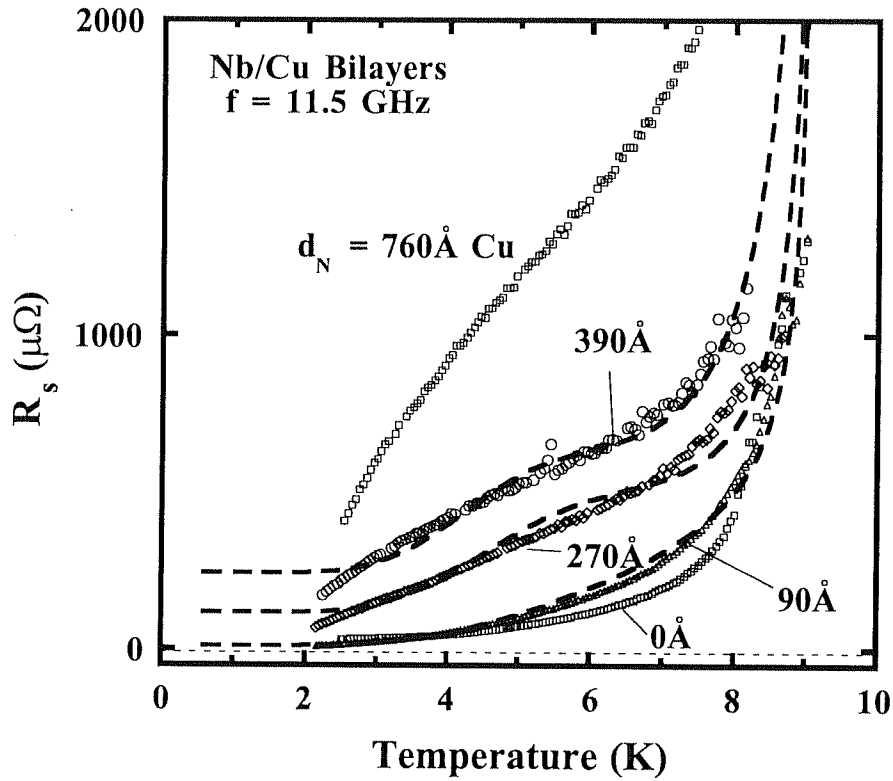

Fig. 5.10. Surface resistance data for Nb/Cu bilayers with $d_S = 3000\text{\AA}$ and $0 \le d_N \le 760\text{\AA}$, showing fits to the adapted Mattis-Bardeen model. The temperature dependence $K_{eff}^{-1}(T) \sim T^{-2}$ was used, as in the $\Delta\lambda_{eff}(T)$ fits. Here, however, the low-temperature behavior is not consistent with $K_{eff}^{-1}(T) \sim T^{-2}$.

Table 5.2. Normal metal thicknesses and fitting parameters for $R_s(T)$ data on Nb/Cu bilayers. Bare Nb data ($d_N = 0$), obtained by removing the Al from the 300Å sample, was fit using the homogeneous Mattis-Bardeen theory. These fits used the same values of $\lambda_S(0)$ and T_c given in Table 4.2. The parameter α was taken to be unity.

d_N (Å)	$\lambda_N(0,0)$ (Å)	$K^{-1}(T_c/2)$ (Å)	σ_N ($10^8\ \Omega^{-1}\text{m}^{-1}$)	σ_S ($10^8\ \Omega^{-1}\text{m}^{-1}$)
0	----	-----	------	1.36 ± 0.02
90	300 ± 50	300 ± 50	6.72 ± .75	0.50 ± 0.12
270	300 ± 50	400 ± 50	6.17 ± .61	1.74 ± 0.23
390	300 ± 50	400 ± 50	4.98 ± .41	3.37 ± 0.34

Chapter 6
Thesis Summary and Future Work

6.0   Context of This Work

The parallel-plate resonator technique was employed in this work to investigate the induced superconducting properties of thin normal metal films of Al and Cu deposited onto Nb. This technique was shown to be uniquely suited to studying the induced superconducting properties of the normal metal in the region near the S/N interface, since it is sensitive to both the induced condensate properties and the properties of the excitations above this condensate. In fact, the technique is constrained to only relatively thin normal layers ($d_N \sim 10^2$ - 10^3 Å), since RF losses become too high with thicker normal layers. The samples studied were generally much thinner than those used in previous experiments on the proximity effect.

The primary contribution of this work is a study of proximity systems which **require** analysis going beyond the single frequency approximation. Very few experiments, especially those relying on electromagnetic screening properties, have had enough sensitivity to really distinguish between the single frequency approximation and the exact case. The results presented in this thesis clearly show that in thinner normal layers, the exact behavior of the order parameter may differ considerably from that predicted by the single frequency approximation.

A secondary contribution of this work is the consideration of electromagnetic absorption processes in proximity-coupled normal metals at microwave frequencies. Due to the time-reversal symmetry properties of the electromagnetic perturbation Hamiltonian, the experimental technique used in this thesis enables one to investigate superconducting coherence effects in the proximity-coupled normal metal.

128

6.1   Results and Accomplishments

An experimentalist's picture of the important processes influencing the screening and absorption of microwave-frequency radiation by superconductor/normal-metal bilayer films has been constructed. It was found that the normal layer, even when very thin, plays the dominant role in the low temperature behavior of the effective penetration depth and the surface resistance in S/N bilayers, and that the suppression of the order parameter in the superconducting layer near the S/N interface has a negligible effect on these properties. The rapid decrease in both $\lambda_{eff}(T)$ and $R_S(T)$ in S/N bilayers as $T \to 0$ (Figs. 3.2 and 3.4) was found to be associated with the divergence of the characteristic length scale for penetration of the superconducting order parameter into the N metal, $K_{eff}^{-1}(T)$. The model developed to understand the screening of applied magnetic field by an S/N bilayer, when applied to the data given in Ch. 3, showed that in both Al and Cu, this characteristic length scale was much shorter $(K_{eff}^{-1}(T_c/2) \sim 150 - 200\text{Å})$ than predicted by the single frequency approximation $(K^{-1}_{single\ freq.} \sim 500 - 1000\text{Å})$. It was concluded that the size of the length scale K_{eff}^{-1} was influenced by the rapid variation of the order parameter near the S/N interface, causing the effective decay length to appear shorter in thin normal films.

It was shown that the magnitude of the induced superconducting penetration depth in the normal metal layer, $\lambda_N(0,0)$, can be estimated by examining the temperature dependence of the S/N bilayer effective penetration depth $\lambda_{eff}(T)$ as the normal metal thickness is varied. When the normal metal layer is thinner than this induced penetration depth, no appreciable decrease or change in curvature is evident in the temperature dependence of $\lambda_{eff}(T)$ at low temperature; the normal layer is too thin to screen an applied field noticeably. As the normal metal thickness is increased, a decrease in $\lambda_{eff}(T)$ as $T \to 0$ becomes more and more prominent. The size of the induced normal metal penetration

depth $\lambda_N(0,0)$ is approximately equal to the value of the normal metal thickness d_N at which this decrease first becomes noticeable. In Cu and Al, this length was found to be $\lambda_N(0,0) \sim 300$ - $400\text{\AA}$. These values are in general smaller than those observed in thicker samples previously, and confirms a trend in which thinner proximity-coupled normal layers are found to have smaller induced penetration depths [41,48]. The values of $\lambda_N(0,0)$ are still larger than the London values, which for Al and Cu are both around λ_L = 180 - 200Å.

According to our model, the approximate size of the effective decay length K_{eff}^{-1} can be ascertained at the same time; K_{eff}^{-1} is approximately equal to the normal layer thickness at the temperature where the rapid decrease in $\lambda_{eff}(T)$ occurs. By varying the normal metal thickness and observing the temperature at which the rapid decrease in $\lambda_{eff}(T)$ occurs, the function $K_{eff}^{-1}(T)$ may be mapped out. This works only if the normal metal is thicker than $\lambda_N(0,0)$, of course. The best results are obtained when the condition $d_N > \lambda_N(0,0) > K_{eff}^{-1}(T_c/2)$ holds. For Al and Cu, this effective decay length was found to be in the range $K_{eff}^{-1}(T_c/2) \sim 150$ - 200Å, as stated above.

The benefit of these general guidelines is that one can estimate these two important length scales without having to know the exact temperature dependence of $\lambda_N(0,T)$ or $K_{eff}^{-1}(T)$, i.e., without having to do any data fitting.

Electromagnetic absorption was built into the model in order to understand the surface resistance of data obtained on S/N bilayers. A local real part of the conductivity $\sigma_{1N}(z,T)$ was calculated using the Mattis-Bardeen theory, assuming a local BCS gap $\Delta_N(z,T)$ which decays into the normal metal with the same length scale $K_{eff}^{-1}(T)$ used in the penetration depth analysis. It was found that such a model, though not rigorously correct, could reproduce the observed data on Nb/Al and Nb/Cu bilayers. Since superconducting coherence effects are a central part of the Mattis-Bardeen calculation of the real part of the conductivity, it was concluded that the success of the model suggests that coherence effects play a role in the absorption of electromagnetic radiation by

130

proximity-coupled normal metals. This is significant, since only a few experimental techniques are sensitive to these effects.

6.2 Future Work

The results of this thesis, though compelling, are not complete. In particular, several extensions of the present work seem worthy of consideration. These are briefly described below.

6.2.1 Data at Lower Temperature

The $\Delta\lambda_{eff}(T)$ and $R_S(T)$ data shown in Ch. 3 on Nb/Cu and Nb/Al were acquired only down to $T = 2K$; this limit was determined by the temperature of the helium bath in which the sample housing was submerged. Naturally, as the effective decay length diverges, further interesting behavior occurs, and the normal layers presumably act virtually like real superconductors at a low enough temperature. This means that at some point the effective penetration depth $\lambda_{eff}(T)$ must become independent of temperature, a condition which was never observed in the bilayer data presented in this thesis. It also implies that even very thick normal layers may exhibit extremely low surface resistance as $T \rightarrow 0$, a behavior which is hinted at in the 760Å Cu data of Fig. 3.5 but never observed because of the experimental lower temperature limit.

Microwave measurements performed in a He^3 cryostat going down to $T \sim 0.5$ K would therefore be of extreme value; in principle there is no reason why the experiment could not be adapted to such a cryostat.

6.2.2 High-Temperature Cuprate Superconductors

A similar S/N bilayer surface impedance measurement involving high temperature superconducting cuprate materials is of great interest to those undertaking efforts to

131

develop high-T_c SNS junctions. Although very little evidence has been found for the existence of induced superconductivity in noble metals (Au) deposited on cuprates such as $YBa_2Cu_3O_{7-\delta}$ (YBCO), it may be possible to obtain such coupling in metallic cuprate layers with properties altered by doping. In that case, the metallic properties of the high-T_c cuprate and its doped cousin would be very similar, and the two would differ only in transition temperature. It is advantageous for the development of proximity superconductivity to have two metals with similar densities of states, since the quantity Δ/NV is continuous at the S/N interface.

Work on c-axis $Pr_xY_{1-x}Ba_2Cu_3O_{7-\delta}/YBa_2Cu_3O_{7-\delta}$ (x = 0.4) bilayers has been carried out in order to explore the possibility of detecting proximity coupling in a high-T_c cuprate system. The c-axis oriented samples were grown on $LaAlO_3$ substrates by pulsed-laser deposition, under conditions detailed in section 2.2.4. In all bilayer samples, 3000Å-thick YBCO was deposited, followed by $Pr_xY_{1-x}Ba_2Cu_3O_{7-\delta}$ (PYBCO) layers of thickness 1000Å, 2000Å, and 3000Å. Single layer PYBCO films of thickness 3000Å were also grown for independent characterization. The PYBCO material had T_c = 59K, so it acted as the normal metal layer for 59K < T < 90K, and it was found to have a penetration depth of approximately $\lambda(0)$ = 5500Å.

The $\Delta\lambda_{eff}(T)$ and $R_S(T)$ data on PYBCO/YBCO bilayers are shown in Figs. 6.1 and 6.2. In the $\Delta\lambda_{eff}(T)$ data, the superconducting transition of the PYBCO layer at 59K is evident, and the change in slope of $\Delta\lambda_{eff}(T)$ is larger as d_N increases. However, there is little evidence of proximity-coupled behavior, such as a rapid decrease in $\Delta\lambda_{eff}(T)$, in the PYBCO layer above 59K. In fact, it looks very much like the behavior of two uncoupled superconductors, with one going through its superconducting transition at a lower temperature than the other. The probable reason for this behavior is that the size of the decay length K_{eff}^{-1} in PYBCO is much smaller than the penetration depth, which is at least 5500Å. When the situation $K_{eff}^{-1} \ll \lambda_N(0,0)$ holds, the onset of superconductivity in the normal layer appears to happen right at T_{cN}, since only then does $K_{eff}^{-1}(T)$ diverge
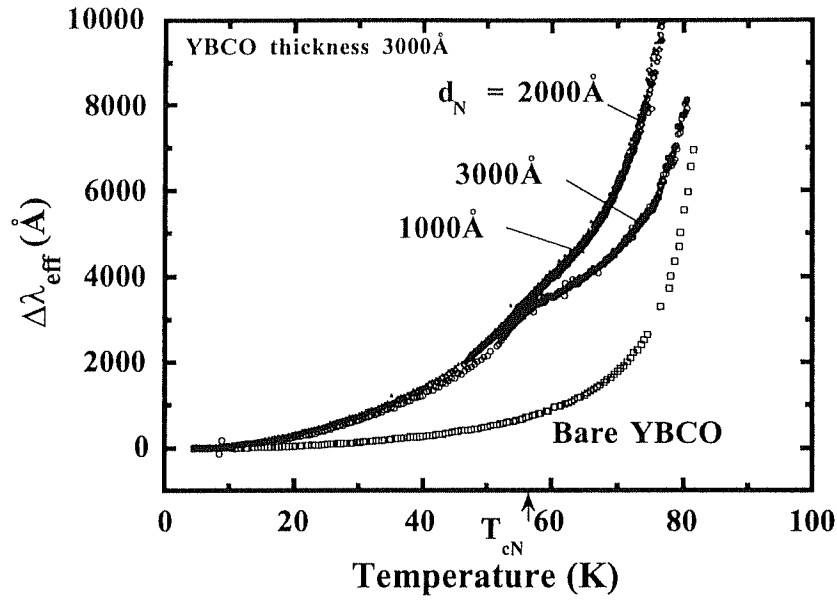
132

Fig. 6.1. Effective penetration depth change vs. temperature for high-T_c $Pr_xY_{1-x}Ba_2Cu_3O_{7-\delta}$/$YBa_2Cu_3O_{7-\delta}$ bilayers on $LaAlO_3$ substrates. The superconducting transition of the $Pr_xY_{1-x}Ba_2Cu_3O_{7-\delta}$ layer is clearly visible at 59K, but very little evidence of proximity-coupled behavior above 59K is discernible.

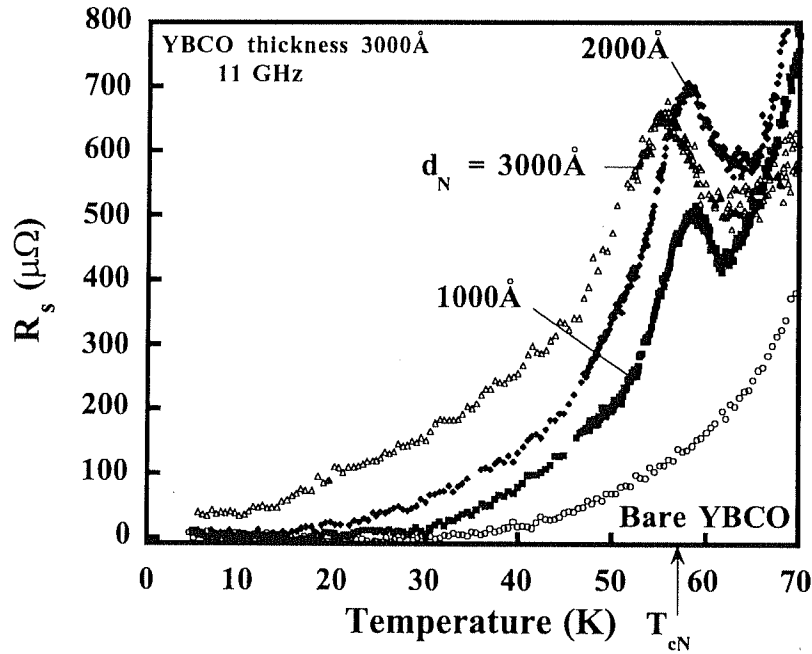Fig. 6.2. Surface resistance of $Pr_xY_{1-x}Ba_2Cu_3O_{7-\delta}$/$YBa_2Cu_3O_{7-\delta}$ bilayers vs. temperature. The peak around T_{cN} is normal even without proximity coupling when the conductivities of the two layers are different.

133

and become large enough to allow screening to occur in the N layer. So the behavior of $\Delta\lambda_{eff}(T)$ shown in Fig. 6.1 does not rule out the existence of proximity coupling in PYBCO, but it does mean that an electromagnetic measurement, which by its nature measures quantities which vary on the scale of the penetration depth, may not be the most sensitive experiment for its detection. Fig. 6.3 shows a close-up view of the transition region around 59K; the $\Delta\lambda_{eff}(T)$ data for the 3000Å PYBCO/YBCO bilayer sample is shown along with a fit assuming no proximity coupling at all between the layers. It agrees quite well with the data, so that the upper limit on $K_{eff}^{-1}(60K)$ in PYBCO is approximately 50Å. Since coherence lengths in the superconducting state of cuprate materials are thought to be even smaller than this (~ 10Å), this is not unreasonable.

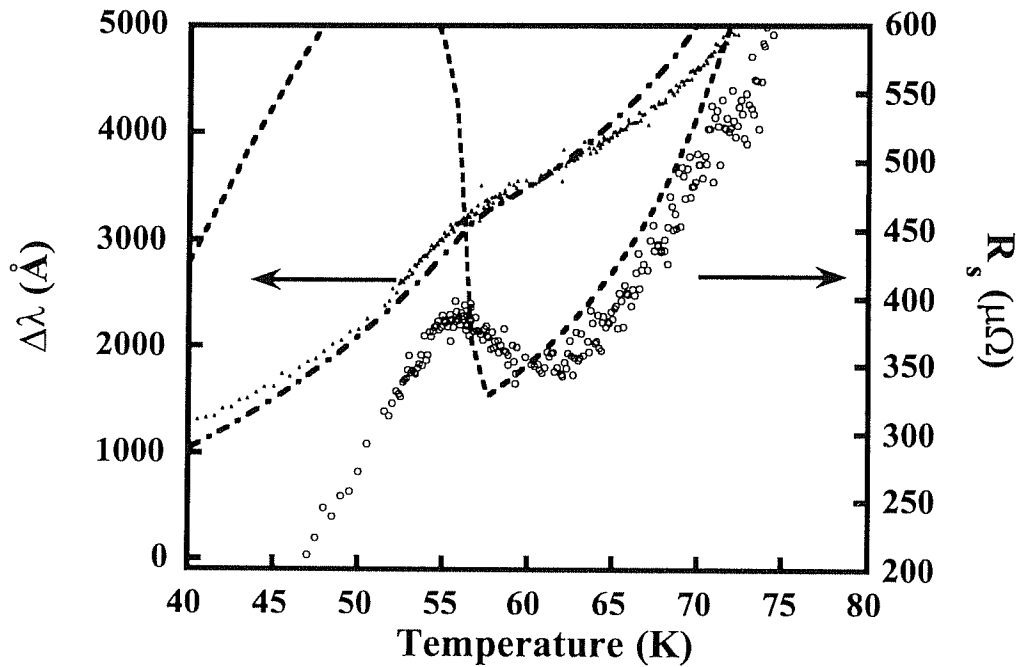Fig. 6.3. Close-up view of $\Delta\lambda_{eff}(T)$ and $R_S(T)$ for a PYBCO/YBCO bilayer with 3000Å normal metal. Dashed lines are the expected behavior of $\Delta\lambda_{eff}(T)$ and $R_S(T)$ in the absence of proximity coupling between the layers. The abrupt change in the temperature dependences of both quantities should occur at the same temperature, but the R_S data actually shows a dip at a higher temperature.

134

The surface resistance data, however, does show a noticeable feature around 59K in all three thicknesses of PYBCO. The dip is actually a normal feature of a two-superconductor bilayer with no proximity coupling, occurring when the conductivities of the two layers differ significantly. However, as the close-up view in Fig. 6.3 shows, the dip should be much more abrupt if that were the case, and it should occur at exactly the same temperature as the abrupt change in slope of $\Delta\lambda_{eff}(T)$ occurred at. Since this dip in R_s occurs at different temperatures for different normal layer thicknesses, this may be evidence of proximity coupling. Further work on such samples is required to ascertain whether or not these vestiges of proximity-induced superconductivity are real or not.

6.2.3 a-$Mo_{1-x}Ge_x$/$Mo_{1-y}Ge_y$ Bilayers

This system is another candidate for proximity effect experiments using a microwave technique. Since the films are amorphous, deposition in layers with a change in Ge doping is relatively straightforward and the films are extremely flat and smooth. The doping of Ge affects the T_c of the material, which has a maximum of 7.2K at 20% Ge doping. The idea, as with YBCO/PYBCO, is to create a bilayer system using two very similar metals which have different transition temperatures. Some preliminary work using 20% doping (T_c = 7.2K) for the S layer and 40% doping (T_c = 3.5K) has been completed; the results are shown in Figs. 6.4 and 6.5.

It is not clear at the time of this writing whether the ratio of penetration depth to decay length in the normal metal is suitable for microwave experiments or not; amorphous materials with mean free paths of ~ 2Å should in theory have very short decay lengths, making such an experiment less likely to produce fruitful results. Still, the ease with which T_c can be varied and the ease of fabrication make this system a sort of halfway point between the conventional metallic bilayers presented in the body of this thesis and the high-T_c bilayers of the last section. Again, further work is planned.

135
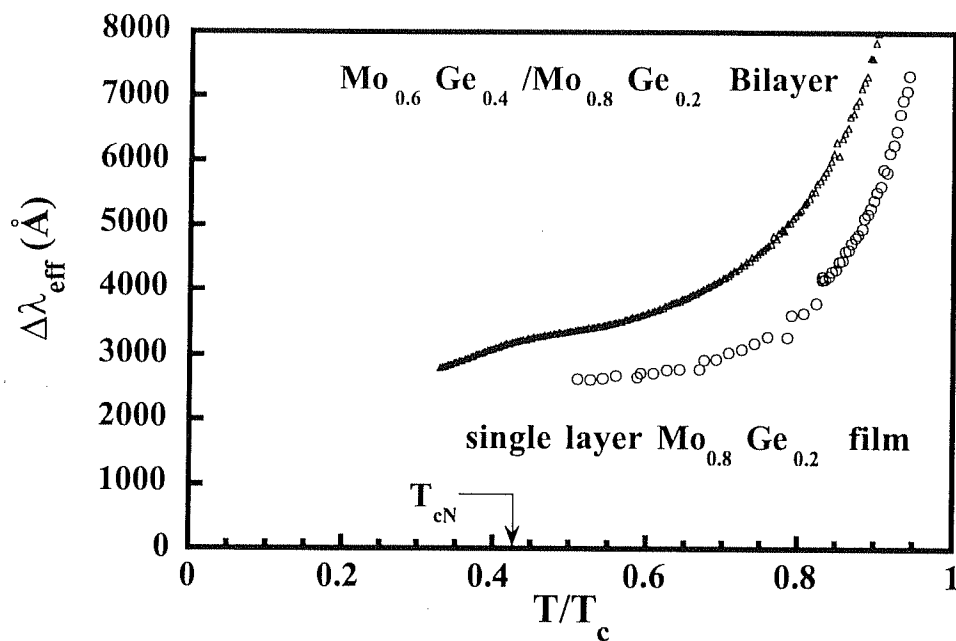
Fig. 6.4. Effective penetration depth vs. temperature for a single layer $Mo_{0.8}Ge_{0.2}$ film and a $Mo_{0.8}Ge_{0.2}$ /$Mo_{0.6}Ge_{0.4}$ bilayer, with d_S = 9000Å and d_N = 9000Å. The transition of the lower-T_c phase is visible near T_{cN}, but some linearity in $\Delta\lambda_{eff}(T)$ above T_{cN} seems evident, indicating possible proximity coupling.

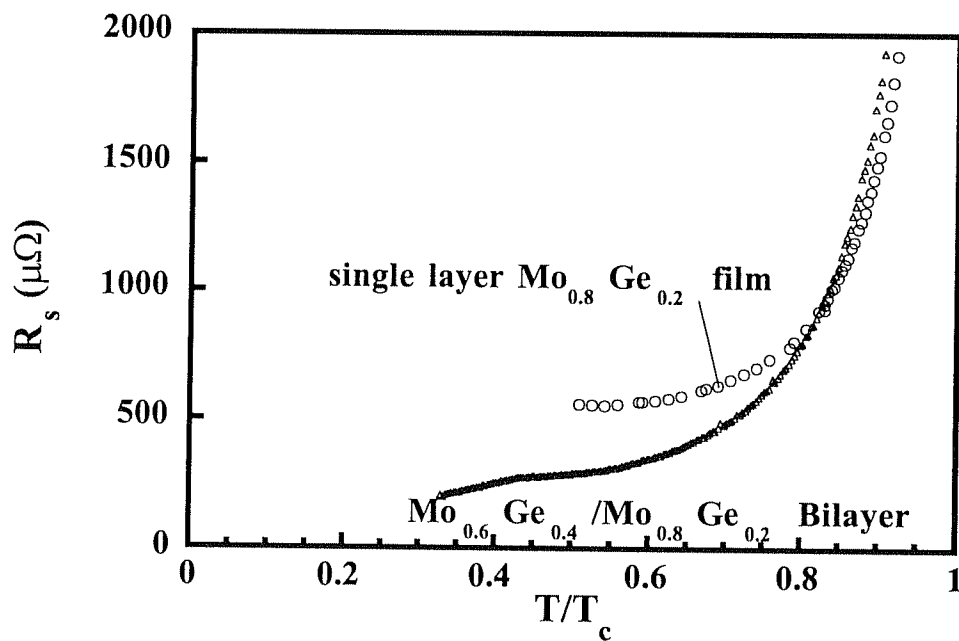Fig. 6.5. Surface resistance vs. temperature for the same $Mo_{0.8}Ge_{0.2}$ film and a $Mo_{0.8}Ge_{0.2}$ /$Mo_{0.6}Ge_{0.4}$ films as above. The decrease in R_s is plainly visible at T_{cN}, but strong evidence of a downturn in R_S above T_{cN} seems lacking.

136

References

[1] J. Bardeen, L. Cooper, and J. R. Schrieffer, Phys. Rev. **108**, 1175 (1957).

[2] R. Holm and W. Meissner, Z. Physik **87**, 715 (1932).

[3] E. F. Burton, J. O. Wilhelm, and A. D. Misener, Trans. Roy. Soc. Canada **28**, 65 (1934).

[4] J. F. Allen, Phil. Mag. **16**, 1005 (1933).

[5] L. P. Gor'kov, Soviet Phys. JETP **36**, 1364 (1959).

[6] Hans Meissner, Phys. Rev. **109**, 686 (1958).

[7] Hans Meissner, Phys. Rev. Lett. **2**, 458 (1959).

[8] Hans Meissner, Phys. Rev. **117**, 672 (1960).

[9] P. H. Smith, S. Shapiro, J. Miles, and J. Nicol, Phys. Rev. Lett. **6**, 686 (1961).

[10] A. C. Rose-Innes and B. Serin, Phys. Rev. Lett. **7**, 278 (1961).

[11] P. Hilsch, Z. Physik **167**, 511 (1962).

[12] J. J. Hauser, H. C. Theuerer, and N. R. Werthamer, Phys. Rev. **136**, A637 (1964).

[13] W. A. Simmons and D. H. Douglass, Jr., Phys. Rev. Lett. **9**, 153 (1962).

[14] A. E. Jacobs and D. M. Ginsberg, Phys. Rev. **175**, 569 (1968).

[15] A. E. Jacobs, Phys. Rev. **162**, 375 (1967).

[16] P. G. de Gennes, Phys. Kondens. Mat. **3**, 79 (1964).

[17] Leon N. Cooper, Phys. Rev. Lett. **6**, 689 (1961).

[18] P. Fulde and K. Maki, Phys. Rev. Lett **15**, 675 (1965).

[19] J. R. Schrieffer, D. J. Scalapino, and J. W. Wilkins, Phys Rev. Lett. **10**, 33 (1963).

[20] C. J. Adkins and B. W. Kington, Phil. Mag. **13**, 971 (1966).

[21] P. G. de Gennes and D. Saint-James, Phys. Lett. **4**, 151 (1963).

[22] J. M. Rowell and W. L. McMillan, Phys. Rev. Lett. **16**, 453 (1966).

137

[23] W. J. Tomasch, Phys. Rev. Lett. **1 6**, 16, 1966.

[24] J. Clarke, Proc. Roy. Soc. **A3 0 8**, 447 (1969).

[25] S. Greenspoon and H. J. T. Smith, Can. J. Phys. **4 9**, 1350 (1971).

[26] J. P. Romagnan, A. Gilabert, J. C. Noiray, and E. Guyon, Solid St. Comm.**1 4**, 83 (1974).

[27] J. P. Romagnan, A. Gilabert, J. P. Laheurte, and J. C. Noiray, Solid St. Comm. **1 6**, 359 (1975).

[28] E. L. Wolf, John Zasadzinski, and J. W. Osmun, J. Low Temp. Phys. **4 0**, 19 (1980).

[29] E. L. Wolf, *Principles of Electron Tunneling Spectroscopy* (Oxford, New York, 1985), Ch. 5.

[30] J. P. Burger, G. Deutscher, E. Guyon, and A. Martinet, Phys. Lett. **1 7**, 180 (1965).

[31] A. L. Schawlow and G. E. Devlin, Phys. Rev. **1 1 3**, 120 (1959).

[32] Orsay Group on Superconductivity, in *Quantum Fluids* (North-Holland, Amsterdam, 1966), p. 26.

[33] G. Deutscher and J. P. Hurault, Phys. Lett. **2 4 A**, 102 (1967).

[34] G. Deutscher, J. P. Hurault, and P. A. van Dalen, J. Phys. Chem. Solids **3 0**, 509 (1969).

[35] C. Vallette, Sol. State Comm. **9**, 895 (1971).

[36] Y. Oda and H. Nagano, J. Phys. Soc. Japan **4 4**, 2007 (1978).

[37] A. C. Mota, D. Marek, and J. C. Weber, Helv. Phys. Acta **5 5**, 647 (1982).

[38] Y. Oda, A. Sumiyama, and H. Nagano, Jap. J. Appl. Phys. **2 2**, 464 (1983).

[39] Y. Oda, A. Sumiyama, and H. Nagano, LT-17 Proc., 1025 (1984).

[40] A. C. Mota, in *Josephson Effect - Achievements and Trends*, ed. A. Barone (World Scientific, 1986), p. 248.

[41] A. C. Mota, P. Visani, and A. Pollini, J. Low Temp. Phys. **7 6**, 465 (1989).

[42] P. Visani, A. C. Mota, and A. Pollini, Physica B **165**, 1631 (1990).

[43] P. G. de Gennes, Rev. Mod. Phys. **36**, 225 (1964).

[44] D. S. Falk, Phys. Rev. **132**, 1576 (1963).

[45] J. H. Claassen, J. E. Evetts, R. E. Somekh, and Z. H. Barber, Phys. Rev. B **44**, 9605 (1991).

[46] A. T. Fiory and A. F. Hebard, Appl. Phys. Lett. **52**, 2165 (1988).

[47] M. L. Wilson and J. H. Claassen, Bull. Am. Phys. Soc. **40**, 72 (1995).

[48] R. W. Simon and P. M. Chaikin, Phys. Rev. B **23**, 4463 (1981).

[49] R. W. Simon and P. M. Chaikin, Phys. Rev. B **30**, 3750 (1984).

[50] H. Meissner and R. V. Fanelli, Rev. Mod. Phys. **36**, 194 (1964).

[51] G. Fischer and R. Klein, Phys. Kond. Materie **7**, 12 (1968).

[52] M. Garfunkel, Phys. Rev. **173**, 516 (1968).

[53] S. C. Harris, Proc. Roy. Soc. Lond. **A350**, 267 (1976).

[54] J. R. Hook and J. A. Battilana, J. Phys. F **6**, 1689 (1976).

[55] R. C. Taber, Rev. Sci. Instr. **61**, 2200 (1990).

[56] J. R. Hook and J. R. Waldram, Proc. Roy. Soc. **A 334**, 171 (1973).

[57] J. R. Hook, J. Low Temp. Phys. **23**, 645 (1976).

[58] A. V. Zaitsev, Sov. Physics JETP **59**, 1015 (1984).

[59] D. C. Mattis and J. Bardeen, Phys. Rev. **111**, 412 (1958).

[60] G. Deutscher. S. Y. Hsieh, P. Lindenfeld, and S. Wolf, Phys. Rev. B **8**, 5055 (1973).

[61] E. Krätzig and W. Schreiber, Phys. Kondens. Materie **16**, 95 (1973).

[62] G. Zheng, Y. Kohori, Y. Oda, K. Asayama, R. Aoki, Y. Obi, and H. Fujimori, J. Phys. Soc. Japan **58**, 39 (1989).

[63] N. N. Bogoliubov, Sov. Phys. Uspekhi **67**, 236 (1959).

[64] P. G. de Gennes, *Superconductivity of Metals and Alloys* (Addison-Wesley, New York, 1989), p. 140.

[65] N. N. Bogoliubov, Sov. Phys. JETP **7**, 41 (1958).

[66] J. G. Valatin, Nuovo Cimento **7**, 843 (1958).

[67] M. Tinkham, *Introduction to Superconductivity* (McGraw-Hill, New York, 1975), p. 30.

[68] A. F. Andreév, Sov. Phys. JETP **19**, 1228 (1964).

[69] P. G. de Gennes and E. Guyon, Phys. Lett. **3**, 168 (1963).

[70] N. R. Werthamer, Phys. Rev. **132**, 2440 (1963).

[71] G. Deutscher and P. G. de Gennes, in *Superconductivity*, edited by R. D. Parks (Dekker, New York, 1969), p. 1005.

[72] Tinkham, section on current carrying case 8.3?.

[73] W. Silvert, J. Low Temp. Phys. **20**, 439 (1975).

[74] G. B. Arnold, Phys. Rev. B **18**, 1076 (1978).

[75] M. Ashida, S. Aoyama, J. Hara, and K. Nagai, Phys. Rev. B **40**, 8673 (1989).

[76] V. G. Kogan, Phys. Rev. B **26**, 88 (1982).

[77] V. Z. Kresin, Phys. Rev. B **32**, 145 (1985).

[78] V. Z. Kresin and S. A. Wolf, Phys. Rev. B **46**, 6458 (1992).

[79] J. D. Jackson, *Classical Electrodynamics*, 2nd Ed., (Wiley, New York, 1975), p.242.

[80] N. Klein, H. Chaloupka, G. Müller, S. Orbach, H. Piel, B. Roas, L. Schultz, U. Klein, and M. Peiniger, J. Appl. Phys. **67**, 6940 (1990).

[81] A. Fathy, D. Kalokitis, and E. Belohoubek, Microwave J. 75 (Oct. 1988).

[82] B. Mühlschlegel, Z. Physik, **155**, 313 (1959).

[83] A. Shoji, S. Kiryu, and S. Kohjiro, Appl. Phys. Lett. **60**, 1624 (1992).

[84] S. Y. Lee, M. Bruns, and R. D. Glenn, IEEE Trans. Appl. Supercond. **3**, 2953 (1993).

[85] M. S. Pambianchi, S. M. Anlage, E. S. Hellman, E. H. Hartford, Jr., M. Bruns, and S. Y. Lee, Appl. Phys. Lett. **64**, 244 (1994).

[86] J. P. Turneaure, J. Halbritter, and H. A. Schwettman, J. Supercond. **4**, 341 (1991).

[87] S. Kashiwaya, M. Koyanagi, A. Shoji, M. Matsuda, and H. Shibata, IEEE Trans. Magn. **2 7**, 837 (1991).

[88] M. Hikita, K. Takei, and M. Igarashi, J. Appl. Phys. **5 4**, 7066 (1983).

[89] B. Batlogg, R. J. Cava, L. W. Rupp, Jr., A. M. Mujsce, J. J. Krajewski, J. P. Remeika, W. F. Peck, A. S. Cooper, and G. P. Epinosa, Phys. Rev. Lett. **6 1**, 1670 (1988).

[90] E. S. Hellman, E. H. Hartford, and E. M. Gyorgy, Appl. Phys. Lett. **5 8**, 1335 (1991).

[91] J. F. Zasadzinski, N. Tralshawala, Q. Huang, K. E. Gray, and D. G. Hinks, IEEE Trans. Mag. **2 7**, 833 (1991).

[92] F. Sharifi, A. Pargellis, R. C. Dynes, B. Miller, E. S. Hellman, J. Rosamilia, and E. H. Hartford, Jr., Phys. Rev. B **4 4**, 12521 (1991).

[93] H. Sato, H. Takagi, and S. Uchida, Physica C **1 6 9**, 391 (1990).

[94] A. N. Pargellis, F. Sharifi, R. C. Dynes, B. Miller, E. S. Hellman, J. Rosamilia, and E. H. Hartford, Jr., Appl. Phys. Lett. **5 8**, 95 (1991).

[95] Z. Schlesinger, R. T. Collins, J. A. Calise, D. G. Hinks, A. W. Mitchell, Y. Zheng, B. Dabrowski, N. E. Bickers, and D. J. Scalapino, Phys. Rev. B **4 0**, 6862 (1989).

[96] E. J. Ansaldo, Z. R. Wang, J. H. Cho, D. C. Johnston, T. M. Riseman, Physica C **185-189**, 1889 (1991).

[97] C. Kwon, Qi Li, X. X. Xi, S. Bhattacharya, C. Doughty, T. Venkatesan, H. Zhang, J. W. Lynn, J. L. Peng, Z. Y. Li, N. D. Spemcer, and K. Feldman, Appl.Phys. Lett. **6 2**, 1289 (1993).

[98] A. Inam, M. S. Hegde, X. D. Wu, T. Venkatesan, P. England, P. E. Miceli, E. W. Chase, C. C. Chang, J. M. Tarascon, and J. B. Wachtman, Appl. Phys. Lett.

5 3, 908 (1988).

[99] Jian Mao, D. H. Wu, J. L. Peng, R. L. Greene, and S. Anlage, Phys. Rev. B.
Rapid Comm. **5 1**, 3316 (1995).

[100] J. F. Annett, N. Goldenfel, and S. R. Renn, Phys. Rev. B **4 3**, 2778 (1991).

[101] M. S. Pambianchi, J. Mao, and S. M. Anlage, Phys. Rev. B **5 0**, 13659 (1994).

[102] T. Imamura and S. Hasuo, IEEE Trans. Magn. **2 7**, 3172 (1991).

[103] P. C. van Son, H. van Kempen, and P. Wyder, Phys. Rev. Lett. **5 9**, 2226
(1987).

[104] G. E. Blonder, M. Tinkham, and T. M. Klapwijk, Phys. Rev. B **2 5**, 4515
(1982).

[105] W. Silvert and L. N. Cooper, Phys. Rev. **141**, 336 (1966).

[106] M. Tinkham, *Introduction to Superconductivity* (McGraw-Hill, New York, 1975),
p. 113.

[107] P. G. de Gennes and J. Matricon, Solid State Comm. **3**, 151 (1965).

[108] M. Abramowitz and I. A. Stegun, *Handbook of Mathematical Functions* (Dover,
New York, 1965), pp. 556-563.

[109] M. Tinkham, *Introduction to Superconductivity* (McGraw-Hill, New York, 1975),
p. 50.

Curriculum Vitae

Name: Michael Scott Pambianchi

Permanent Address: 48 Bullymuck Rd., New Milford, Connecticut 06776

Degree and date to be conferred: Ph.D., 1995

Date of birth: December 12, 1967

Place of birth: Valley Stream, New York

Secondary education: Hunterdon Central High School, Flemington, New Jersey, 1985

Collegiate institutions attended:

INSTITUTION	DATES ATTENDED	DEGREE	DATE OF DEGREE
Cornell University	1985-1989	B. A.	1989
University of Maryland	1989-1995	Ph.D.	1995

Major: Physics

Minors: Mathematics, Foreign Languages

Professional publications:

Michael S. Pambianchi, Sining Mao, and Steven M. Anlage, "Microwave Surface Impedance of Proximity-Coupled Nb/Al Bilayer Films", Phys. Rev. B **5 2**,4477 (1995).

Michael S. Pambianchi, J. Mao, and Steven M. Anlage, "Magnetic Screening in Proximity-Coupled Superconductor/Normal-Metal Bilayers", Phys. Rev B **5 0**, 13659 (1994).

Steven M. Anlage, Michael Pambianchi, Alp T. Findikoglu, C. Doughty, Dong-Ho Wu, Jian Mao, Si-Ning Mao, X. X. Xi, T. Venkatesan, J. L. Peng, and R. L. Greene, "The Electrodynamics of Oxide Superconductors", SPIE Proceedings, Vol. 2158 (1994).

M. S. Pambianchi, S. M. Anlage, E. S. Hellman, E. H. Hartford, Jr., M. Bruns, and S. Y. Lee, "Penetration Depth, Microwave Surface Resistance, and Gap Ratio in NbN and $Ba_{1-x}K_xBiO_3$ Thin Films", Appl. Phys. Lett. **6 4**, 244 (1994).

M. S. Pambianchi, D. H. Wu, L. Ganapathi, and S. M. Anlage, "DC Magnetic Field

Dependence of the Surface Impedance in Superconducting Parallel-Plate Transmission Line Resonators", IEEE Trans. Appl. Supercon. **3**, 2774 (1993).

A. T. Findikoglu, S. Bhattacharya, C. Doughty, M. S. Pambianchi, Qi Li, X. X. Xi, S. M. Anlage, R. E. Fahey, A. J. Strauss, Julia M. Phillips, and T. Venkatesan, "$Sr_2AlTaO_6/YBa_2Cu_3O_7$ Heterostructures for Superconducting Device Applications", IEEE Trans. Appl. Supercon. **3**, 1425 (1993).